

## ABSTRACT

Title of Document: A BIOPHYSICAL EVALUATION OF CELL-SUBSTRATE INTERACTIONS DURING SPREADING, MIGRATION AND NEURON DIFFERENTIATION

Leann Lynn Norman, Ph.D. 2010

Directed By: Assistant Professor Helim Aranda-Espinoza  
Fischell Department of Bioengineering

The development of engineered scaffolds has become a popular current avenue to treat numerous traumas and disease. In order to optimize the efficiency of these treatments, it is necessary to have a more thorough understanding of how cells interact with their substrate and how these interactions directly affect cellular behavior. Cell spreading is a critical component of numerous biological phenomena, including embryonic development, cancer metastasis, immune response, and wound healing. Along with spreading, cell adhesion and migration are all strongly dependent on the interactions between the cell and its substrate. Cell-substrate interactions can affect critical cellular mechanisms including internal cellular signaling, protein synthesis, differentiation, and replication and also influence the magnitude of adherence and motility. In an effort to better understand cell-substrate interactions we characterize the initial stages of cell spreading and blebbing using cell-substrate specific microscopy techniques, and identify the effects of cytoskeletal

disruption and membrane modification on surface interactions and spreading. We identify that blebs appear after a sharp change in cellular tension, such as following rapid cell-substrate detachment with trypsin. An increased lag phase of spreading appears with increased blebbing; however, blebbing can be tuned by supplying the cell with more time to perform plasma membrane recycling. We developed software algorithms to detect individual bleb dynamics from TIRF and IRM images, and characterize three types of bleb-adhesion behaviors. Overall, we show that blebs initially create the first adhesion sites for the cell during spreading; however, their continuous protrusion and retraction events contribute to the slow spreading period prior to fast growth. In addition, we identify the elastic modulus of the rat cortex and characterize a polyacrylamide gel system that evaluates the effects of substrate stiffness on cortical outgrowth. Remarkably, we illustrate that cortical neuron differentiation and outgrowth are insensitive to substrate stiffness, and observe only morphological differences between laminin versus PDL-coated substrates. Together, this research identifies cell-specific behaviors critical to spreading and migration. The thorough evaluations of spreading and migration behavior presented here contribute to the understanding of critical cellular phenomena and suggest potential therapeutic targets for treatment of cardiovascular disease and neurological disorders.

A BIOPHYSICAL EVALUATION OF CELL-SUBSTRATE INTERACTIONS  
DURING SPREADING, MIGRATION AND NEURON DIFFERENTIATION

By

Leann Lynn Norman

Dissertation submitted to the Faculty of the Graduate School of the  
University of Maryland, College Park, in partial fulfillment  
of the requirements for the degree of  
Doctor of Philosophy  
2010

Advisory Committee:

Assistant Professor Helim Aranda-Espinoza, Chair

Professor Avis Cohen

Professor William Bentley

Assistant Professor Sameer Shah

Appointed Faculty James Valdes

© Copyright by  
Leann Lynn Norman  
2010

## **Dedication**

I dedicate this work to my parents, Karen and Joseph Matta, who have always encouraged me to pursue my interests. They have provided endless support and inspiration throughout this journey.

## Acknowledgements

I would first like to thank my advisor, Dr. Helim Aranda-Espinoza for supplying me with the opportunity to work in his lab and discover the world of biophysics. The opportunities and experiences that you have supplied me with throughout my studies will remain with me forever. I also acknowledge beneficial suggestions and advice from all of my committee members.

I also acknowledge multiple collaborators, including Dr. Kheya Sengupta, Dr. Pierre Sens, Dr. Jan Brugués, Dr. Micah Dembo, Fitzroy Byfield, Dr. Daniel Hammer, and Dr. Irena Levitan. I am grateful for the opportunity to travel to Dr. Sengupta's lab in Marseille to learn from her expertise in image software. Also, to Dr. Sens and Dr. Brugués for their development of the theoretical model on cell blebbing and membrane recycling. Thanks to Dr. Micah Dembo for development and use of the traction force microscopy software and to Dr. Lisa Taneyhill, Dr. Herbert Geller and Dr. Pierre Nassoy for their comments and suggestions during my manuscript preparations.

A special thanks to the U.S. Army for a much appreciated CREST fellowship and the Philanthropic Educational Organization for additional financial support. To all the members of the Cell Biophysics laboratory, thank you for your helpful critiques and suggestions. I appreciate our new friendships and lasting memories.

To all of my friends, thank you for the distractions and laughter along the way. Finally, to my family, thank you for your love and support, and to my husband, Joe, for his endless encouragement and optimism.

## Table of Contents

Dedication.....	ii
Acknowledgements.....	iii
Table of Contents.....	iv
List of Tables.....	vii
List of Figures.....	viii
1 Introduction.....	1
2 Background – Cell spreading and cell-substrate interactions.....	3
2.1 Cell spreading.....	3
2.1.1 Introduction.....	3
2.1.2 Physiological relevance.....	4
2.1.3 Basic principles of cell spreading and migration.....	7
2.2 Neuronal cell spreading.....	12
2.2.1 Introduction.....	12
2.2.2 Physiological Relevance.....	13
2.2.3 Basic principles of neuronal spreading and migration.....	17
2.3 Methods for detecting cell-substrate interactions and spreading.....	27
2.3.1. Bright field microscopy.....	27
2.3.2. Interference reflection microscopy.....	27
2.3.3. Total internal reflection fluorescence microscopy.....	28
2.3.4. Atomic force microscopy.....	31
2.4 Summary.....	32
3 Characterization of the initial stages of endothelial cell spreading and blebbing...	33
3.1 Introduction.....	33
3.2 Materials and methods.....	35
3.2.1 Cell culture and substrate preparation.....	35
3.2.2 Detachment and spreading experiments, and actin staining.....	35
3.2.3 Microscopy, imaging conditions, and data analysis.....	36
3.3 Results.....	37
3.3.1 Blebs appear following rapid cell detachment.....	37
3.3.2 Endocytosis regulates cell blebbing.....	38
3.3.3 Role of blebs in cell spreading.....	39
3.3.4 Model.....	41
3.4 Conclusions.....	46
4 Effect of cytoskeletal disruption and membrane modification on endothelial cell spreading and blebbing.....	55
4.1 Introduction.....	55
4.2 Materials and methods.....	57
4.2.1 Cell culture and substrate preparation.....	57
4.2.2 Drug treatments and osmotic manipulation.....	58
4.2.3 Microscopy and imaging conditions.....	58
4.2.4 Cell spreading experiments.....	59
4.2.5 Data Analysis.....	59

4.3 Results.....	60
4.3.1 Cytoskeletal disruptions and membrane tension affect global statistics of spreading and blebbing .....	60
4.3.2 Cytoskeletal disruptions inhibit initial spreading .....	62
4.3.3 Bleb adhesion dynamics during spreading .....	67
4.3.4 Physical forces inhibit bleb retraction.....	69
4.3.5 Paxillin localization appears after the cessation of blebs.....	70
4.4 Conclusions.....	72
5 Modification of cellular cholesterol content affects traction force, adhesion and cell spreading.....	88
5.1 Introduction.....	88
5.2 Materials and methods .....	91
5.2.1 Cell culture.....	91
5.2.2 Coverslip activation and polyacrylamide gel preparation .....	91
5.2.3 Cholesterol treatment.....	92
5.2.4 Fluorescence labeling of BAEC monolayers.....	93
5.2.5 Traction force microscopy.....	93
5.2.5 Interference reflection microscopy .....	94
5.2.6 Total internal reflection fluorescence microscopy.....	94
5.2.7 Data Analysis.....	94
5.3 Results.....	95
5.3.1 Cholesterol-depletion increases the average traction force .....	95
5.3.2 Cholesterol-depletion increases focal adhesion size.....	97
5.3.3 Cholesterol treatment affects spreading behavior.....	99
5.3.4 Monolayer area decreases with both cholesterol depletion and enrichment .....	101
5.4 Conclusions.....	104
6 Effects of substrate stiffness on cortical neuron outgrowth and differentiation ...	110
6.1 Introduction.....	110
6.2 Materials and methods .....	113
6.2.1 Preparation of substrates .....	113
6.2.2 Determination of Young's moduli using dynamic mechanical analysis ..	113
6.2.3 Determination of Young's moduli using atomic force microscopy.....	114
6.2.4 Characterization of surface-bound laminin.....	115
6.2.5 Cell Culture and experimental conditions.....	116
6.2.6 Inhibition of myosin II with blebbistatin .....	117
6.2.7 Antibodies and immunostaining .....	117
6.2.8 Image analysis and statistics .....	118
6.3 Results.....	119
6.3.1 Identification of cortex stiffness using atomic force microscopy .....	119
6.3.2 Specification of substrate ligand concentration and Young's modulus...	120
6.3.3 Axonal differentiation of cortical neurons is insensitive to substrate stiffness .....	121
6.3.4 Cortical outgrowth is insensitive to substrate stiffness.....	124
6.3.5 Process extension is more directed on laminin-coated substrates .....	127
6.3.6 Myosin II inhibition is independent of substrate stiffness.....	129

6.4 Conclusions.....	132
7 Summary and conclusions .....	148
8 Future work and applications.....	151
9 Appendix:.....	154
Appendix A: Coverslip activation and polyacrylamide gel polymerization.....	154
Appendix B: Imaging conditions.....	155
Appendix C: IGOR image analysis software algorithms.....	157
Appendix D: Modeling cell blebbing and plasma membrane tension .....	159
10 Bibliography .....	169

## List of Tables

Table 4.1	Effect of cytoskeletal and membrane treatment on BAEC spreading and blebbing	(79)
-----------	--	------

## List of Figures

Figure 2.1	Stages of typical cell spreading.	(3)
Figure 2.2	A simplified schematic of cellular migration.	(9)
Figure 2.3	PC12 spreading using interference reflection microscopy.	(12)
Figure 2.4	Schematic representation of spinal cord injury and the glial scar.	(16)
Figure 2.5	Schematic representation of total internal reflection fluorescence microscopy.	(28)
Figure 2.6	Comparison of adhesion using IRM with vinculin immunostaining.	(30)
Figure 2.7	Schematic representation of atomic force microscopy.	(31)
Figure 3.1	Identification of cellular blebs during detachment using IRM.	(50)
Figure 3.2	The number of blebs per cell decreased with time spent in suspension.	(51)
Figure 3.3	Differences in initial spreading behavior were observed for individual blebbing and non-blebbing cell spreading events.	(52)
Figure 3.4	Viscoelastic model for cell spreading.	(53)
Figure 3.5	Evolution of the (normalized) average number of blebs per cell $n_b$ with time.	(54)
Figure 4.1	Total spreading area observed for cells under drug or osmotic treatment after 1 and 4 hours of spreading.	(80)
Figure 4.2	Representative images of cells observed using interference reflection microscopy illustrated for each treatment condition.	(81)
Figure 4.3	Cell spreading dynamics for control, blebbistatin, nocodazole, and latA treated cells.	(82)
Figure 4.4	Coexistence of blebs and lamella during spreading.	(83)
Figure 4.5	Identification of individual bleb adhesions using self-written algorithms.	(84)
Figure 4.6	Bleb-surface interactions observed using IRM reveal both adhering and retracting bleb dynamics during the initial stages of spreading.	(85)

Figure 4.7 Cellular bleb dynamics observed using total internal reflection fluorescence microscopy.	(86)
Figure 4.8 Actin and paxillin organization during spreading of control, blebbistatin, nocodazole, and latA treated cells.	(87)
Figure 5.1 Effect of cellular cholesterol on cell traction forces.	(105)
Figure 5.2 Identification of the average vinculin contact area using total internal reflection fluorescence microscopy.	(106)
Figure 5.3 Single cell spreading on fibronectin-coated glass substrates.	(107)
Figure 5.4 Total spreading area of control, cholesterol-enriched and cholesterol-depleted cells after 1 hour of spreading.	(108)
Figure 5.5 Effect of cholesterol treatment on BAEC confluent monolayers.	(109)
Figure 6.1 Specification of ligand concentration using anti-laminin antibodies.	(138)
Figure 6.2 Cortical neurons exhibit similar differentiation regardless of stiffness	(139)
Figure 6.3 Cortical neuron outgrowth observed based on substrates stiffness.	(140)
Figure 6.4 Axon extension and retraction dynamics for laminin and PDL-coated substrates.	(141)
Figure 6.5 Dorsal root ganglion outgrowth on substrates of varying stiffness.	(142)
Figure 6.6 Process extension on laminin versus PDL-coated substrates.	(143)
Figure 6.7 Cell body displacements are increased on laminin-coated substrates.	(144)
Figure 6.8 Inhibition of myosin II with blebbistatin.	(145)
Figure 6.9 Long-term observations of axon outgrowth between 49-53 hours of culture on laminin and PDL-coated glass substrates reveals numerous periods of extension, retraction, and stalling.	(146)
Figure 6.10 A simplified schematic illustrating some of the major cytoskeletal components and forces involved in axon extension and retraction.	(147)

Appendix Fig. 1 Constitutive viscoelastic equation for the cell membrane.	(161)
Appendix Fig. 2 Evolution of the average number of blebs cell with time.	(166)
Appendix Fig. 3 Spreading kinetics for different incubation times.	(168)

# 1 Introduction

Cell spreading is a critical component of numerous biological phenomena, including embryonic development, cancer metastasis, immune response, and wound healing. Along with spreading, cell adhesion and migration are all strongly dependent on the interactions between the cell and its substrate. These cell-substrate interactions can control the occurrence and magnitude of adherence and motility, and can also affect critical cellular mechanisms including internal cellular signaling, protein synthesis, differentiation, and replication. Recently, the development of engineered scaffolds has become a popular avenue to treat numerous traumas and disease. However, in order to optimize the efficiency of these scaffolds and disease treatments, it is necessary to have a more thorough understanding of how cells interact with their substrate and how these interactions directly affect cellular behavior.

In order to develop a more comprehensive understanding on how cells interact with their substrates during critical biological phenomena, we proposed the following objectives:

- (1) Investigate and characterize the initial stages of endothelial cell spreading and blebbing using cell-substrate specific microscopy techniques;
- (2) Investigate the effects of cytoskeletal disruption and membrane modification on surface interactions and endothelial cell spreading;
- (3) Investigate the effects of substrate stiffness on cortical neuron morphology, outgrowth and differentiation.

Collectively, this research is aimed towards completing these objectives in order to provide a more complete understanding of how cell-substrate interactions affect critical cellular phenomena. In turn, this knowledge will broadly impact biomedical and tissue engineering approaches aimed in particular at cardiovascular and neurological disease.

## 2 Background – Cell spreading and cell-substrate interactions

### 2.1 Cell spreading

#### 2.1.1 Introduction

Cell spreading is a critical component of numerous biological events including embryonic development, mitosis, wound healing, and the immune response. Although it has recently been proposed that the dynamics of adhesion for all cell types follow a universal behavior (1), neutrophils (2), red blood cells (3, 4), fibroblasts (5) and other cell types all exhibit different morphologies and time scales during the cell spreading process. While the individual mechanisms involved with cell spreading and migration are dependent on the specific cell type, the typical characteristic behavior of cell spreading is illustrated in Figure 2.1. Briefly, there occurs an initial cell-substrate contact, where the cell recognizes and binds to the surface (6). Following the initial contact, the cell transitions to a spreading state and continues to increase in adhesion area until it reaches a fully saturated state (6). The increase in cell contact area during spreading is driven by specific cell-surface adhesion bonds, as well as nonspecific interactions (1).



**Figure 2.1** Stages of typical cell spreading. Initially, cells adhere to the extracellular matrix through individual contacts, such as blebs or filopodia. Then, moderate adhesion occurs, followed by fast lamellar spreading. Finally, cells reach a fully saturated spreading area.

With recent advancements in technology, multiple microscopy techniques have been developed which allow for the direct visualization of cell-substrate interactions during spreading. These techniques (which will be further discussed in section 2.3) have created a large field dedicated to understanding the relationship between cell spreading and disease. In particular, understanding both the chemical and physical components involved in cell spreading can allow for more tailored approaches to studying and treating related injury and disease.

### **2.1.2 Physiological relevance**

#### ***Embryonic development***

Cell spreading and migration are two vital components of embryonic development and contribute most specifically to the stages of gastrulation and organogenesis (7). Due to the importance of proper neural crest migration and neural tube formation in the development of the central nervous system, a vast amount of focus over the past 50 years has been placed on understanding the mechanisms by which cells collectively migrate during neural crest cell formation (8). Methods used to evaluate neural crest migration typically involve tagging and observing the localization and regulation of specific antibodies (9, 10) and modifying gene expression (11-13) in order to identify critical signaling mechanisms and proteins involved. These techniques and others have led to a significant understanding of the complex signaling pathways and gene regulation involved in neural crest cell migration (11, 14) however, much still remains unknown about the biophysical processes involved in embryonic development. For example: How does the mechanical environment of the migrating cells contribute to development and possibly disease? Do these mechanics differ among species? and Are mechanical and

signaling pathways restricted to embryonic development or can they be utilized to treat developmental disorders or abnormalities postnatally? Understanding the mechanics of cell-substrate interactions and the role of the surrounding environment during embryonic development will contribute significantly to the understanding of such a complex phenomena and will aid in the development of molecular therapeutics which may incorporate cell signaling to induce or prevent specific cell differentiation or behavior.

### ***Cancer metastasis***

Cancer metastasis is a complex phenomenon involving the migration of cancerous cells from one organ or part of the body to a new more distant organ or body location. This multi-step process initially starts with cells which leave the primary tumor and invade nearby blood vessels and tissue. Traveling through tissues or the blood stream allows cells to leave the vessel or tissue at a more distant location and establish new colonies far from the primary tumor (15). All of these steps require critical signaling and spreading mechanisms which are still not entirely clear. Metastasis is one of the greatest challenges when treating cancer patients for numerous reasons, including the inability to accurately distinguish metastatic-prone tumors versus ones that are less likely to progress to a metastatic state (16), the variability of metastatic-suppressor genes among cell and cancer types (17), and the variability of metastases methods (i.e. via the blood or lymphatic systems) as well as the variability of places in which metastases can occur. Cancer metastasis is the cause of 90% of human cancer deaths (18). This substantial statistic has resulted in an annual budget of more than \$4.8 billion by the U.S. National Institutes of Health (19). Although many different research approaches are taken to understanding cancer metastasis and potential treatments, a more complete understanding

of the role of cell spreading during metastasis would greatly contribute to the development of potential therapeutics. For example, preventing cancer cells from migrating away from the primary tumor, inhibiting cancer cells from penetrating vessels or tissue, or preventing cancer cells from escaping the blood vessels may all be ways to impede the migration of cancer cells.

### ***Immune response***

Numerous cell types involved in the body's innate immune system, including neutrophils, macrophages and monocytes require cell spreading, adhesion and motility to perform their proper function in the immune response cycle. Neutrophils are the first line of defense against infection and inflammation and require specific chemo-attractive cell signaling which encourages the neutrophil to leave the blood stream and attach to the endothelial cell wall (15). This endothelium attachment is then followed by the transmigration of the neutrophil through the cell wall and into the intima of the blood vessel where the neutrophil identifies the source of infection through chemoattractive signaling. The neutrophil uses chemotaxis to migrate towards the source of infection and phagocytoses the foreign material (15). Similar to neutrophils, macrophages are another part of the innate immune system that use phagocytotic mechanisms to engulf foreign material (20). These cells recognize specific antigens (typically from T-cells) that identify non-native materials, which stimulate macrophages to migrate towards the signal and engulfs the material (20). In general, these phagocytotic components of the immune response system first require proper identification of foreign material or the site of infection (through cell-signaling), followed by appropriate adhesion, spreading and migration behavior to ensure that the immune response cell can translocate to the site of

infection and destroy the material through phagocytosis. Abnormalities in the proper migration of immune cells can result and/or contribute to devastating diseases including psoriasis, Crohn's disease, rheumatoid arthritis, multiple sclerosis, Alzheimer disease and juvenile diabetes (21). A substantial amount of research has been focused on understanding optimal leukocyte migration behavior in order to develop therapeutic strategies that may aid in the treatment of immune response disorders (21, 22). For example, one recent variable of interest is the substrate stiffness, since changes in the surrounding environment that occur during disease stages, such as the hardening of arteries in atherosclerosis (23, 24), can dramatically affect neutrophil migration and immune response (25). Understanding the way in which the spreading and migration of immune system cells is affected by chemical and physical changes in the environment can significantly contribute to the advancement of therapeutics for immune response disorders and diseases (such as those mentioned above) which are affected or caused by the improper migration of immune cells.

### **2.1.3 Basic principles of cell spreading and migration**

Typical cell spreading behavior (illustrated in Figure 2.1) involves an initial binding of matrix ligands. When cells are plated onto a substrate coated with an extracellular matrix (ECM) protein, the cells probe the substrate surface by extending small protrusions, such as filopodia, lamella (6) or blebs (26, 27). During this portion of the spreading process, the cell exhibits a lag period where there is no substantial increase in spreading area as the cell probes the surface and eventually adheres. The duration of this lag period is inversely related to the concentration of ECM molecules present on the surface (28), and the time spent in suspension prior to plating (26). Next, the cell spreads

rapidly due to the formation of an actin-rich lamella which extends continuously from the periphery of the cell (6). Because cell volume and surface area remain constant during normal cell spreading (6) there comes a point in the spreading process where the excess membrane area (previously present when the cell was in a more spherical state) is depleted as the cell spreads fully on the substrate. This saturation of spreading area is typically when cells begin to polarize and have the potential to migrate (6).

Although the mechanisms involved in cell migration are cell-type dependent, with the exception of ameboid-like cell movement (29), typical cell motility consists of four basic events (6, 15, 30). A simplified schematic of basic migration is illustrated in Figure 2.2. Initially, cells extend a lamellipodium as they spread across the substrate. This actin-rich cellular feature extends in the direction of migration. Actin polymerization forces at the leading edge of this cell encourage the protrusion of the lamellipodium (31). Next, the extended lamellipodium forms new focal adhesions, which link the F-actin network to the ECM and trigger a plentitude of structural and signaling proteins (32, 33). These leading edge protrusions are coordinated with rear-end detachment through acto-myosin contractile forces (34). The acto-myosin and extracellular adhesion involved in this migration process are described as spatially and temporally coordinated (35), with migration shown to be optimized through feedback between acto-myosin and adhesion systems (30).

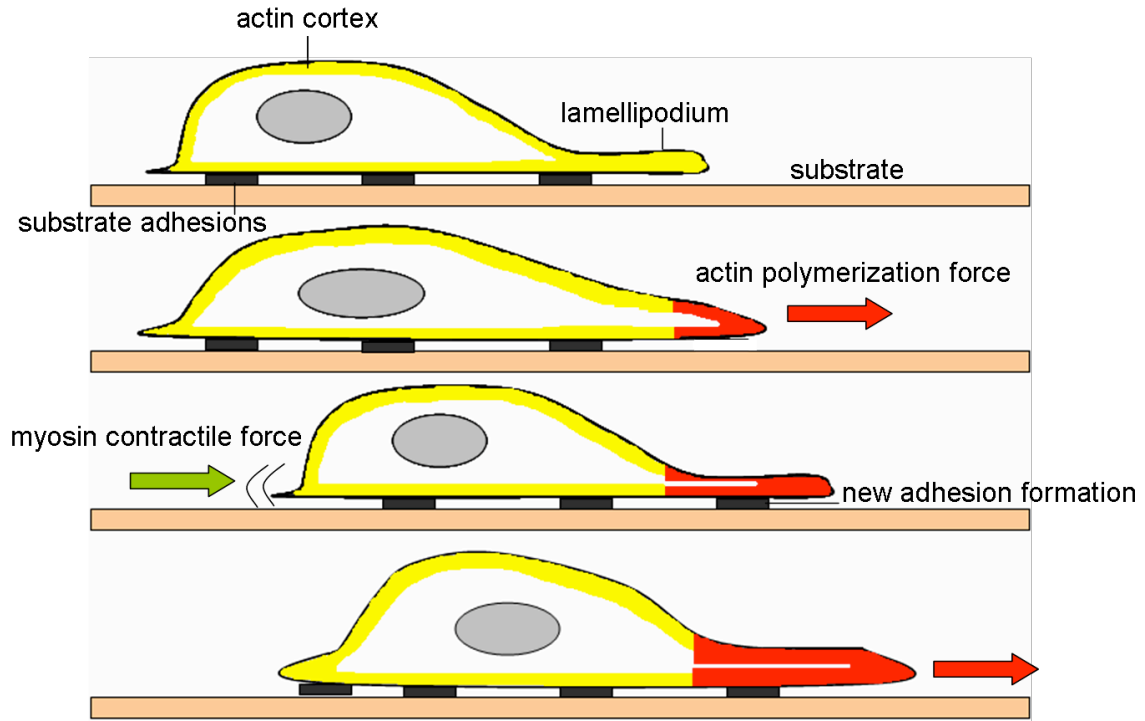


**Figure 2.2** A simplified schematic of cellular migration. Initially a spread cell extends a lamellipodium, which due to the increase of actin polymerization forces at this leading edge, cause the lamellipodium to extend. These actin-based leading edge forces are coupled to rear-end retraction due to myosin contraction in the back of the cell. When the leading edge forces ahead, new adhesions are formed at the leading edge and the detachment in the rear allows the cell to move forward. These actin-polymerization forces continue, and the coupling to rear-retraction allow for a smooth migration process. (Adapted from (15)).

### ***Effect of ligand concentration, substrate stiffness and dimensionality***

Cell spreading and migration behavior can be affected by numerous parameters including the concentration of ECM proteins (36-38), substrate stiffness (39-41) and dimensionality (42). A mathematical model proposed almost 20 years ago predicted that an increase in adhesion strength would induce a biphasic response in migration speed (43). This has since been supported experimentally by increasing and decreasing the concentration of ECM proteins present on the substrate during *in vitro* cell spreading experiments, revealing a biphasic dependent of cell migration velocity with increased

adhesion (36-38). Although the biphasic curve may be shifted due to cell type, ECM protein, and concentration variation, these experiments suggest that cells exhibit an optimal migration speed at some intermediate adhesion strength. More recently, it has been illustrated that this optimal migration involves an intricate relationship between the activity and organization of actin, myosin and focal adhesion assembly and disassembly (30, 44).

In recent years, it has also been shown that cell morphology, spreading and migration behavior can be greatly influenced by substrate stiffness (25, 39-41, 45). Cells that respond to changes in the substrate stiffness are termed “mechanosensitive” and this behavior has proven very critical in the development of cell scaffolds and biomaterials (46, 47), since cells appear to adopt their physiologically appropriate morphology when cultured on materials that mimic the environment of their native tissue (45, 46). Remarkably, substrate stiffness not only affects the migration and morphology of various cell types, but can also direct stem cell lineage (45). When mesenchymal stem cells (MSCs) are cultured on soft substrates, which mimic brain tissue, they differentiate into “neuron-like” cells which express neurogenic markers and stain positive for neurofilaments and axon-specific proteins (45). In contrast, MSCs cultured on stiffer materials, such as that which mimic muscle or bone, express myogenic or osteogenic markers, respectively (45). The ability to induce stem cell lineage through mechanical modification of the substrate has vast implications in the fields of biomaterial development and stem cell therapies (45, 47).

Along with ECM availability and substrate stiffness, the dimensionality and topography of cell’s environment is of additional importance in regulating cell behavior,

migration and spreading. Cells migrating in 3D have a less apparent lamellipodia compared to those extending on 2D surfaces (48), express different matrix adhesion molecules and focal adhesion constituents (49), and receive different directional cues (42). Although many have previously argued that 3D models better mimic the native environment of most cell types, there are numerous caveats to using 3D models, such as difficulties regulating pore size, matrix stiffness, and ligand density, as well as developing efficient microscopy methods to visualize cell migration (42). Recently, Doyle *et al* have developed a 1D matrix approach that presents epithelial cells with a highly controlled concentration of ligand presented to the cells in aligned stripes (42). Their results illustrate that this 1D environment mimics that of the 3D fibrillar nature, and provides a new platform to evaluate cell migration in a more “3D” nature without the associated difficulties.

In sum, it is apparent that cell migration and spreading can be significantly affected based on the environmental factors the cell experiences during culturing. Therefore, when evaluating cellular behavior, it is critical to consider not only the effects of ligand concentration, substrate mechanics, and dimensionality, but also the native environment of the cell type. Neuronal cells are also affected by many of these parameters, however their migration and spreading behavior is strikingly different and will be considered separately in the following section.

## 2.2 Neuronal cell spreading

### 2.2.1 Introduction

Prior to spreading, neurons in culture originate as spherical cell bodies similar in appearance to non-neuronal cell types. When plated onto ECM-coated substrates, hippocampal (50), cortical (51) and PC12 (neuron-like cells) attach to the substrate and extend an actin-rich lamellipodia similar to that described for non-neuronal cells. Figure 2.3 illustrates the characteristic spreading behavior of pheochromocytoma (PC12) cells using interference reflection microscopy (IRM). This technique, which will be discussed in more detail in the following sections, allows for a detailed visualization of the cell-substrate contacts. During the spreading process, cells extend a lamellipodium as mentioned above. After time, the lamellipodium is breached and numerous filopodia appear on the periphery of the cell (T = 8 minutes in Figure 2.3, and (52)). Eventually, these filopodia coalesce to form neurites, which later differentiate into axons and dendrites (T = 30-91 minutes in Figure 2.3, and (53, 54)). Emphasis has been placed on understanding each individual component of this spreading process in order to fully comprehend neuronal polarization and axon development. The ability to direct axon specification would be valuable in neurological therapeutics and injury treatments (47).

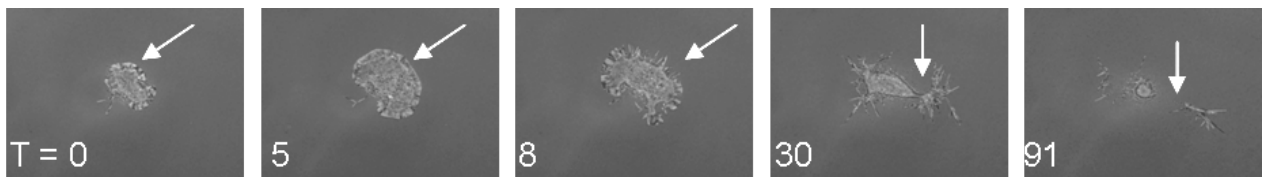


**Figure 2.3:** PC12 spreading using interference reflection microscopy (IRM). T = time in minutes. Lamella is present during initial attachment and spreading (arrows at T = 0-5). After time (T = 8), the lamellipodia breaches to form individual filopodia, which eventually coalesce into neurites (T = 30-91).

## 2.2.2 Physiological Relevance

### *Neurological migration disorders*

Developmental neurobiology has been a long studied field due to both the interest in the formation of such a complex biological system, as well as in understanding the origin of disorders that arise during aberrant development. Beginning from two weeks of human central nervous system (CNS) development through two years postnatal, deviations from standard morphological brain development events can result in specific neurological disorders (55). Neuronal and glial proliferation and migration are two characteristic events during weeks 9-24 of fetal development which can lead to neurological abnormalities if misperformed. In particular, defects occurring during the migration of cortical neurons may result in lissencephaly, also known as “smooth brain”, or other migration disorders, which typically result in mental retardation and epilepsy (55). Proper migration and extension during nervous system development requires axonal extension spanning great distances in order to reach proper synapses. There is significant importance in understanding how migratory events occur both during and after development in order to best reproduce the native environment when attempting to engineer therapeutics for trauma or disease.

### *Spinal cord injury and the glial scar<sup>†</sup>*

Central nervous system damage can be caused by injury or disease. Brain trauma and other acute disorders involve injury-induced apoptosis, while chronic disorders such as Alzheimer’s and Parkinson’s involve a slow degeneration of the cellular components of the CNS (56). In contrast, trauma and injury to the CNS results in tissue damage and

---

<sup>†</sup> Portions of this section were published as: Norman, LL, Stroka, K, and Aranda-Espinoza, H. 2009. Guiding axons in the central nervous system: A tissue engineering approach. *Tissue Engineering Part B*. 15(3) 291-305.

the subsequent formation of a glial scar. Findings involving reactive astrocytes involved in the glial scar suggests that it may have beneficial functions in helping to preserve and protect tissue function and to aid in the repair of the blood-brain barrier after mild or moderate spinal cord injuries (57, 58), as well as focal brain injuries (59). However, the glial scar is notorious for creating a barrier to regeneration (See Figure 2.4). A substantial amount of research has been placed on understanding how this response to injury prevents axon regeneration past this site (60).

The glial scar forms within weeks after injury and is largely composed of astrocytes (60-63). The scar formation begins within the first hours after injury with the appearance of macrophages and blood-borne cells, followed by a response in microglia, which begin to divide and upregulate signaling molecules and receptors (61). Along with microglia, macroglia infiltrate the lesion site, with astrocytes and oligodendrocytes being the major cell types (63). Although the role of astroglia cells in the CNS has not been fully described, they have been identified to play a role in multiple cell functions including CNS development, the CNS immune system, the uptake of neurotransmitters, and the preservation of tissue after injury (63). Astrocytes become “reactive” when aiding in tissue preservation responses, typically after one to two days post injury, and it is often thought that this reactive gliosis is the major barrier to axonal regeneration after trauma (60, 61, 63, 64). Astrocytes produce multiple types of proteoglycans, including heparan sulfate proteoglycan which encourages neurite extension, as well as chondroitin and keratan sulfate proteoglycans, which have demonstrated inhibition of neurite outgrowth (60, 63, 64). Chondroitin sulfate proteoglycans (CSPGs) have been identified in many *in vivo* injury studies including localization in the brain after stab wounds, in

explants of wounded striatum, in the spinal cord after dorsal root injury and crush injury, as well as in the fornix after transection (64). These increases in CSPG localization lead many to believe that these molecules may be the most significant components of regeneration-inhibition after CNS trauma. A very simplistic schematic of a CNS lesion and the subsequent glial scar is illustrated in Figure 2.4.

Due to the described complexity of the central nervous system, and the intricate formation of the glial scar following injury, it is doubtful that one specific strategy can reverse these traumatic damages. In order to incorporate numerous strategies into a single treatment, the field of tissue engineering emerges as a highly attractive approach to repair CNS injury and/or disease. The field of tissue engineering can be subdivided into multiple applications, including as a means of controlled drug delivery, as an extension of medical and surgical therapy, as a method to repopulate cellular content of tissues, and as a method to control the normal healing response of tissue (65). The intent of tissue engineering as a type of wound healing treatment involves numerous general principles, including the regulation of the normal healing process, the attempt to replace cellular components of disease tissues, and the controlled release of chemical or drug treatments (65). These principles have allowed the tissue engineering field to emerge as an exciting avenue in the pursuit of CNS repair in attempts to regulate axon regeneration.

Development of effective synthetic biomaterials for neural regeneration involves, among many other issues, a complete understanding of how the mechanical properties of the material affect cellular behavior and response. In particular, significant attention has been focused on how the stiffness and topography of the biomaterials affect neurite outgrowth. However, it is also essential to consider signaling mechanisms that are

occurring at the injury site. Thus, in addition to studying the physical properties of potential biomaterials for neural regeneration, it is also necessary to look at how the biochemical composition of the environment affects axonal outgrowth, since both variables contribute to neuronal migration, differentiation and survival.

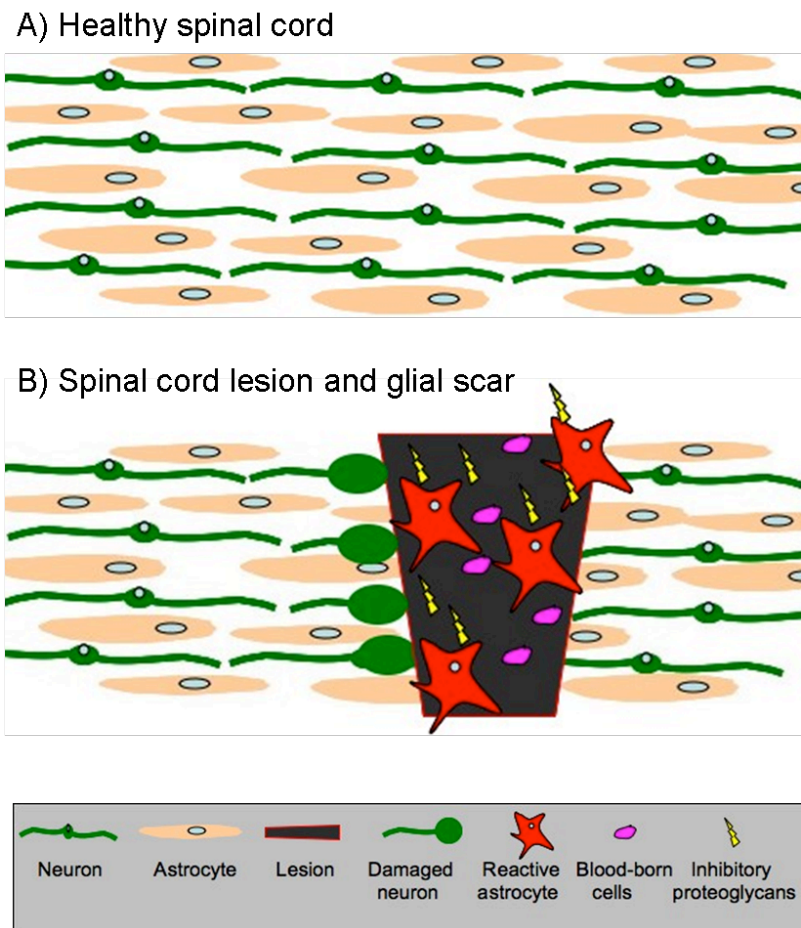


**Figure 2.4** Schematic representation of spinal cord injury and the formation of a glial scar. A) A simplistic representation of a healthy spinal cord track, containing synaptic neurons and astrocytes. B) After a lesion in the spinal cord, astrocytes become activated and initiate a signaling cascade which produces multiple proteoglycans which repel nearby axons. The non-permissive chemical and physical properties of the glial scar prevent the axons from reaching their proper synapses beyond the lesion.

### 2.2.3 Basic principles of neuronal spreading and migration <sup>†</sup>

#### *Effects of environmental stiffness*

One approach in understanding the regeneration of neurons is to examine how the environment of the cells affects their behavior. This understanding is extremely important for the development of synthetic biomaterials that will guide neuronal growth. Neural stem cells in particular have displayed the capability to modify differentiation and self-renewal capabilities based on the substrate modulus and biochemical environment (66). Neuron-like (i.e. PC12) cells have also been shown to be affected by substrate stiffness, but not all neuronal subtypes behave similarly, and not all biomaterials produce the same effects. For example, when grown on polyacrylamide (PA) gels coated with fibronectin, PC12s display longer and more branched neurites, as well as a greater percentage of cells with neurites, on stiffer gels ( $10^2 - 10^4$  Pascals [Pa]) (67). Meanwhile, PC12s on PA gels as soft as 10 Pa possess few, short, and unbranched neurites (67). In contrast, a separate study evaluating neurite extension on polyethylene glycol (PEG) hydrogels ranging in stiffness between 75-400 kPa illustrates that PC12s have the greatest degree of neurite extension on less stiff gels (68). Although in the presence of neurotrophic factors PC12s are capable of differentiating into sympathetic-like neurons (69, 70), it would be interesting to identify whether similar behavior occurs using primary neurons.

Another study investigated both PA gels and fibrin gels of varying stiffness, and optimal neuronal growth of rat cortices occurs on flexible fibrin gels of stiffness in the range of intact rat brain, which is several hundred Pascals (71). Dorsal root ganglia

---

<sup>†</sup> Portions of this section were published as: Norman, LL, Stroka, K, and Aranda-Espinoza, H. 2009. Guiding axons in the central nervous system: A tissue engineering approach. *Tissue Engineering Part B*. 15(3) 291-305.

(DRG) in three-dimensional collagen gels (72) and three-dimensional agarose matrices (73) possess maximum length of neurites at lower concentrations of collagen (softer gels), while cortical neurons on very soft hydrogels have low viability (74). It has also been shown that while primary spinal cord neurons thrive on soft PA gels coated with poly-D-lysine and Matrigel, glia are unable to survive on the same soft PA gels (75). Thus, it may be possible to use hydrogels to reduce scar tissue, and substrate stiffness could be used as a method to encourage growth of neurons while stifling growth of inhibitory glial cells.

### ***Effects of substrate topography and dimensionality***

In addition to substrate stiffness, other physical features of the cellular environment also influence cellular behavior. For neurons, these features include topography (74, 76-81), fractional porosity and pore size (75, 82), hydrophobicity or hydrophilicity (83-85), as well as swelling behavior, interfacial tension, surface to volume ratio, and viscoelasticity (82). Also, cellular behavior depends on whether the neuronal environment is two-dimensional (e.g. artificial substrates) or three-dimensional (e.g. tissue-engineered scaffolds) (86, 87). It has been well-established that 3D matrices are much more effective in stimulating neuron growth than are 2D substrates (86, 87), most likely because they more closely mimic the native environment of the cells, allowing for innate behavior and function. Recent results, however, have suggested that this preference may vary when neurons are presented with multiple options (88). Kofron, et al. (88) developed an *in vitro* system designed for the observation of outgrowth behavior in the simultaneous presence of a 2D and 3D environment. For dorsal root ganglion (DRG) neurons cultured at an interface between a 2D glass slide and collagen

gel, the majority of neurite growth was visible at the glass/gel interface. Interestingly, although there was penetration into the 3D gel, neurites extending from the interface cultures were not as long as those which extended on patterned 2D laminin surfaces. This study suggests that neurite extension may actually be slowed due to the complexity of the interface environment and the multiple options provided to the neurites (88). In addition to dimensionality, further considerations in the design of biomaterial scaffolds for axon regeneration include biocompatibility, biodegradability, sterilization, and the ability of the scaffold to conform to the dimension of the implantation site (89).

Physical topographical guidance has been shown to be an effective method to enhance axon outgrowth. Many studies on the effects of topography use gels of varying chemical composition which have been micropatterned to contain grooves of different height, thickness, and depth. Those grooves can act as channels to guide the growth of axons in a preferred direction. Smaller channels with widths of 100  $\mu\text{m}$  in poly(lactide-*co*-glycolide) (PLG) are more effective than larger channels in neuronal guidance and result in longer extension of primary neurites as well as less secondary branching (79). Murine embryonic cortical neurons, when faced with a step in height on poly-D-lysine (PDL)-coated PDMS, minimize their turning angle when faced with deeper grooves, while in shallower grooves they are able to extend into or out of the channel (80).

It is also possible for rat DRG neurons to extend neurites over grooves on polydimethylsiloxane (PDMS) with no underlying solid support (76). Interestingly, this study also reports that neurons are able to migrate into a groove, extend neurites to either side of the groove and up onto the plateau, and pull the soma of the cell up onto the plateau. The experimental conditions which favor the highest number of these “neuron

bridges” are a cell density of 125,000 cells per sample, groove depth of 50  $\mu\text{m}$ , groove width of 30  $\mu\text{m}$ , and plateau width of 200  $\mu\text{m}$  (76). These studies indicate that small surface changes can affect axon behavior, and therefore, topography can be utilized in biomaterial development in designing pathways for which axons extend in a more directed manner.

Several studies also combine topographical features with other mechanical or biochemical features. One such study investigated murine embryonic cortical neurons on PDMS with grooves of varying depth and with coatings of either PDL or Matrigel (80). PDL was more conducive than Matrigel for adhesion and neurite outgrowth, and a preference for the straightest path possible during axon extension was also shown. When neurons are presented with a conflict of these preferences, axons chose to extend into the Matrigel, and when the only straight pathway is non-permissive, axons take the path which minimizes the turning angle (80). Another study of PC12s on PDMS combined effects of microtexture (consisting of micro-islands in a square array) with mechanical strain (78). For both smooth and microtextured substrates, lower mechanical conditions (i.e. low strain at high frequency or high strain at low frequency) result in neurons with more and longer neurites, while higher mechanical conditions (i.e. high strain at high frequency) result in fewer and shorter neurites and lower cell density. Meanwhile, the lowest mechanical condition (i.e. low strain at low frequency) shows a significant increase in neurite length on the microtextured gel (78). Thus, the effects of topography seem to be most influential to neurite outgrowth under low mechanical conditions. Topographical features have also been combined with DNA drug delivery, and controlled

release of neurotrophic factors into guidance channels has shown to increase the effects of optimal topographical conditions (79).

Varying mechanical and topographical properties have also been combined with biochemical cues, in particular, neurotrophic factors, to better understand axon outgrowth in heterogeneous structures. Evaluating the benefit of neurotrophic factors within a matrix is done by either linking the growth factor directly to the matrix or by simply adding the factors into the cell medium. The combination of multiple neurotrophic factors supplied simultaneously has shown interesting results, which should be considered when designing heterogeneous materials. In addition to neurotrophic factors, the addition of ECM molecules, cell adhesion molecules, and cells native to the injury site have all been of significant importance in attempts to recreate the most optimal environment for axon regrowth.

### *Neuronal guidance cues*

Once the importance of neural receptors was identified, specific detail has been placed on how binding to these receptors triggers the internal signaling necessary for axonal extension; however, no concrete understanding has been defined. Recent evidence has supported that neural cell adhesion molecule (N-CAM), N-cadherin, and L1 stimulate neurite outgrowth through fibroblast growth factor receptor (FGFR) activation in neurons. In particular, N-cadherin-stimulated neurite outgrowth is inhibited from FGFR blocking agents (90-92) and all the major N-CAM isoforms have been illustrated to interact with the FGFR complex (93).

Along with CAMs, detailed studies have been placed on the signaling involved with extracellular guidance cues identified to guide the neuronal growth and axonal

extension. Guidance cues have been identified to play a role during embryonic development when neuronal migration is necessary in order to establish signaling pathways and neuronal connectivity. The guidance cues may be either attractive or repulsive for axons and neurons. While the current picture of guidance cues and their receptors is not complete, eleven molecules and receptors have been at least partially characterized (94). The best understood guidance cue families include the semaphorins, netrins, slits, and ephrins. Attractive guidance cues come from some netrins and ephrins, yet semaphorins, netrins, slits and ephrins have all illustrated repulsive mechanisms for steering axonal and neuronal migration (94, 95).

Semaphorins have illustrated repulsive properties in multiple cell types including facial, olfactory, motor, hippocampal, and dorsal root neurons and more (94, 95). The semaphorin family of proteins can be either secreted or membrane-associated (96) and were first identified in studies of growth cone collapse activity (94, 97). Like semaphorins, slits also act as repulsive guidance cues. These extracellular proteins were initially discovered in *Drosophila* by their ability to repel commissural axons from the midline (98). Interestingly, slits have the ability to repress the attractive action of netrins when bound to the slit receptor, roundabout (Robo) (95). Netrins are unique in that they can act over both long and short distances, have both repulsive and attractive actions through different receptor mediation, and were the first family of guidance cues to be identified in both vertebrate and invertebrate nervous systems (94, 95, 99, 100). Netrins exhibit their bifunctional qualities during development when motor neurons are repelled from the midline, yet commissural neurons are attracted to this area (94, 95). Ephrins, the fourth class of guidance molecules, also exhibit attractive responses but are primarily

seen as repulsive. There are two types of ephrins, A and B, with EphrinA being bound to the ECM, and EphrinB serving as a transmembrane protein (94, 95). Ephrins play critical roles during neuronal development by assisting axonal guidance into particular pathways and, more specifically, in retrieving positional information used during retinotectal development (101, 102).

The ability to understand the signaling molecules, ligands, and receptors active during neuronal development allows for a more complete comprehension of how to encourage axonal regeneration in the most native way. Both the stimulatory and inhibitory signaling mechanisms must be considered when engineering approaches and materials for use in CNS regeneration studies. Much interest has been placed on the pathways of axonal guidance and growth cone behavior, and concentrating on these pathways may be the best approach for incorporating growth factors into biomaterials. An example of this is including soluble factors within a matrix in which the signaling pathway response for neuronal growth to these factors is understood (103). Nerve growth factor released from polymeric implants has been shown to stimulate neurite sprouting in PC12s (104), while the controlled release of neurotrophin-3 from fibrin scaffolds increased neuronal fiber sprouting and migration into the lesion after ablation injury in rats (105). For further understanding of drug delivery methods in neural tissue engineering, see the review by Willerth and Sakiyama-Elbert (89).

### ***Growth cone signal transduction***

A vast amount of axonal regeneration literature involves the signaling molecules and pathways that activate and encourage the growth cone to migrate in specific directions. As described above, the repulsive and attractive characteristics of the four

families of guidance cues has been illustrated for multiple neuron cell types; however, one also needs to understand the steps that follow from guidance molecules to growth cone signal transduction. The key steps in the signal transduction process have been described as 1) binding of an extracellular molecule to a receptor on the growth cone membrane, 2) activation of effectors through receptor-cue complexes, 3) activation or inactivation of actin-binding proteins, and lastly 4) modulation of actin dynamics (95). The growth cone was first described by Cajal in 1890 (106), with more recent studies beginning to understand the cytoskeletal dynamics of actin and microtubules during motility (107) using modern high-resolution microscopy. Once the growth cone binds to an extracellular molecule and the effector is activated, these guidance cues can modulate actin dynamics during the migration process. It is necessary to understand the signaling behind this process in order to manipulate directed axonal extension after trauma. The signaling transmitted intracellularly after receptors on the growth cone interact with the described guidance cues involves the Rho family of GTPases. Rac, Rho and Cdc42 are three of these adaptor proteins which have illustrated close association with actin cytoskeleton dynamics in neurons (94) as well as other cell types (108, 109). Rac is responsible for actin-rich lamellipodia and promotes actin polymerization, along with Cdc42, at the leading edge of the growth cone. Similar to Rac, Cdc42 induces actin-rich filopodia, used for sensing the nearby environment. Unlike Rac and Cdc42, Rho mediates repulsive cues and is believed to contribute to retraction through acto-myosin contraction at the trailing end (94, 95). The complicated process of signal transduction pathways downstream of the Rho GTPases which regulates cytoskeletal organization is

described in detail by Guan and Rao (94), yet there is the likely possibility of more activity pathways that remain unknown.

### *Axon specification signaling*

Extracellular and intracellular signaling mechanisms are not only critical in the migration and extension of the growth cone, but also play a significant role in determining which neurite becomes the axon. Many studies aim to identify proteins which localize within the growing axon but are absent from the remaining neurites. These proteins are termed “polarity proteins” and are generally suspected to be involved in axon specification, in part through signaling to the cytoskeletal components such as actin and microtubules (110). Polarity proteins include GAP43, synaptic vesicle antigens, tau and L1 (50), as well as partitioning-defective (PAR) proteins PAR-3 and PAR-6 which localize at the tips of all neurites before differentiation, yet localize only in the axon of developing growth cones during polarization (110, 111). A tentative model for axon polarization and intrinsic signaling is described by Arimura and Kaibuchi (112) in terms of positive and negative regulation. It suggests that, during the transition from neurite to axon, there is a disturbance in the balance between positive regulation (membrane recruitment, protein transport, increase F-actin dynamics and microtubule assembly) and negative regulation (membrane elimination, degradation of proteins, decrease in F-actin dynamics, and microtubule catastrophe) (112). A neurite can elongate quickly and become an axon due to an imbalance of signaling caused by the activation of adhesion molecules and receptors, and the recruitment of signaling molecules (112). Arimura and Kaibuchi also describe a list of neuronal polarity-regulating molecules and models of positive and negative signaling (112).

Overall, signal-passed regeneration approaches involve one of three methods: 1) introducing new attractive molecules or increasing the amount currently present in the environment, 2) preventing inhibitory molecules or 3) influencing axons to regenerate in a previously inhibitory environment (61). The attractive and repulsive characteristics of the above-mentioned adhesion molecules, guidance cues, and transduction pathways have lately become incorporated into optimizing many engineering approaches for axonal regeneration. In particular, attempts to deliver both soluble and bound growth and neurotrophic factors have made important contributions to an understanding of axonal regeneration in the CNS (105, 113, 114). Attempts have been made to supply organized and even patterned quantities of neurotrophic factors, growth and adhesion molecules. Direct supply of guidance cues have been used in collagen implants containing the neurophin NT-3, which attracts regrowth of neurons and illustrates partial functional recovery in the adult rat spinal cord (113). With the recent attention of microprinting techniques, patterned arrays of neurotrophic factors have been frequently used on experimental regeneration substrates. Microprinting has been used to direct axons in specific directions by stamping attractive proteins, ligands, and growth factors, in a pathway desired for axonal extension (68, 77, 84, 115). The reverse can also be performed, with microprinting being used to create repulsive areas, including repellent backgrounds, which discourage cell attachment and movement in specified areas (116).

## ***2.3 Methods for detecting cell-substrate interactions and spreading***

### **2.3.1. Bright field microscopy**

Bright field (BF) microscopy is a traditional optical microscopy technique which uses transmitted white light to visualize a sample. Although BF is useful during experiments focused on cell morphology or basic migration changes, it does not supply information on cell-substrate interactions. Typically, with an inverted microscopy system, BF microscopy is often combined with more substrate sensitive techniques, such as interference reflection microscopy (IRM) or total internal reflection fluorescence microscopy (TIRF). Combining these techniques allows for the observation of both the basal and apical surfaces during processes such as cell spreading and migration (26, 27, 117).

### **2.3.2. Interference reflection microscopy**

IRM is a method used to detect surface interactions based on the interference from light reflected off the sample versus the substrate (118). The interference correlates to images illustrating varying degrees of dark and light zones. IRM images can be distinguished based on gray values since the greater the refractive index of the membrane, the lower the reflectivity, and thus the site of cell contact in direct apposition to the glass will appear darker than the cell free background (118, 119). Areas of the cell further from the substrate appear with lighter shades of gray. Based on the principles of IRM, spreading cells exhibit varying intensity, which is related to the distance between their membrane and the surface of the substrate. This contrasts well with the background, which maintains a primarily uniform gray intensity.

IRM is an advantageous method for evaluating cell-substrate dynamics, versus, typical BF observations, which cannot efficiently illustrate the complex substrate interactions during processes such as spreading and migration.

### 2.3.3. Total internal reflection fluorescence microscopy

TIRF follows similar principles as the IRM technique. Briefly, a thin layer of illumination, also termed an “evanescent field”, is produced by exiting a light beam into a glass coverslip at an incidence angle greater than some “critical angle” in order for the beam to totally reflect rather than refract through the interface (120). Figure 2.5 represents an illustration of the TIRF scheme. As mentioned, the incidence angle,  $\theta$ , must be larger than the critical angle,  $\theta_c$ , for total internal reflection to occur. The evanescent field allows for the light to excite fluorophores near the surface ( $\sim 80\text{nm}$ ) while avoiding the excitation of those fluorophores which are not close to the substrate surface (70).

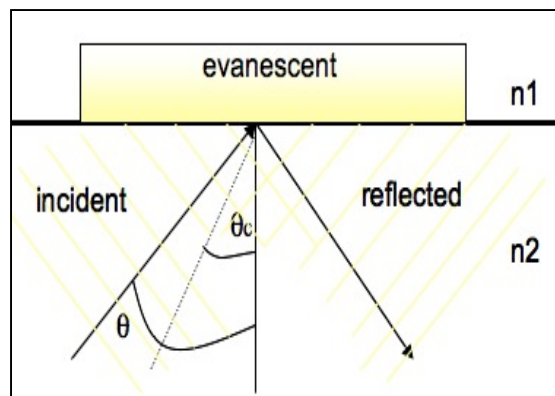


**Figure 2.5** Schematic representation of total internal reflection fluorescence (TIRF) microscopy. The refractive index  $n_2$  must be greater than  $n_1$ . Also, the incidence angle  $\theta$ , must be greater than  $\theta_c$ , for complete internal reflection. The evanescent field decays as the distance from the substrate increases, allowing for excitation at only  $\sim 80\text{nm}$  from the surface. (Adapted from (120)).

Due to the excitation of such a small cell-surface area, TIRF has proven a useful tool in approaches aimed at the understanding of cell dynamics at the submembrane level, including actin kinetics (70, 71) and spreading behavior (72).

The often transient nature of proteins during processes such as cell spreading and membrane modification (117) and neurite extension and retraction prior to axogenesis (121) requires live time-lapse studies in order to receive the greatest insight into specific protein dynamics, and therefore illustrates a critical need for TIRF microscopy.

Although IRM is a valuable tool in identifying cell-substrate adhesion and even identifying focal adhesion sites as mentioned above, a caveat of this technique is that dark adhesion patches can sometimes also appear due to factors other than focal adhesion, such as membrane fluctuations and cell movements. Specific adhesion sites can be quantitatively measured by labeling a specific focal adhesion protein of interest and observing the cell simultaneously with TIRF and IRM, as shown in Figure 2.6. Figure 2.6 illustrates a bovine aortic endothelial cell using IRM which is overlaid with the corresponding vinculin (a focal adhesion protein) immunostaining image. The white arrows illustrate selected areas, which appear dark in adhesion; however, these spots lack vinculin expression. Although these areas do indeed represent tight adhesion with the surface (based on the principles of IRM), it does not always correlate with focal adhesions. In sum, TIRF is a more quantitative method to evaluate specific adhesion parameters such as focal adhesion morphology, size and distribution, while IRM remains a valuable tool for identifying spreading area and migration behavior.

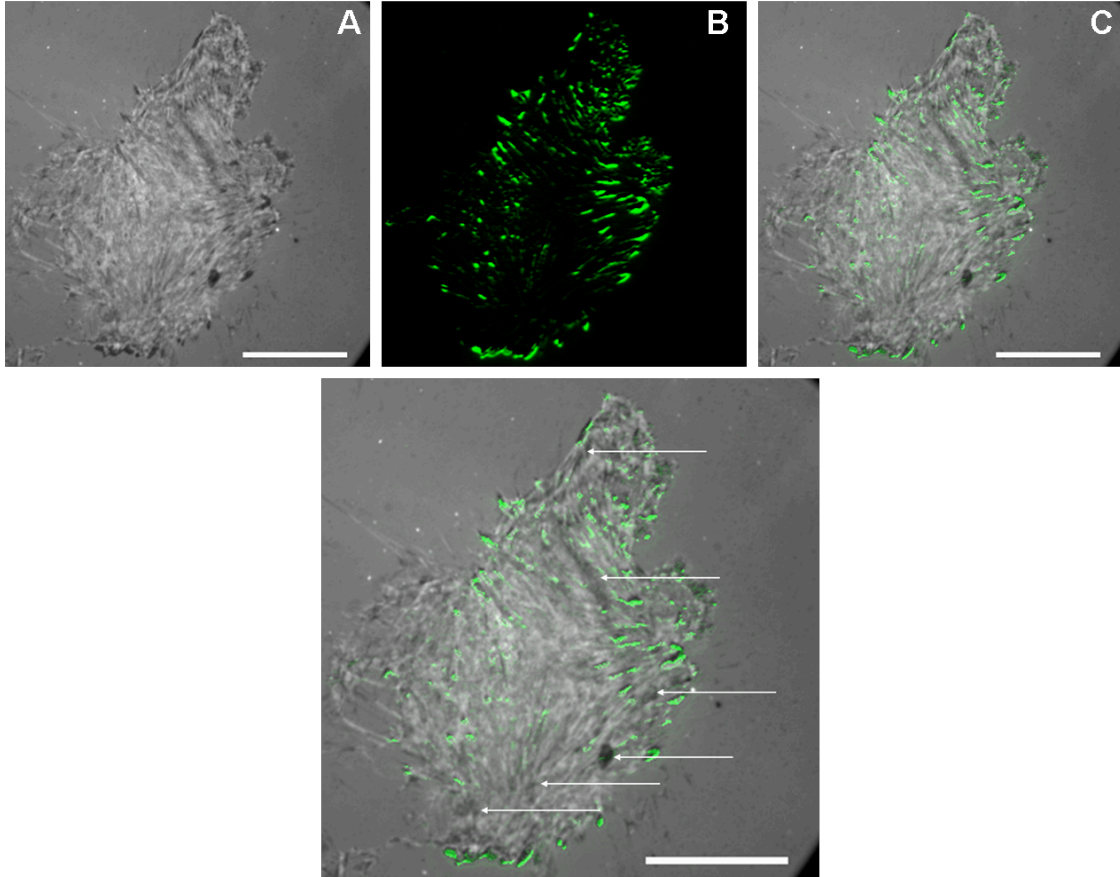


**Figure 2.6** Comparison of adhesion using IRM with vinculin immunostaining. Cells were fixed and observed using IRM (A), and stained for vinculin and observed using TIRF microscopy (B). An overlap of the images is shown in (C) and magnified in (D) to illustrate the association of vinculin at places of tight adhesion. Arrows identify areas of the cell that are dark and therefore identify close adhesion using IRM, yet vinculin staining is not apparent. Scale bar is 25  $\mu\text{m}$ .

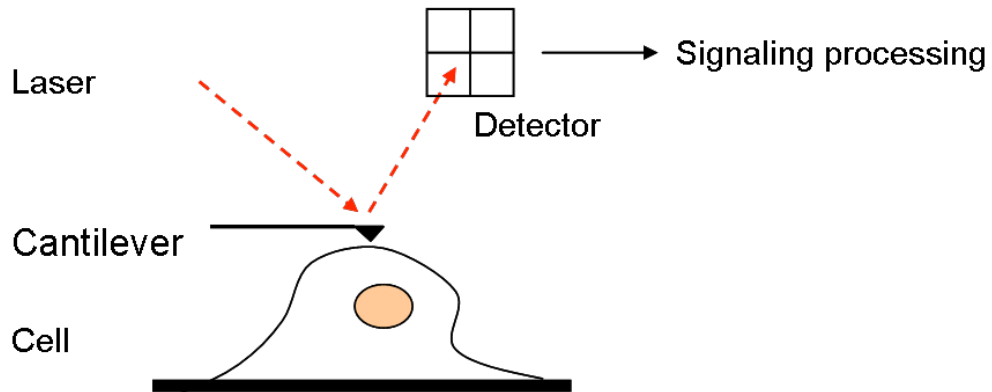


**Figure 2.7** Schematic representation of atomic force microscopy (AFM). Briefly, a cantilever is positioned on top of the cell or sample and a laser is focused onto the tip of the cantilever. The deflection of the laser changes as the cantilever scans the sample area. These deflections are detected using a photodiode detector and their positions are recorded. These signals are used to recreate a 3D reconstruction of the sample image and can also be used to measure local cellular nanomechanical properties.

#### 2.3.4. Atomic force microscopy

Atomic force microscopy (AFM) is a technique that has acquired substantial importance in the studying of biological systems and cellular mechanics (122). In brief, AFM involves directing a laser onto the tip of a small cantilever which comes in contact with the sample. As the sample is probed or scanned, the deflection of the laser is recorded. These recorded laser deflections can be used to recreate a topographical image by moving the cantilever across the sample or can be used to determine various mechanical properties of the sample, such as the elastic modulus, by tapping the sample and recording the change in laser deflection (123, 124). A schematic of AFM is illustrated in Figure 2.7. AFM has the remarkable ability to evaluate and quantify mechanical and morphological characteristics of biological specimens and single cells in the nanometer range at high resolution while preserving samples in their natural aqueous environment (122, 125). In particular, AFM has been used to evaluate the elastic

properties of individual cells (126, 127), quantify mechanical properties of tissues (124, 128), evaluate protein-protein interactions (129, 130), and determine binding forces between single molecules (131).

## ***2.4 Summary***

Cell spreading and migration are two critical phenomena vital to embryonic development, cancer metastasis, immune response, and wound healing. Recent developments in advanced microscopy techniques have contributed to a substantial understanding of cell spreading behavior for both neuronal and non-neuronal cell types. However, a more thorough understanding of cell-substrate interactions is necessary to fully understand methods of cell spreading and migration in relation to disease and to optimize the development of tissue engineered scaffolds. This work aims to understand cell spreading and cell-substrate behavior for endothelial and cortical neurons in order to develop a more comprehensive understanding of how cells interact with their substrates during critical biological phenomena such as cardiovascular disease and neurological development and trauma.

### **3 Characterization of the initial stages of endothelial cell spreading and blebbing<sup>†</sup>**

#### ***3.1 Introduction***

Blebs are spherical outgrowths of the plasma membrane (PM) that occur upon membrane detachment from the underlying cytoskeleton. Traditionally viewed as a sign of apoptosis, blebs are increasingly emerging as dynamic features connected to dramatic cellular reorganization, with a possible role in cell motility (132). Blebs have been observed during spreading (133-136), mitosis (135, 137, 138), and *in vivo* (139) and *in vitro* cell migration (140, 141). The mechanics of a single bleb is beginning to be well understood (108, 142, 143). Blebs are nucleated by the loss of PM-cytoskeleton adhesion, possibly due to the increase of cytoskeleton contractility. The freed membrane inflates rapidly (within 30 sec) into a spherical bleb (134, 135, 142-144). Bleb expansion stalls either because of a drop of pressure inside the cell, or after *de-novo* assembly of an actin cortical layer on the bleb membrane. First, transmembrane actin-binding proteins localize within the membrane of the bleb, followed by polymerization of actin at the membrane of the bleb and lastly, localization of motor proteins, in particular, myosin II (108). A new contractile cortex is formed which retracts the bleb toward the cell body within a few minutes (108, 135, 142, 143). Cellular blebs can also be driven by external mechanical perturbations such as an hyperosmotic shock or micropipette suction (145), and have been identified as obligatory features following detachment of adhered cells (133-136, 146). However, blebs have not yet been connected to the global mechanical

---

<sup>†</sup> Portions of this section have been submitted for publication as: Norman, LL *et al.* Cell blebbing and membrane area homeostasis in spreading and retracting cells. (Under Review, April 2010).

homeostasis of the cell. We demonstrate this connection here by observing the blebbing activity of adherent cells abruptly detached from their substrate, and we further show the role blebs play in the initial stage of adhesion.

The dynamics of cell spreading has been studied for many individual cell types including fibroblasts (5, 146) and neutrophils (2). Theoretical models of cell spreading have also been proposed (1, 147), where spreading results from a balance between a driving force from substrate adhesion and/or actin polymerization, and a viscoelastic force accompanying cell deformation. Broadly speaking, such an approach predicts a power-law where the cell-substrate contact area increases linearly with time (the cell then essentially behaves as a very viscous fluid), up to a saturation area, that depends on both cell and substrate. Membrane tension could play an important role in opposing cell deformation, and the regulation of PM surface area by endosomal recycling through endo- and exocytosis mechanisms is thought to be required for major changes of the cell shape during cellular processes such as mitosis (138) and spreading (148-150). In addition to bringing specific adhesion proteins to the PM, increased exocytosis during cell spreading helps to prevent an increase of membrane tension by bringing membrane material to the PM (150, 151), while endocytosis could play the opposite role during cell detachment (148, 149). Mechanically speaking, it appears probable that membrane recycling is crucial in preventing a large variation of the PM tension during major morphological cell changes (138, 150). We show below that blebs can also contribute to this mechanical homeostasis.

## ***3.2 Materials and methods***

### **3.2.1 Cell culture and substrate preparation**

Bovine aortic endothelial cells (BAECs) were purchased from Lonza Walkersville, Inc. and cultured in Dulbecco Modified Eagle Medium supplemented with 10% bovine serum, 1% 200 mM L-glutamine and 0.5% penicillin-streptomycin (referred to as BAEC medium). Cells were maintained at 5% CO<sup>2</sup>, 70% humidity and 37°C. Cells were passaged at 90% confluence, and used between passages 3-10 for experiments. Prior to each experiment, cells were starved of serum for approximately 16 hours and detached with 0.25% trypsin with EDTA. Glass bottom dishes (No. 1.5, MatTek Co.) were coated with fibronectin (FN) by incubating with 100 µg/ml FN (Sigma-Aldrich) at room temperature for 2 hrs. Dishes were rinsed three times with 1X PBS buffer prior to addition of cells.

### **3.2.2 Detachment and spreading experiments, and actin staining**

For detachment experiments, cells were plated on FN coated plates for 24 hrs in order to reach saturation. For rapid detachment, cells were trypsinized with 0.25% trypsin with EDTA, while trypsin with EDTA diluted 20:1 with BAEC medium was used for slow detachment. For spreading experiments, cells were plated onto new BAEC media filled FN coated dishes following the appropriate incubation time (0-120 min). An average of  $5 \times 10^3$  cells were plated per dish to ensure that single cells during spreading. For detachment and spreading experiments, one frame was recorded every 3-5 sec. To modify the number of blebbing cells without drug or osmotic treatment, cells were allowed to remain in suspension after trypsinization between 0-120 min prior to replating.

IRM and BF snapshots were taken for a minimum of 15 random cells per spreading time point. To observe the number of blebs per cell, BAECs were plated onto extremely soft ( $E \sim 260$  Pa), uncoated polyacrylamide gels (following methods described by Pelham and Wang (39), and as described in Appendix A). Individual cells were observed with multiple BF snapshots taken at each time point to ensure the identification of blebs on both the basal and apical surfaces. Cells were treated with  $80 \mu\text{M}$  dynasore (Sigma-Aldrich) for 10 min prior to plating and remained in the same concentration of the drug for the entire duration of the experiment. Using all captured planes, the numbers of blebs were counted for each cell.

For actin staining, cells were fixed for 20 min with 2% paraformaldehyde solution, and permeabilized with 1% Triton-X for 5 min. A 2% BSA solution was used to prevent nonspecific binding, and cells were stained with  $0.1 \mu\text{M}$  Phalloidin-TRITC.

### **3.2.3 Microscopy, imaging conditions, and data analysis**

As previously mentioned, interference reflection microscopy (IRM) is a method used to detect surface-to-surface distance. Typically, the areas of the membrane closest to the surface appear dark, while those further away look brighter; thus IRM is well suited for cell adhesion studies. Spreading and detachment experiments were performed using IRM, while the number of blebs per cell was observed using bright field microscopy. Imaging conditions are further explained in Appendix B.

The cell was identified using an algorithm based on fitting of intensity histograms which was implemented in IGOR-Pro data analysis software (WaveMatrix). For a detailed explanation of this method and the algorithms used to fit intensity histograms refer to Appendix C and (2). For statistical evaluations of spreading areas, IRM images

were analyzed using ImageJ (National Institutes of Health) software. The cell-boundaries were traced by hand and area was calculated using in-built ImageJ routines.

### ***3.3 Results***

#### **3.3.1 Blebs appear following rapid cell detachment**

We observed blebbing activity of adherent cells by imaging the cell region near the substrate using IRM. Figure 3.1 shows blebs in adhering BAEC observed with bright field (BF) imaging as well as phalloidin actin staining, and their distinctive appearance in IRM. Blebs appeared as spherical protrusions in BF and fluorescence microscopy and corresponded to uniformly dark circular adhesion zones when attached to the substrate, using IRM. Blebs had a similar morphology to those observed in fibroblasts (133, 137) and human melanoma cells (135, 142, 143), and their dynamics (extension and retraction rates) were also similar to those previously reported (108) even when interacting with the substrate, which indicates poor adhesion between blebs and the substrate.

Rapid cell detachment with trypsin (as well as detachment with EDTA without trypsin) leads to the appearance of numerous blebs. A typical process of moderately rapid cell detachment is shown in Figure 3.1B using IRM. In this particular case, blebs were first observed after 8.8 min (Figure 3.1B), and became more numerous and larger after 10 min. In our hands, the time of bleb appearance was arbitrary; however, the detachment area necessary for bleb appearance was consistent for cells of similar initial adhesion areas. Typically, blebs began to appear on detaching cells (N=6) after approximately  $78 \pm 11\%$  of the total adhered area was detached, and were observed on both the basal and apical surfaces using BF imaging. We also note that although blebbing is a common

occurrence upon trypsinization, cell blebbing is heterogeneous, with some cells lacking blebs completely and others possessing blebs of varying number and size. This variability is likely due to a variety of factors including the initial spreading area and tension, the stage in the cell cycle (although our cells are deprived of serum to minimize this effect), or differences among membrane-cytoskeleton attachments.

The appearance of blebs during detachment could be due to major disruption of the cytoskeleton structure. It could also be a way for the cell to deal with the large amount of membrane area that was transferred to the PM during cell spreading, and that will eventually be endocytosed (148, 149). We tested the role of the kinetics of cell detachment by using a lower concentration of trypsin. Interestingly, blebbing was not observed at all when cells were detached slowly over more extended periods of time (>50 min in our case). The time scale involved appears fairly large as compared to cytoskeleton remodeling times, but is rather consistent with the dynamics of membrane recycling (152, 153). In order to gain more insight on the relation between blebbing and membrane recycling, we studied the evolution of the blebbing activity of cells after fast detachment.

### **3.3.2 Endocytosis regulates cell blebbing**

Adhered BAEC were rapidly detached from their substrate using a high concentration of trypsin, and then placed on very soft polyacrylamide gels ( $E \sim 260$  Pa), without any extracellular matrix coating, making the substrate non-adherent. The number of blebs was counted using BF microscopy to monitor the evolution with time of the number of blebs per cell (Figure 3.2). For control cells, the average number of blebs remained fairly constant for the first 10-15 min of observation. After 15 min, we

observed a gradual decrease in the number of blebs per cell until 40-60 min, when the cells were no longer blebbing. The large characteristic timescale of the blebs disappearance suggests that the number of blebs is likely to be regulated by membrane internalization mechanisms such as endocytosis (148, 149). To test this hypothesis, we repeated the above experiment with cells treated after detachment with 80  $\mu$ M dynasore, an inhibitor of dynamin-dependent endocytotic pathways (154). Although the number of blebs did decrease slightly over the observed 90 min period, the majority of cells treated with dynasore were unable to completely reintegrate cellular blebs (Figure 3.2). Furthermore, cells treated with dynasore did not spread on any substrate, in agreement with results shown by others (154). We observed cells for up to 3.5 hrs during which the adhered area did not increase, while the majority of cells continued to bleb.

### **3.3.3 Role of blebs in cell spreading**

Finally, we established the influence of blebs on the kinetics of cell spreading. Adherent cells rapidly detached by trypsinization were (re)-plated after varying times of incubation (0-120 min), and their spreading area was captured every 5 sec by IRM (Figure 3.3). Cells plated immediately following trypsinization typically exhibited vigorous blebbing as illustrated in Figure 3.2B, while cells which remained in solution for 120 min prior to plating did not bleb at all (Figure 3.3A, Non-blebbing cell). Blebbing and non-blebbing cells exhibited distinctly different behaviors during the initial stage of spreading.

Non-blebbing cells displayed both filopodia and lamella (respectively, white and black arrowheads in Figure 3.2A) within the first 10 min of spreading. They spread quickly on the substrate, following the linear dynamics reported previously (1). On the

contrary, the initial substrate adhesion of blebbing cells occurred through individual bleb-adhesion zones (Figure 3.3A arrow), which grew and fused to form the adhered area of the cell. Because of constant bleb retraction, this process was very slow, and little increase of the adhered area was actually observed during the first 40 min of spreading. During this long lag spreading regime, the cell showed numerous blebs at the periphery of the adhesion zone which dynamically adhered and detached from the substrate. Lamella and filopodia became apparent after some time and initiated the fast spreading regime, after while blebs quickly disappeared from the PM. The timescale for bleb disappearance was similar for spreading and non-spreading cells Figure 3.2. This behavior illustrates that the reintegration of cellular blebs is independent of cell spreading, and it is more likely regulated by internalization mechanisms such as endocytosis (148, 149). Furthermore, the spreading rate in the fast spreading regime was similar for blebbing ( $33 \pm 17 \mu\text{m}^2/\text{min}$ , N=9) and non-blebbing ( $30 \pm 18 \mu\text{m}^2/\text{min}$ , N=9) cells), emphasizing that the major difference between the two spreading behaviors lies in the first 40 min of spreading, the time needed for blebs to disappear.

To support this claim, we incubated cells for varying time before re-plating them and then measured the area from IRM snapshots for a minimum of 15 random cells taken at each time point during spreading (Figure 3.3B). A lag was still observed for cells incubated less than 60 min, but the extent of the lag phase decreased with increasing incubation time, consistent with the view that the lag phase is connected with the presence of blebs. Cells incubated for 60 min or more quickly developed lamella and spread very quickly. Here again, the fast spreading regime was similar for all cases, whether it was preceded by a lag phase or not, as was also the final adhered area at

saturation. We examined the number of cells that were blebbing during the spreading process and found that the percentage of cells blebbing decreased with incubation time, with 92% of the T=0 min incubation cells blebbing, while only 62% and 33% of cells are blebbing after 30 and 60 min, respectively. Cells no longer bleb after 120 min of incubation.

### 3.3.4 Model

In order to quantify the relationships between blebbing, membrane recycling, and cell spreading in a more precise way, we used a general linear viscoelastic framework not restricted to cell spreading, to relate cell deformation to membrane tension. Blebs were taken into account by introducing formation and retraction rates that depend on membrane tension. This model is explained in more details in the supporting information (see Appendix D).

#### *Viscoelastic description of cell spreading*

Following previous works (1, 147), we use a linear viscous relationship between the cell deformation, measured by the area  $A_c$ , and the net driving force:  $\eta_c \partial_t A_c = \varepsilon - \gamma_m$ , where  $\eta_c$  is a dissipation coefficient,  $\varepsilon$  is the force (per unit length) driving the deformation, and where the membrane tension  $\gamma_m$  opposes deformation. In the case of cell spreading,  $A_c$  is related to the adhered area and the driving force  $\varepsilon$  includes both the adhesion energy between the PM and the substrate and a contribution from actin polymerization in the lamella (1).

Here, we assume membrane tension to be the only force opposing deformation (see below) leading to a saturation when it balances the driving force:  $\gamma_m = \varepsilon$ . The membrane tension itself is coupled to the deformation and is regulated by endo and

exocytosis. Furthermore, blebbing influences the membrane tension by sequestering membrane area. We show in Appendix D that these effects (sketched Figure 3.4) can phenomenologically be taken into account by modeling the PM as the viscoelastic body depicted in Figure 3.4B, consisting of the so-called standard linear elastic model, coupled with an element describing blebbing. The general relationship between the membrane tension  $\gamma_m$  and the total PM area  $A_m$  (which includes blebs:  $A_m = A_c + A_b$ , with  $A_b$  the area contained in blebs) reads:

$$\dot{\gamma}_m + \frac{\gamma_m}{\tau_m} = (k_1 + k_2) \dot{A}_m + \frac{k_2}{\tau_m} (A_m) \quad [1]$$

where tension and areas are defined with respect to the resting situation ( $\varepsilon = 0$ ,  $\tau \rightarrow \infty$ ). In the absence of blebs, the membrane crosses-over from a relatively stiff elastic body at short time to a much softer elastic body after a relaxation time  $\tau_m$ , identified with the characteristic time of membrane area homeostasis (of order 40 min for BAEC). As we show below, blebs appear if the membrane tension drops below a critical value.

### ***Bleb Statistics***

The life cycle of a bleb involves nucleation and growth, followed by the polymerization of a new actin cortex underneath the bleb membrane, and by bleb retraction. The whole process only takes a few minutes, and in the time scale of our observations (about an hour), it can be considered instantaneous. The average number of blebs per cell thus results from a balance between nucleation and retraction. The rate of bleb retraction depends mostly on the time needed to polymerize an actin cortex and recruit myosin, and can be considered roughly constant. The rate of bleb nucleation, on the other hand, strongly depends on membrane tension.

It has been shown ( (142), reviewed in Appendix D) that the energetics of bleb formation is mostly controlled by three physical parameters: internal cell pressure, the membrane-cortex adhesion energy and the membrane tension (see Figure 3.4C). While the former, partly built by acto-myosin contraction, promotes membrane cortex separation and membrane inflation, the latter oppose bleb formation. As a result, the bleb energy displays the characteristic features of a nucleation process; if the membrane area detached from the cortex ( $S_b$  in Figure 3.4C) is small, it rebinds without major inflation, but beyond a critical area corresponding to a particular nucleation energy, blebs steadily inflate. The smaller the nucleation energy barrier, the higher the probability to observe blebs on a given cell. It has been suggested that local increases of the cortical activity could be responsible for bleb nucleation (142, 143). As the nucleation energy depends on the membrane tension (linearly, see Appendix D), blebbing can also be triggered by a major drop in membrane tension, such as that expected upon detachment of a strongly adhered cell.

The rate of bleb nucleation is expected to grow exponentially with the nucleation energy barrier, hence with membrane tension. The fraction of the cell surface covered with blebs thus takes the general form (see Appendix D)

$$n_b = \frac{1}{1 + e^{\beta(\gamma_m - \gamma_b)}} \quad [2]$$

where  $\gamma_b$  and  $\beta$  are respectively the threshold tension for blebbing and the bleb nucleation sensitivity to membrane tension. They are expressed in terms of physical parameters in Appendix D. Equation [2] tells us that there should be no blebs for high membrane tensions, while blebs should saturate the cell surface ( $n_b \sim 1$ ) for low tensions, with a transition around  $\gamma_b$  the sharpness of which is controlled by  $\beta$ . Bleb formation is

physically very similar, although for different energy and length scales, to the invagination of protein-enriched membrane domains such as caveolae (155), which have been shown to buffer membrane tension. The total area in blebs is the bleb fraction times the maximal area that can be contained in blebs:  $A_b = A_{b0}n_b$ .

### ***Model predictions***

Solving Eq. [1] in the absence of blebs can be done analytically, and examples of such spreading curves are presented in Figure 3.4D. Initial spreading is linear with time with a rate  $\varepsilon / \eta_c$  (of order  $0.5 \mu\text{m}^2/\text{s}$ ), and the subsequent spreading kinetics depends on the recycling time  $\tau_m$ . If membrane recycling is fast:  $\tau_m \ll \tau_c$  with  $\tau_c = k_2 / \eta_c$ , the cell behaves as a soft body of stiffness  $k_2$  and spreading saturates after a time  $\tau_c$  to an area  $\varepsilon / k_2$ . In the absence of recycling, on the other hand, the spreading saturates to a much smaller area  $\varepsilon / (k_1 + k_2)$ . In the physiologically relevant limit  $\tau_m > \tau_c$ , the initial spreading kinetics is controlled by viscous dissipation in the cytosol, but the later stage is slower and controlled by the kinetics of area transfer.

At saturation, a large fraction of internal area has been transferred to the PM. Upon rapid cell detachment, most of the cell's adhered area retracts very quickly (see Figure 3.4.1). The excess area gained upon spreading results in a large drop of membrane tension (see Appendix D for details). If the tension drops below  $\gamma_b$  (Eq. [2]), blebs form on the cell surface, and take up part of the excess area, thereby buffering the tension to a value close to  $\gamma_b$ . After a time of order  $\tau_m$ , endocytosis slowly recycles the PM excess area, also removing bleb membrane area, until the rest tension is reached. The number of blebs on the PM decays in time with a characteristic time scale  $\tau_m$ . We present the numerical solution of Eqs.[1,2] for the decay of the number of blebs on the

PM with time in Figure 3.4.5, where parameters have been chosen to reproduce our experimental observation (Figure 3.4.3). The number of blebs remains constant for some time before decreasing because the cell was initially saturated with blebs ( $n_b \cong 1$ ). This can be expected in the case of strong adhesion, where the large membrane area transferred to the PM during spreading causes a massive drop of tension upon detachment.

We calculated the adhesion kinetics after different incubation times by choosing as initial conditions different points along the relaxation curve  $n_b(t)$  (squares, Figure 3.5A). The observed adhesion kinetics (Figure 3.3) could be reproduced by assuming that the presence of blebs reduces the energy of adhesion between the cell and the substrate, which we render using the effective adhesion energy  $\tilde{\varepsilon} = (1 - n_b / n_b^*)\varepsilon$  (Figure 3.5B). We find that blebs prevented adhesion ( $\tilde{\varepsilon} \leq 0$ ) when blebs covered more than  $n_b^* = 25\%$  of the PM surface. This effect can be traced to the fact that the blebs don't seem to promote strong substrate adhesion, and to the repulsive pressure exerted by inflating blebs colliding with the substrate. Finally, we remark that the maximal area at saturation ( $\sim \varepsilon / k_2$ ) is independent of whether the cells were initially blebbing or not.

Our model predicts saturation of spreading when the adhesion energy is balanced by membrane tension, corresponding to a well defined spreading area. It has been recently reported (150) that the force needed to extract a membrane tether from a spreading cell (which is related to the PM tension) does not increase, but rather decreases during spreading. The authors concluded (as we do here), that tension is regulated via membrane recycling. However, their observation is inconsistent with our assumption that membrane tension is responsible for the saturation of cell spreading. Tether force is not

only influenced by membrane tension, but also by membrane cytoskeleton interaction, and alteration of the latter could be responsible for the observations of (150). However, if membrane tension indeed decreases during spreading, another global cellular phenomenon must limit spreading. This detail could invalidate our prediction concerning saturation (although our main prediction, that the saturated area doesn't depend upon blebbing, is validated by our observations), but wouldn't change our picture of *i)* the way blebbing is related to membrane homeostasis, and *ii)* the effects blebs have on the initial cell spreading pattern.

### ***3.4 Conclusions***

It has been known for some time that, along with cytoskeleton remodeling, major cellular shape changes such as those occurring during mitosis, apoptosis and cell motility are regulated by membrane recycling. In addition to bringing specific proteins to the PM, membrane recycling also permits membrane area homeostasis, which insures that the right amount of membrane area is available for a particular transformation (156). In the absence of such regulation, large deformation would be prevented by excessive membrane tension. Membrane recycling is typically fairly slow (~30 min (152)), and the cell has other means to respond to sudden changes of PM tension, *e.g.* through the folding and unfolding of specialized membrane invaginations such as caveolae (155). Here we propose that cellular blebs can transiently play a similar role.

Membrane spreading and detachment are examples of shape changes involving major cellular reorganization, and have been of continued interest in relation to tumor growth and metastasis (149, 157). Both cell spreading (150) and detachment (148, 149) are accompanied by extensive membrane transport. As we show here, cell detachment

provides a remarkable illustration of membrane area homeostasis through the study of the cell blebbing activity. Following cell detachment using trypsin, cells round up in a similar manner to that characteristic of eukaryotic cells during mitosis (138). Trademark features of rounded or completely detached cells includes excess membrane, which arises from the rapid transition from a fully spread cell to a spheroid, and extensive membrane blebbing (138). We argue that blebs are nucleated by a sudden drop of tension following cell detachment, and provide the cell with a mean to store excess membrane (136). Although trypsin cleaves cell surface receptors during the detachment process, it has been previously illustrated that this does not significantly affect the readhesion or spreading saturation of cells (158). In fact, when DNA, RNA and protein synthesis are inhibited through via chemical treatment, there remains no effect on the ability of cells to readhere and spread following trypsinization (158). Studies which illustrate effects on readhesion following trypsinization report significant effects only when temperature is dramatically reduced compared to physiological norms (158, 159), emphasizing that the lag phase we observe following cells rapidly detached with trypsin is not a result of cells lacking necessary adhesion mechanisms. To further confirm this, detachment experiments were repeated using EDTA without trypsin. Following rapid cell detachment with EDTA, we observed numerous cellular blebs and reduced blebbing in cells that detach more slowly, consistent with our trypsin observations. Upon replating of EDTA-detached cells, we observed similar incubation-dependent dynamics comparable to those shown in Figure 3.3A for cells detached with trypsin (data not shown). This supports our model and emphasizes the large role of membrane tension regulation and recycling during the initial stages of cell spreading following rapid detachment.

Blebs could readily be monitored during cell spreading and detachment using BF and IRM imaging (Figure 3.1) and (Figure 3.3A). Upon sudden detachment by trypsin, cytoskeleton reorganization led to significant cell rounding after 10 min (Figure 3.1 and (134, 136)). This timescale is slow compared to the time needed to transfer significant membrane area between the PM and inner organelles, resulting in an important excess PM area and a large drop of membrane tension. In agreement with the prediction of our model, blebs spontaneously nucleated at low tension and exhibited the pattern of inflation and retraction previously described (108, 142, 143). The blebbing activity then steadily decreased with time and was entirely suppressed after about an hour (Figure 3.2), a time consistent with the kinetics of membrane recycling. Furthermore, when treated with dynasore, a drug inhibiting endocytosis, detached cells kept blebbing for as long as we watched them, indicating a clear connection between blebbing and membrane homeostasis. Our model could reproduce the slow disappearance of blebs by assuming a linear relationship between the flux of membrane and the difference of tension between the PM and internal organelles (156), extracting a typical membrane recycling time  $\tau_m=7$  min (Fig.3.2). Remarkably, slowing cell detachment using a smaller concentration of trypsin did not lead to blebbing. This illustrates a property shared by all viscoelastic bodies, that is, the strength of the response depends on the rate of the perturbation compared to the rate of internal relaxation. If cell detachment occurs sufficiently slowly for membrane homeostasis to regulate PM area, the PM tension is kept constant and blebs do not form.

Since blebs are so intimately related to cell detachment, it is interesting to understand how blebbing cells can re-adhere on a substrate. We replated detached cells

after letting them incubate for various times, and showed that blebbing versus non-blebbing cells have different initial spreading behavior and adhesion patterns (Figure 3.2). While non-blebbing cells formed filopodia and lamella right away and spread quickly as previously described (1), blebbing cells exhibited a lag phase during which blebs were seen to collide with and retract from the substrate, with little expansion of the adhered area. We showed (Figure 3.5) that this observation could be explained if blebs act as a pressurized cushion preventing cytoskeleton mediated adhesion to the substrate. Indeed, the termination of the lag phase and the initiation of the fast spreading regime coincided with the disappearance of blebs. Cells replated immediately upon detachment showed a long lag phase consistent with the bleb decay time of cells in suspension (Figure 3.2 and 3.3B), and the duration of the lag phase decreased with increasing incubation time. Interestingly, both blebbing and non-blebbing cells spread at a similar pace during their fast spreading regime, and reached similar spreading areas at saturation. Therefore, although blebs can serve as a reservoir of area (108, 136), blebs inhibit initial cell spreading because of direct interaction with the substrate but do not influence the final state. To emphasize that the bleb related dynamics we observe in Figures. 3.2 and 3.3 are not dependent on the substrate coating, we plated blebbing cells onto polylysine-coated glass bottom dishes and observe no statistical differences between spreading during the first 4 hours compared to fibronectin-coated dishes (data not shown).

In conclusion, this work illustrates that blebs are more than just an interesting cellular protrusion or a marker of cell apoptosis. Rather, cellular blebs are complex dynamic structures that prevent initial cell spreading and play a critical role in the global mechanical homeostasis of the cell through regulation of membrane tension.

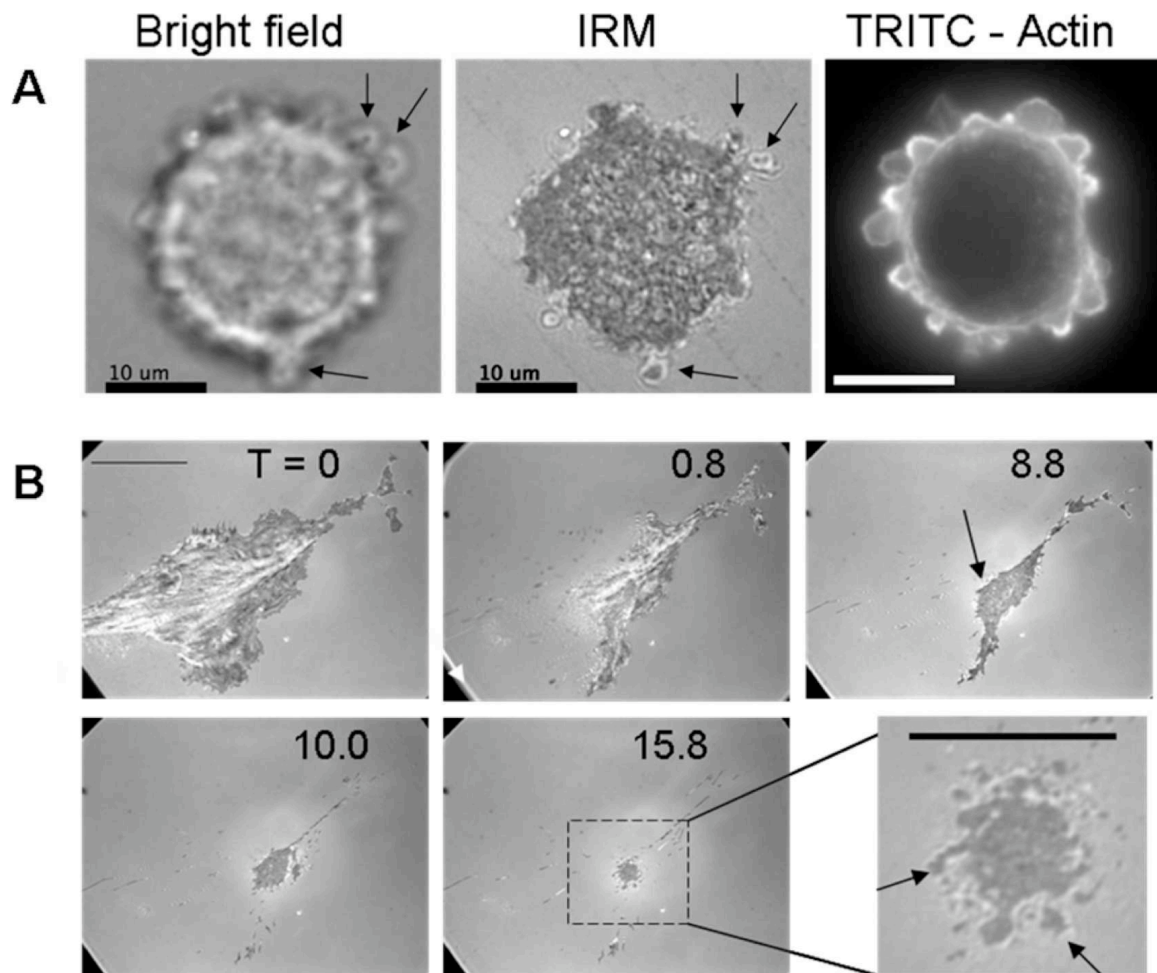


**Figure 3.1** (A) Identification of cellular blebs during detachment and spreading using interference reflection microscopy (IRM). Bovine aortic endothelial cells (BAEC) were observed using bright field (BF) and phalloidin-TRITC staining, and showed characteristic adhesion patterns when using IRM (arrows). IRM and BF images were captured within 10 sec for the same cell, while actin staining was performed on fixed cells. Scale bar is 10 $\mu$ m. (B). Using IRM, blebs were observed on the basal surface during trypsin detachment (T = min after addition of trypsin). Blebbing was first noted on only a small area of the cell at T=8.8 (arrow), and became more numerous and larger after 10 min (Scale bar is 25 $\mu$ m). T=15.8 is enlarged (scale bar is 10 $\mu$ m) to illustrate some of the blebs (arrows).

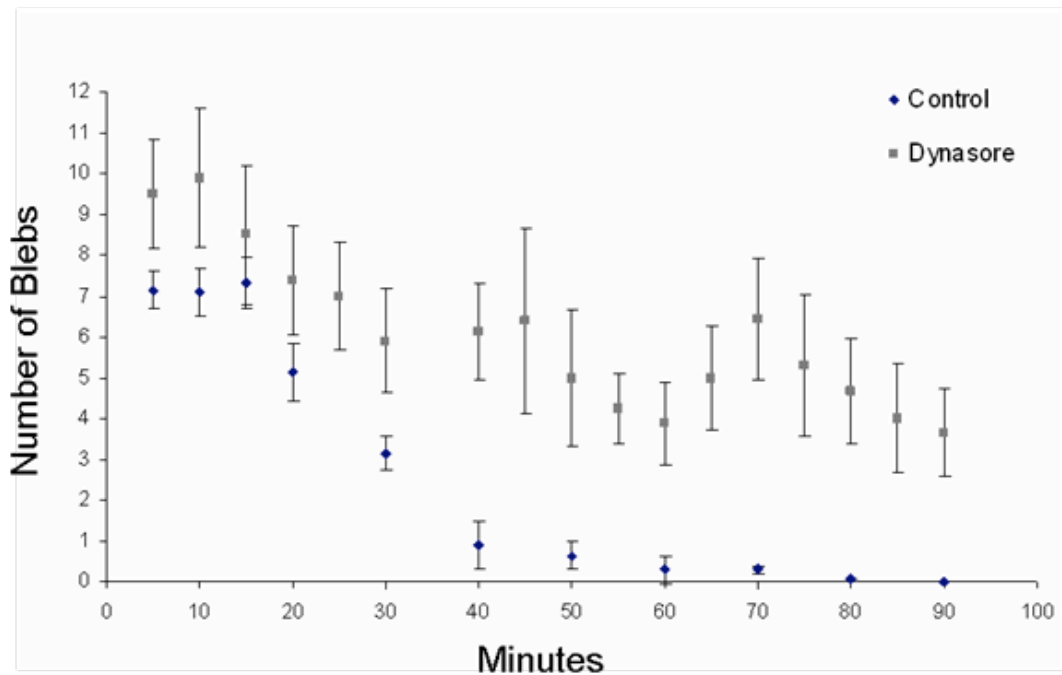


**Figure 3.2** The number of blebs per cell decreased with time spent in suspension. BAEC were plated onto extremely soft, uncoated polyacrylamide gels which prevented cell attachment and spreading. Cells were observed with multiple BF snapshots taken at each time point to ensure the identification of blebs on both the basal and apical surfaces. The normalized number of blebs per cell (compared to the number of blebs 5 min after detachment) is plotted with error bars representing standard error. Control cells (N = 10-20) maintained a constant number of blebs for the first 15 min, and then exhibited a continuous decrease in blebbing over time, with all blebs disappearing after 90 min. For dynasore treated cells (N=10), there is a slight decrease in blebbing over time, however only 1 of the 10 observed cells ceased blebbing after 90 min

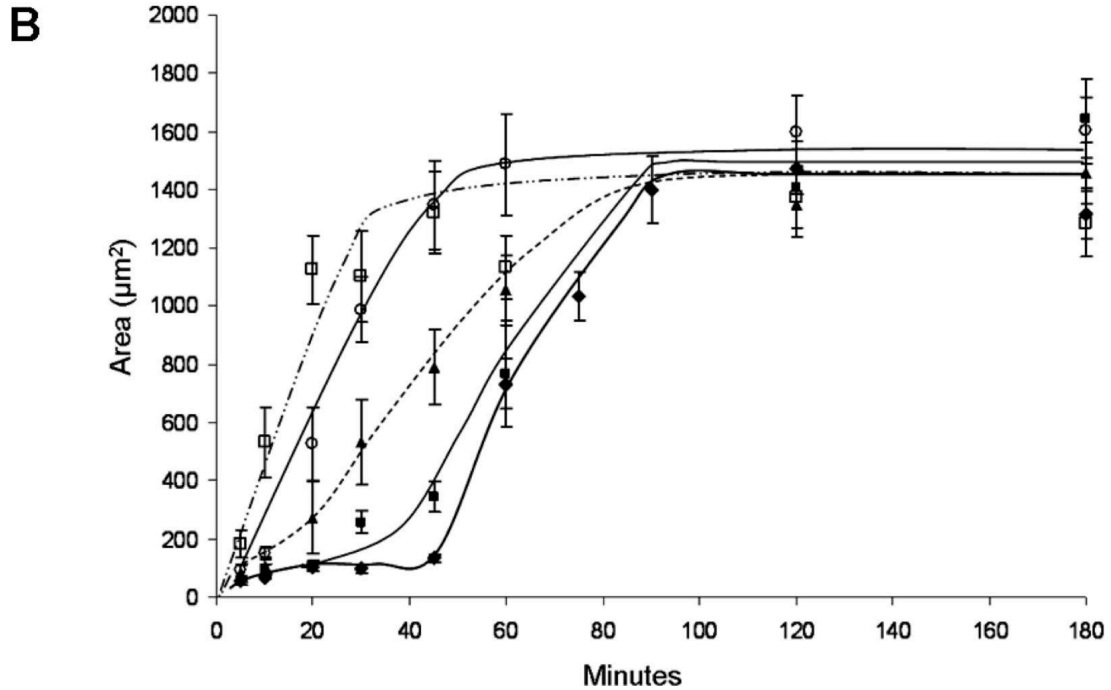
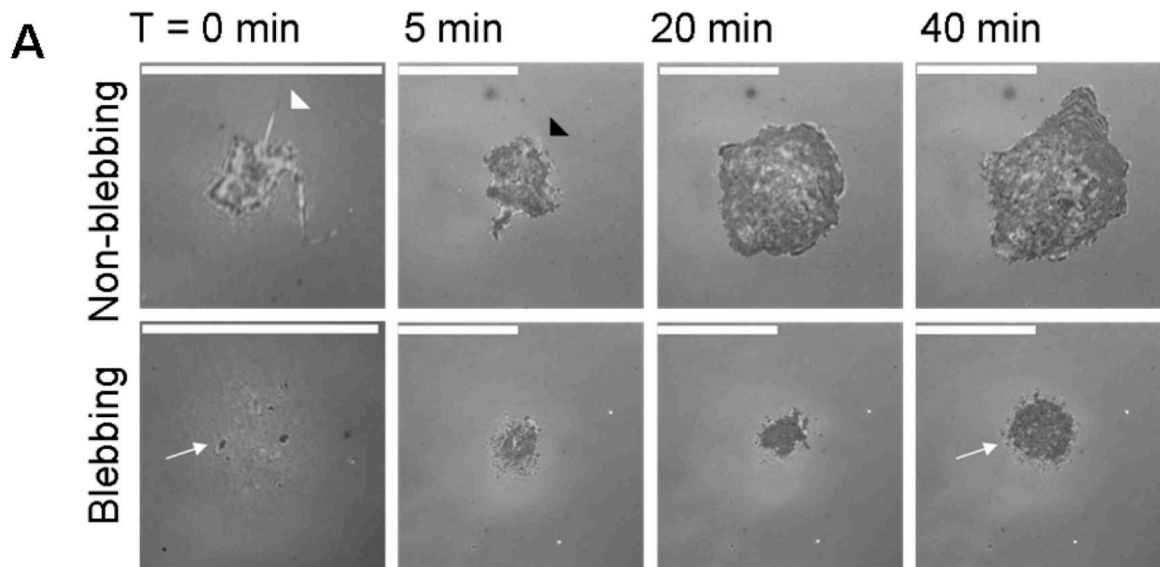


**Figure 3.3** (A) Differences in initial spreading behavior were observed for individual blebbing and non-blebbing cell spreading events. For non-blebbing cells, features of fast growth including filopodia (white arrow head) and lamella (black arrow heads) were present within the first 10 min of spreading. Blebbing cells attached initially to the substrate through individual bleb adhesions (white arrow, T=0 min) and continued to bleb for up to 40 min. After 40 min, fast cell spreading occurred with a similar speed to that of non-blebbing cells. (Scale bar is 25  $\mu\text{m}$ .) (B) Effect of time for which cells were suspended in solution prior to plating on cell spreading behavior. Suspension time = 0 (black diamond), 15 (black square), 30 (black triangle), 60 (white circle), or 120 (white square) min prior to plating. BF and IRM for a minimum of 15 random cells were captured for each time point. Error bars display standard error, with lines serving as guides to the eye.

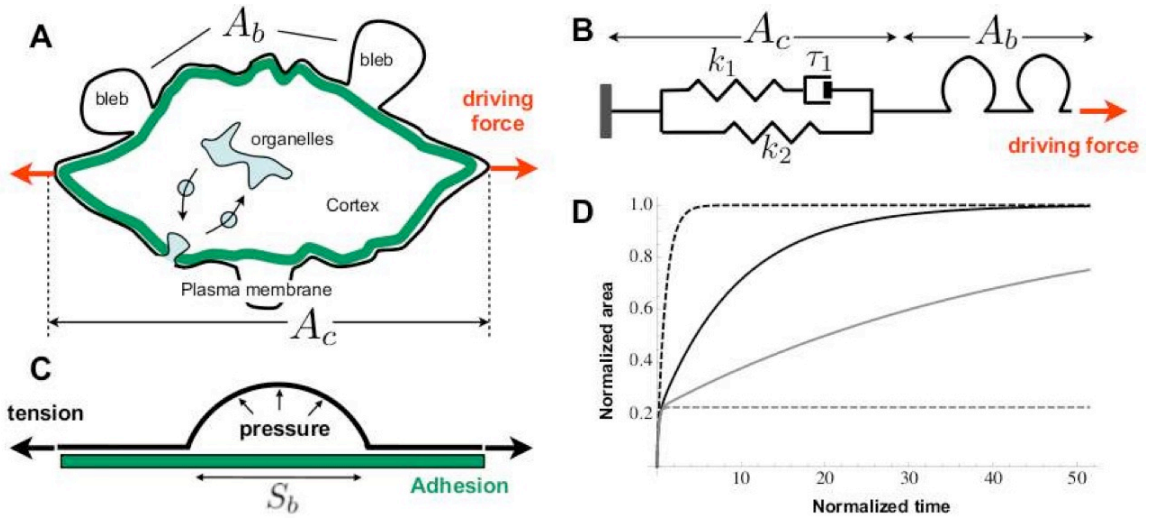


**Figure 3.4** Viscoelastic model for cell spreading (see Appendix D for more details). (A) Sketch of the cellular model: upon a perturbation that modifies the shape of the cell ( $A_c$ ), membrane recycling (time scale  $\tau_m$ ) and blebbing (bleb area  $A_b$ ) regulate membrane tension and cell deformation. (B) Equivalent visco-elastic model for the cell elasticity; spring and dashpot are linear elastic and viscous components, respectively. (C) Physical parameters influencing bleb nucleation (see text). (D) Kinetics of cell spreading under a constant driving force (the time is normalized by the typical spreading time  $\tau_c = \eta_c / k_2$ ). Dashed grey and black curves are purely elastic cells with very fast and very slow area transfer ( $\tau_c \rightarrow 0$  and  $\tau_m \rightarrow \infty$ , respectively). Solid grey and black curves are with membrane area transfer  $\tau_m = 10\tau_c$  and  $\tau_m = 2\tau_c$ , respectively, with  $k_1 = 3.4k_2$ .

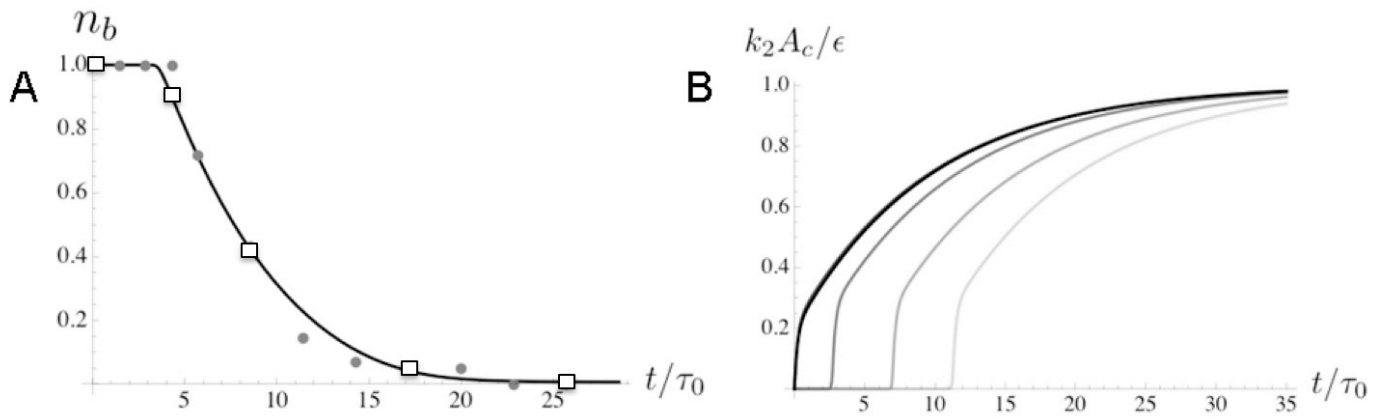


**Figure 3.5** (A) Evolution of the (normalized) average number of blebs per cell  $n_b$  with time. Cells were allowed to spread until complete saturation before their adhered area  $A_c$  was set to zero, keeping the initial PM area to its full spread value, leading to pronounced cell blebbing, quantified by Eq. [1]. Parameters are the same as in Fig.3.4, with  $\tau_m = 2\tau_c$ ,  $\gamma_b = -0.1\epsilon$ ,  $\beta\epsilon = 50$ , and  $A_{b0} = \epsilon/(4k_2)$ , and the grey dots show the experimental points of Fig.3.2. (B) Spreading kinetics for different incubation times (squares in (A)), increasing from zero (lighter grey) to infinity (black), with  $n_b^* = 0.25$ .

## **4 Effect of cytoskeletal disruption and membrane modification on endothelial cell spreading and blebbing<sup>†</sup>**

### ***4.1 Introduction***

Actin-based protrusions such as filopodia and lamellipodia have long been accepted as key constituents in processes such as cell motility, migration and spreading. Cellular blebbing has only recently been proposed as an additionally critical phenomenon contributing to these processes. Blebs have been observed in a wide variety of cell lines including fibroblasts (137), endothelial cells (24), zebrafish primordial germ cells (139), human melanoma cells (135, 143, 144, 160) and mesenchymal stem cells (unpublished data). The mechanics of cellular blebs have recently been well described (142, 143, 160, 161) based on biophysical examinations of bleb expansion and retraction.

Briefly, blebs putatively arise in areas of weak membrane-cytoskeleton attachment; however, blebbing also requires the local contraction driven by myosin II (134, 135, 140, 143, 160, 162). The myosin driven contraction of the cortex creates a compression of the cytoskeletal network, resulting in intracellular hydrostatic pressure, leading to local bleb expansion (134, 135, 143, 144). Retraction occurs upon accumulation of actin and other proteins inside the bleb. Trans-membrane actin-binding proteins first localize within the membrane of the bleb, followed by polymerization of actin at the membrane of the bleb and, lastly, localization of motor proteins, in particular, myosin II (160). A new membrane cortex is developed which is capable of reintegrating with the bulk cell cortex upon complete bleb retraction (142, 143, 160). Bleb expansion

---

<sup>†</sup> This section been submitted for publication as: Norman, LL, Sengupta, K, and Aranda-Espinoza, H. Blebbing dynamics during endothelial cell spreading. (Under Review, April 2010).

occurs quickly, within 30 seconds, while retraction occurs more slowly, lasting up to 2 minutes (135, 142).

Due to its mechanical origin, cell blebbing can be manipulated by varying osmotic conditions or by using chemical treatments that affect cytoskeletal components. For example, blebbing has been observed following microtubule disassembly (1, 163, 164), as well as inhibition of actin polymerization at short times (160). Inhibition of blebs is possible by increasing the membrane rigidity or inactivating myosin motors. Myosin inhibitors block the generation of contractile forces and weaken interactions between myosin and F-actin, therefore preventing bleb formation (143, 165). Blebs can be made smaller or larger by increasing or decreasing the extracellular osmotic pressure, respectively. These manipulations are based on the pressure changes that drive bleb formation and the cytoskeletal tension that balances outward pressure (143, 144). Blebs can also increase in size locally with the actin-depolymerization drug latrunculin A (latA) (143). The ability to modify cellular blebbing through chemical treatments has been extremely beneficial in understanding protein localization and bleb-membrane assembly (143, 160).

In the past, cellular blebs were most frequently associated with apoptosis (137, 166), however, as previously mentioned, non-apoptotic blebs have recently been observed in critical cellular processes including mitosis (135, 137, 138), spreading (133-136) and migration (139, 140, 162, 167, 168). In particular, cellular blebs have been identified as familiar features following cell detachment with trypsin (134). Note that, while cell surface receptors are cleaved during detachment with trypsin, readhesion and cell spreading are not significantly affected under physiological conditions (158, 159).

The most intense blebbing occurs within the first few minutes of plating, with blebs appearing on the cell periphery at later times (133). Some suggest that blebs are related to the degree of spreading (136) and may broaden the adhesion area of the cell to the substrate (134). Others suggest that blebs increase the cell surface area through excess membrane storage (136, 160). Little attention, however, has been given to the role of the attachment and retraction of blebs in cell-substrate interactions and spreading dynamics. Here, we observe the effects of chemical and osmotic disruptions on cell spreading and blebbing and identify increased spreading areas for cells with reduced blebbing. By quantifying individual bleb-substrate adhesions, we identified similar dynamics for both control blebs and nocodazole-induced blebs and identified three characteristic adhesion behaviors for all blebbing cells: 1) permanent adhesion, 2) adhesion followed by partial detachment, and 3) adhesion followed by total retraction. We propose that these bleb dynamics are related to the location of cellular blebs and physical forces present during spreading. Collectively, this work presents a new picture of cell-substrate interactions during the initial spreading process.

## ***4.2 Materials and methods***

### **4.2.1 Cell culture and substrate preparation**

Bovine aortic endothelial cells (BAECs) (Lonza, Walkersville, MD) were cultured as previously described above in section 3.2.1. Cells were starved of serum for approximately 16 hours and detached with 0.25% trypsin with EDTA (Invitrogen) prior to each experiment. Glass bottom dishes (No. 1.5) from MatTek Co. (Ashland, MA)

were coated with fibronectin by incubating in 100  $\mu\text{g}/\text{ml}$  fibronectin (Sigma-Aldrich) at room temperature for 2 hours. Dishes were rinsed three times with 1X PBS before use.

#### **4.2.2 Drug treatments and osmotic manipulation**

All drugs purchased from Sigma-Aldrich were chosen based on their ability to affect cytoskeletal components and thus allow for controlled manipulation of cellular blebbing. Nocodazole was used at 1  $\mu\text{M}$  to disrupt microtubules, myosin II was inhibited using 100  $\mu\text{M}$  blebbistatin, and actin filaments were disrupted using 1  $\mu\text{M}$  latrunculin A (latA). After detachment, cells were immediately counted and treated with the appropriate drug. Cells were incubated for 5 (nocodazole and blebbistatin) or 10 (latA) minutes prior to experiments. Control cells were maintained in BAEC media solution for 10 minutes prior to plating.

In experiments on osmotic differences, the osmolarity was increased using 150 mM sucrose. Standard BAEC medium was measured at 310 mOsM, and the osmolarity increased to 469 mOsM when 150 mM sucrose was added. In complementary experiments, osmolarity was decreased by diluting standard medium with ultrapure autoclaved water (1:1). When medium was diluted, osmolarity decreased to 150 mOsM. Cells were incubated in the appropriate solution for 5 minutes prior to the spreading experiments.

#### **4.2.3 Microscopy and imaging conditions**

IRM and TIRF microscopy were used cell-substrate behavior during spreading. Specific microscopy set-up is described in Appendix B. For TIRF imaging, BAECs were

transfected with both GFP-actin and mCherry-paxillin using lipofectamine (Invitrogen) and incubated in their respective chemical treatments as described above in section 4.2.2.

#### **4.2.4 Cell spreading experiments**

After incubation and/or chemical treatment, cells were immediately plated onto fibronectin-coated dishes filled with 2 ml of BAEC medium. For all drug and osmotic treatments, the same concentration was maintained for incubation and spreading. An average of  $5 \times 10^3$  cells were plated per dish to ensure that single cells could spread without touching others. For detailed view of the spreading dynamics, frames were captured approximately every 5 seconds during the first hour of spreading for single cells. To evaluate the statistics of spreading at specific time points, approximately 20-30 cells were randomly chosen and a single snap-shot of each cell was recorded. Experiments were repeated, with a final count of approximately 50-75 cells observed at each time point.

#### **4.2.5 Data Analysis**

The boundary of the cell was identified using an algorithm based on fitting of intensity histograms which was implemented in IGOR-Pro data analysis software (WaveMatrix, Portland, OR). For a detailed explanation of this method and the algorithms used to fit intensity histograms refer to Appendix C and Sengupta *et al* (2). For the analysis of the blebs, binary images were obtained using the cell-identification software. They were first cleaned by a process of dilation followed by erosion which fills up holes and removes small irrelevant specks from the binary images. Next, the in-built particle identification routine of IGOR-Pro was used to identify the position of each bleb

in each frame and the information about their position and size were stored. For bleb adhesion areas, individual blebs were followed and area was calculated from the binary images based on the coordinate position of each bleb over time.

For statistical evaluations of spreading areas, multiple cells were captured with single snap-shot images, and analyzed using ImageJ (National Institutes of Health, Bethesda, MD) software. The cell-boundaries were traced by hand and area was calculated using in-built ImageJ routines.

### ***4.3 Results***

#### **4.3.1 Cytoskeletal disruptions and membrane tension affect global statistics of spreading and blebbing**

BAECs were subjected to multiple chemical and osmotic treatments in order to test the effects of disrupting specific cytoskeletal components and to modify the plasma membrane tension. Specific chemical treatments included blebbistatin (100  $\mu\text{M}$ ) used to inhibit myosin II (143, 165), nocodazole (1  $\mu\text{M}$ ) used to disrupt microtubules (1, 163, 164), and latA (1  $\mu\text{M}$ ), which was used to disrupt actin filaments (143). Modifications of the plasma membrane tension were achieved by increased or decreasing the osmolarity of the media through the addition of 150 mM sucrose or a 50% media dilution, respectively. Sucrose was used to increase the physical forces opposing blebbing (143), while the media dilution was used to generate a decreased pressure environment. The use of sucrose to affect bleb and membrane dynamics was based on the pressure changes that drive bleb formation and the cytoskeletal tension that balances outward pressure (143, 144). Cells were incubated in the appropriate solution for 5 or 10 minutes prior to the

spreading experiments (see Materials and Methods), and remained in the presence of the drug (or osmolarity modification) during the entire four hours of observations, preventing cells from fully recovering following chemical treatment or pressure modifications. Cells were initially identified using BF microscopy to ensure all observations were performed on individual cells, which did not contact neighboring cells. The microscope was then switched to IRM mode and snapshots were taken using IRM in order to quantify cell spreading. After multiple experiments, approximately 50-75 cells were observed for each condition with the average normalized adhered areas (normalized to saturated control cells at 4 hours of spreading) plotted in Figure 4.1. A summary of observations from the first four hours of spreading, including the presence of blebs and the effect of treatment on total spreading area are compiled in Table 4.1.

All treatments except blebbistatin resulted in significantly less spread cells compared to control after the first hour of spreading. Representative IRM snapshots after one hour of spreading are shown in Figure 4.2, with remarkable differences appearing in the total spreading area of individual cells. Most significant are nocodazole and latA treated cells, illustrating the critical importance of both microtubules and actin dynamics in the initial stages of cell spreading. Control BAECs did not reach saturation within the first hour, illustrated by the significant difference between the 1 and 4 hour spreading areas. Similar to control cells, all treated cells were significantly more spread after 4 hours, illustrating that control and treated cells continued to spread between the 1 and 4 hour time points. After four hours of spreading, cells which spread in the presence of media dilution were no longer significantly different from control. All other treatments remain less spread after four hours ( $p < 0.05$ ), compared to control cells. This suggests

that decreased osmolarity only hinders the spreading process and does not prevent cells from reaching a fully saturated spreading state.

After 1 hour, blebs were still present in a large percentage of cells treated with nocodazole and latA, and are clearly observed using IRM (Figure 4.2). Interestingly, for all treatments, the percentage of spreading cells blebbing after 1 hour is inversely related to the degree of spreading. For nocodazole and latA treated cells, which spread only slightly during the first hour, the observed percentage of cells which remained blebbing after 1 hour was 65% and 66%, respectively. For cells which spread to a larger area, such as those cells which spread in diluted media or sucrose solution, we observed only 9% or 15%, respectively. For both control and blebbistatin treated cells, there was no blebbing after 1 hour. In addition to the inhibition of critical elements involved in cell spreading (such as microtubules and actin), these observations suggest that cell spreading may also be inhibited by the inability of the cell to make proper contact with the substrate and reintegrate blebs with the plasma membrane. To further evaluate this concept, individual cells were observed during the first 45 minutes of spreading dynamics.

#### **4.3.2 Cytoskeletal disruptions inhibit initial spreading**

Of all observed treatments, the spreading behavior of nocodazole and latA treated cells appear to be the most affected. Individual spreading dynamics for nocodazole and latA treated cells were observed along with blebbistatin (non-blebbing) and control cells using IRM. These observations revealed distinct differences between chemically treated and control BAECs. Differences in the initial adhesion patterns and bleb appearances are shown in Figure 4.3. Control as well as nocodazole and latA treated cells possess blebs upon initial attachment (Figure 4.3, arrows). After 30 minutes, blebs have begun to

disappear and instead lamellae are present (Figure 4.3, arrowheads). Single cell spreading dynamics were observed during the first 45 minutes of spreading, with the total adhesion areas plotted in Figure 4.3 for representative cells. At first, control cells exhibit an initial slow spreading period prior to fast spreading. Lamella appeared on control cells around the start of fast growth (Figure 3B, arrow head) and was quickly followed by the cessation of cellular blebbing (Figure 3B, arrow). Since blebs disappear following the appearance of lamella, this suggests that the transition from slow to fast spreading is not driven by the elimination of blebs, but rather by the apparition of lamella. The average appearance of lamella occurred around  $20 \pm 3$  mins (N = 9 cells, S.E.M), while the average disappearance of blebs occurred at  $24 \pm 4$  mins (N = 9 cells, S.E.M). In all observed cases, the lamella appeared prior to the cessation of blebbing. The cessation of blebbing occurred approximately  $2.5 \pm 0.7$  mins following the first appearance of the lamella. Fast growth continued for the first hour of spreading and saturation was not typically reached until 90 minutes (data not shown).

#### ***Blebbistatin treatment***

Blebbistatin treated cells did not produce blebs due to myosin II inhibition (165, 169). Inhibiting myosin II results in the inability to contract the actin-membrane complex, a necessary step for bleb expansion and retraction. Interestingly, blebbistatin treated cells spend less time at a slow spreading rate compared to control cells, and the appearance of lamella occurs around  $7.5 \pm 3$  mins (N = 4 cells, S.E.M.), more than 12 minutes earlier than blebbing control cells (Figure 3B). It is likely that the lack of blebs present allowed the cell to begin fast growth prior to blebbing cells, which require a remodeling of the plasma membrane prior to fast growth. Similarly, it has been

illustrated that myosin II inhibition increases the rate of cell spreading in fibroblasts (170, 171); however, although we see that fast growth occurs more quickly during the spreading process, we did not see a significant difference in the adhesion areas between control and blebbistatin treated cells after 1 hour (Figure 4.1). In fact, we see that although myosin II inhibited cells initially spread similarly to control cells in area after 1 hour, the inhibition of MII prevents cells from reaching a fully saturated state comparable to control cells after 4 hours of spreading (Figure 4.1).

#### *Nocodazole treatment*

The microtubule-destabilizing agent nocodazole was used to disrupt microtubules during spreading. BAECs incubated in nocodazole exhibited numerous blebs which typically covered the entire cell membrane surface. Although it has been demonstrated that there are no microtubules within blebs (133), a vast amount of literature has looked at the effect of microtubule disruption on cell spreading. Some experiments show cells decrease in total spreading area after treatment (172, 173), while others show no change (1, 174) or varying degrees of change (175). Differences with incubation times, drug concentrations, and substrate adhesion are some factors that likely account for this variability. For our experimental parameters, microtubules appeared to play a vital role in the initial spreading of BAECs. Although nocodazole treated cells are unable to reach a saturation state comparable to control cells after 4 hours, the spreading area continues to increase between 1 to 4 hours of spreading. This could possibly be due to previously described structural redundancy mechanisms which suggest that cells contain compensatory mechanisms, such as microfilaments, for stabilizing cell shape when microtubules are compromised (175). This increase in spreading area is also apparent in

Figure 4.3B, where nocodazole treated cells exhibited both a slow (prior to the appearance of lamella, arrowhead) and fast (following the appearance of lamella and bleb cessation) spreading regime. However, there is a noticeable difference in the rate of the fast spreading regimes for nocodazole treated cells compared to control or blebbistatin treated cells. For the majority of individual cells (4 out of 6), lamella were not observed and blebs were present during the entire first hour of spreading. For the cells which stopped blebbing, lamella appeared on the surface prior to the cessation of blebs similarly to that described for control cells.

#### ***Latrunculin A treatment***

Latrunculin A binds to G-actin and disrupts the polymerization of actin filaments. BAECs treated with latA spread very little during the first hour (Figures 4.1-4.3) and possessed blebs that appeared incapable of retracting. In fact, blebs were still observed after 1 hour of spreading (Figure 4.2). Similar results were seen by Charras, *et al.* (143), where localized incubation with latrunculin B inhibited retraction locally, yet increased bleb size globally. After 1 and 4 hours, latA treated cells were significantly less spread than control cells. There was a certain degree of spreading, most likely due to membrane adhesion; however no lamellae were observed and in turn, cells did not exhibit fast spreading during the first hour. Comparable observations were seen in latA treated neutrophils, which undergo an initial substrate-attachment, including bleb adhesion, but fail to spread after activation (2). Other actin-interfering agents, such as cytochalasins B and D, exhibited less severe effects on spreading. Neutrophils incubated with cytochalasin B spread after activation and reached their saturation area quickly (2), and

similarly; it has been illustrated that cytochalasin D can also increase the spreading rate of HeLa cells (1).

### ***Osmotic treatment***

Cells treated with 150 mM sucrose were much smaller in size (Figures 4.1 and 4.2), with noticeable vacuoles and blebs. Osmotic effects on blebbing and spreading have recently been described using the Laplace equation (143, 144):  $T_m + T_c = 2r\Delta P$ , where  $T_m$  is the bleb membrane tension,  $T_c$  is the cortical cytoskeleton tension,  $\Delta P$  is the pressure difference between the inside ( $P_i$ ) and outside ( $P_o$ ) of the cell, and  $r$  is the bleb radius. From this equation, an increase in intracellular pressure increases bleb tension, while a decrease in intracellular pressure decreases bleb tension. Thus, we expect hypotonic solutions, which cause an increase in intracellular pressure, to produce cells with numerous large blebs, and we expect fewer and smaller blebs in hypertonic sucrose solutions, which decrease intracellular pressure and bleb tension. Dai and Sheetz (144) have illustrated with membrane tethering experiments that an increase in bleb size does correlate to an increase in tension. As expected, our results illustrate that sucrose treated cells are smaller in size and have fewer blebs, whereas dilution treatments produce cells with larger blebs and decreased spreading areas only during the first hour of spreading.

As briefly mentioned, for control, blebbistatin treated cells, which exhibit a fast spreading regime (and for those nocodazole cells which stop blebbing), we first observed the appearance of lamella at the start of fast growth. For control and nocodazole treated cells which possess blebs, the blebs disappeared from the basal surface after an additional few minutes (Figure 4.3B). Interestingly, although we did see the coexistence of blebs and lamella, the lamella appeared on an area of the cell where we no longer observe blebs

on the basal surface (Figure 4.4). This was observed for both nocodazole treated and control cells. Since we noticed a correlation between lamella apparition and the start of fast growth, and also observed an absence of blebs from regions of the cell which are spreading quickly, we suspect that cellular blebs may inhibit spreading by either altering typical cell-substrate adhesion dynamics and/or delaying the formation of lamella. This delayed lamella formation would be consistent with the observed decreased spreading areas for chemical treatments which support blebbing (i.e. nocodazole and latA). To evaluate these concepts experimentally, we observed the adhesion dynamics of individual blebs during the spreading process and also observed the differences in actin organization for control versus chemically modified cells during spreading.

### **4.3.3 Bleb adhesion dynamics during spreading**

Figure 4.5 illustrates the bleb identification technique developed with the use of the software described in Materials and Methods. The IRM image on the left shows the adhered blebs at T=0 minutes, while the image on the right identifies individual blebs whose number and area can be measured. Blebs were only counted if they were single blebs which did not touch other blebs or the central spreading cell area. Spreading dynamics are described by quantifying the time and area of each individual bleb-adhesion site for both control and treated cells.

LatA blebs were difficult to distinguish because they were only weakly adhered and did not exhibit regular extension/retraction dynamics. In IRM, less adhered areas appear as lighter shades of gray or white, and therefore the white “patchy” areas observed in Figure 4.4 for latA treated cells at 5 minutes reflect that the cell is only weakly adhered

to the surface. Most likely, the blebs and other parts of the cell membrane fluctuate close to the substrate and do not attach strongly to the substrate.

Comparison of nocodazole treated cells with control cells can be seen in Figure 4.6, where the bleb area is quantified and represented as red or black lines respectively. Dynamics of individual blebs reveals that blebs exhibit one of three types of behavior during spreading: 1) permanent adhesion, 2) adhesion followed by partial detachment, or 3) adhesion followed by total retraction. Permanent adhesion is observed in blebs which have a sharp increase in adhesion area, with no subsequent decrease (marked with an asterisk in Figure 4.6A). Partially retracting blebs exhibit a subsequent decrease in area (illustrated with a cross in Figure 4.6A), and lastly, certain blebs adhere to the surface and then completely retract (Figure 4.4B), with an average duration of adhesion (N=28 blebs) of 0.5 minutes. Overall dynamics is similar for control and nocodazole treated cells. Due to the temporal nature of bleb adhesion area, we use the average maximum area for comparisons. The average maximum area for attached control blebs was  $2.62 \pm 0.76 \mu\text{m}^2$  compared to  $1.51 \pm 1.48 \mu\text{m}^2$  (S.E.M) for nocodazole blebs. For retracting blebs, the average maximum adhesion area for control blebs was  $1.13 \pm 0.60 \mu\text{m}^2$  compared to  $0.70 \pm 0.17 \mu\text{m}^2$  (S.E.M) for nocodazole blebs.

For both control and nocodazole treatment, the initial cell-substrate contacts occurs through individual bleb adhesions which, after attachment, begin to coalesce to form a central cell spreading area. The permanently adhering blebs which appear during the very initial stages of spreading for control and nocodazole treatment represent these initial contacts. Although retracting blebs appear throughout the first 10 minutes, more retracting blebs occur between 4-10 minutes. Blebs that retract do not contribute to the

total spreading area, and as mentioned in the previous chapter, this retraction contributes to the lengthened slow-spreading behavior observed in Figure 4.3.

This experiment shows that blebs initially contribute to the start of spreading by serving as the primary adhesion sites upon initial attachment. However, as spreading proceeds, retracting blebs, which have still not reintegrated into the cell membrane, prevent the formation of lamella and subsequent fast growth. Interestingly, bleb dynamics does not seem to be affected by microtubule disruption.

#### **4.3.4 Physical forces inhibit bleb retraction**

As illustrated in Figure 4.6B, certain blebs adhere completely to the surface, while others appear to come in contact with the substrate and quickly retract from the surface. One explanation for the difference between adherent versus non-adherent blebs may be that certain blebs possess adhesive binding proteins, such as integrins, while other blebs lack these adhesive structures. Although this is an intriguing possibility, there is also the likelihood that physical constraints prevent the adhesive blebs from retracting. To determine whether physical forces inhibit bleb retraction and encourage certain blebs to adhere to the substrate, BAECs transfected with GFP-actin were observed during spreading using TIRF microscopy. Both adhering and non-adhering blebs were observed during the initial spreading process (Figure 4.7). Adhering blebs typically appeared in the more central region of the cell, while retracting blebs were most noticed on the periphery of the cell. Retracting blebs likely experience less physical restraints from the above cell body, and therefore more easily retract from the surface. In particular, this is observed at later time of spreading when the majority of retracting blebs are present on the periphery of the cell (see Figure 4.4). These “peripheral” blebs likely experience less

pressure because the cell has already begun to spread and a significant portion of the cell body is not longer directly above the structures.

Initially, adhering blebs came into contact with the substrate and increased in size as they began to attach to the surface (seen by increase in bleb area between  $T = 0.3$  and  $T = 1.0$  minutes in Figure 4.7). As time progressed, adhering blebs appeared to become trapped by surrounding blebs and the spreading cell (Figure 4.7) between  $T = 2.3 - 4.3$  minutes. When blebs became entrapped in this manner, retraction was not observed, suggesting that the bleb was physically prevented from retracting from the surface. An increase in the actin intensity was also observed for adhering blebs (Figure 4.7,  $T = 3.0$  minutes) illustrating actin recruitment to the membrane. In contrast, retracting blebs on the periphery of the cell were weaker in actin-intensity, likely because they quickly came into contact with the substrate and promptly retracted. The time frames for adhering and retracting blebs are comparable to those identified using our bleb-detection software (Figure 4.6). This data further illustrates that certain blebs are observed to be “adhering” because they are trapped by the surrounding cell and blebs and appear incapable of retracting, while other blebs that are localized further from the spreading cell are “retracting” and display weak cell-substrate interactions. Collectively, this data illustrates that physical parameters contribute to the different bleb behaviors observed, and not adhesive properties of the individual blebs.

#### **4.3.5 Paxillin localization appears after the cessation of blebs**

Since blebs are transient features observed during spreading, we hypothesized that developed focal adhesions would appear late in the spreading process, after which blebs have become fully reintegrated. To identify when focal adhesions form during cell

blebbing and spreading, BAECs were co-transfected with GFP-actin and mCherry-paxillin (a focal adhesion protein) and observed with TIRF microscopy for the first hour of spreading (Figure 4.8). At  $T = 15$  minutes, blebs were seen on the surface during the first hour of spreading for control, nocodazole and latA treated cells (Figure 4.8, arrow heads) and, as expected, were absent from the blebbistatin treated cells. During the first 15 minutes, the appearance of paxillin is very diffuse for all conditions, as illustrated by the grainy red expression in Figure 4.8. Diffuse expression of paxillin, similar to that seen in the rest of the cell body can be observed inside blebs, however, no distinct puncta are observed. This suggests that blebs which adhere are not adhesive because of increased paxillin expression. After 45 minutes of spreading, blebs were no longer observed and thin lamella was present around the periphery of the control cell. Although control and blebbistatin-treated cells are fairly well spread by 45 minutes, paxillin expression remains weak. This suggests that blebs likely do not affect the appearance of focal adhesion formation, since both control cells (which bleb) and blebbistatin-treated cells (which do not bleb) exhibit similar paxillin expression during the initial spreading process. By 1 hour of spreading, focal adhesions are observed by the appearance of distinct paxillin puncta formation for both control and blebbistatin-treated cells (Figure 4.8, arrowheads).

For nocodazole and latA treated cells, which do not spread significantly during the first hour of spreading, the appearance of paxillin puncta was not typically observed. In a few cases, some of the more spread nocodazole treated cells exhibited paxillin expression localized to the outer periphery of the spreading cell (Figure 4.8,  $T = 45$  minutes). Although not all cells exhibited this behavior, it is possible that the observed

paxillin “ring” is involved with increased cell adhesion, which has been reported by others (172), who show decreased spreading and increased ECM adhesion following microtubule disruption. As expected, both actin and paxillin organization appear much disrupted following latA treatment. Although there is a small amount of spreading, actin and paxillin were diffuse and lacked typical cytoskeletal organization.

Since the appearance of focal adhesion formation appears well after cellular blebbing has stopped, these results illustrate that the cellular blebbing does not contribute to focal adhesion formation. Further, focal adhesion formation occurs at a similar spreading time for both blebbing (control) and non-blebbing (blebbistatin-treated) cells, suggesting independence between the focal adhesion development and the cessation of blebbing. Lastly, these results emphasize that for control cells, lamella formation, fast spreading, and focal adhesion formation all occur after the integration of cellular blebs.

#### ***4.4 Conclusions***

Cellular blebbing is a familiar feature following trypsin-based cell detachment methods (134) and cell division (135, 137, 138), and has also been observed during cell spreading (133-136). Cell spreading is a critical phenomenon in several biological processes including embryonic development, cancer metastasis, and mitosis; however the role of blebs during this process is still poorly understood. In the present study, we show that modification of cellular blebbing through chemical and osmotic disruptions causes a decrease in the initial spreading of endothelial cells (Figure 4.1). Interestingly, we report an inverse correlation between the percentage of blebbing cells and the total spreading area after 1 hour. This led us to observe single cell spreading events, where we noticed significantly increased durations of slow spreading with blebbing cells (Figure 4.3B).

Initially, we suspected that if blebs were preventing the initiation of fast spreading, then blebs should disappear prior to lamella formation and the start of fast growth. The appearance of the lamella and the beginning of the fast spreading regime approximately coincides for all observed control cells; however, the disappearance of blebs did not always occur at the same time. For the short period of time when cellular blebs do coexist with lamella, they typically appear distant from one another (Figure 4.4), suggesting that bleb membrane needs to be reintegrated into the cell membrane prior to lamella development. To emphasize that the blebbing behavior and effects on spreading which we report here is not an effect of trypsinization, we repeated spreading experiments with cells detached using EDTA (without trypsin) and observe similar blebbing and spreading behavior (data not shown). In addition, we performed spreading experiments for cells plated onto polylysine-coated dishes and observe no significant differences in spreading area during the first four hours (data not shown), illustrating that this behavior is not a result of substrate coating.

Observations of individual bleb dynamics illustrate a dichotomy between contributing to and preventing cell spreading. First, we illustrate that the initial cell-attachments occur through individual cell blebs (Figures 4.5 and 4.6). However, as blebs begin to coalesce and the spreading area increases, the abundance of retracting blebs prevents the cell from entering the fast growth regime. If all blebs were adherent, we surmise that the rate of the lag time would decrease and lamella would likely appear more quickly, as there would be a substantial amount of cell-substrate adhesion available for a lamellipodium to form.

Surprisingly, nocodazole and control blebs appear to exhibit similar adhesion behaviors during the initial spreading process, although blebs remain longer on nocodazole treated cells. RhoA pathways have been shown to regulate blebbing (160), while separately microtubule depolymerization can promote local RhoA activation (176). The proposed actomyosin contraction caused by activated RhoA (177) would likely contribute to the accepted model of blebbing proposed by Charras, *et al.*(143), which involves an initial contraction of the actin cortex. Therefore, it is not entirely surprising that the bleb dynamics does not change with microtubule disruption but is strongly influenced by actin distribution. In addition to these signaling pathways, we suspect that the lengthened blebbing regime in nocodazole treated cells arises because microtubules are tension bearers and eliminating them makes it easier for actomyosin to “squeeze” the cell cytoplasm resulting in an increased in internal membrane pressure. This tension would become regulated as the cell spreads, allowing for blebs to reintegrate, albeit over longer periods of time. This increase in the duration of blebbing also correlates with a decreased spreading area observed at both 1 and 4 hours (Figures 4.1, 4.3, and 4.8), an observation reported by others (172, 173). Increased cell adhesion reported to occur with microtubule disruption (172) and subsequent decreases in spreading that we (and others) observe may be partially explained by the relationship between microtubule disruption and Rho activation, and the subsequent enlargement of focal adhesions (178, 179). This relationship may also help to explain the paxillin “ring” observed in nocodazole treated cells (Figure 4.8). In addition to slower substrate contact turnover (173) and increased adhesion (172), here we also consider that a decrease in the spreading rate may be due to the large number of blebs in nocodazole treated cells and their collective inhibitory

behavior during the initial stages of spreading. Although the nocodazole treated cells did not spread to the same area as control cells, they did continue to increase in spreading area, likely as more cellular blebs were reintegrated in the cell membrane and attached to the substrate. After 1 hour of spreading, the number of nocodazole treated cells (N=50) still blebbing was 65%, while after 4 hours this percentage dropped to 38% (N=50). Since nocodazole cells are still spreading between 1-4 hours, but with much slower rates, this supports the hypothesis that blebs hinder the cells from reaching the fast spreading regime.

Unlike nocodazole treated cells, BAECs treated with blebbistatin did not produce blebs. Based on the literature, in which an increase in the rate of cell spreading in fibroblasts has been reported (170, 171), we were surprised to observe no significant difference in spreading after 1 hour and significantly less spread cells after 4 hours compared to control cells (Figure 4.1). We did observe a few cells which possessed blebs; however, these blebs were not dynamic, suggesting that they had formed prior to the blebbistatin incubation. It is possible that these few blebs which were present may have slightly slowed the spreading behavior of the cells. In addition, varying results in the literature have been reported on blebbistatins' effects on eukaryotic cell migration, with observations illustrating a species-dependent spreading effect. Blebbistatin does not affect migration of *Drosophila melanogaster* cells [30], yet disrupts migration in *Xenopus* tissue [30] and pancreatic adenocarcinoma cells [31]. As well as cell type, incubation times and drug concentration may also account for this variability. In our study, blebbistatin treated cells continue to spread between 1 and 4 hours of spreading but are unable to spread as well as control cells. This suggests that although blebbistatin

treated cells can initially spread quickly (in part because of their lack of blebs), MII inhibition is also indirectly preventing maximal spreading through other mechanisms, such as a possible reduction in the rate of lamellipodial extension, or an imbalance in extension and retraction dynamics.

A primary conclusion from this study is that initial blebs allow the cell to attach to the substrate and initiate the spreading process. Since cell blebs typically adhere with a very small area, it is easy to overlook these initial attachments during typical spreading experiments. Without the use of high magnification surface sensitive microscopic methods such as IRM and TIRF, it is unlikely that one can properly evaluate the bleb-substrate interactions. In fact, the initial spreading dynamics is often overlooked when the lag time for spreading initiation is subtracted from the growth rate, as described by others (1). Our work suggests that these initial adhesions are critical components in the spreading process and have the potential to modify typical spreading behavior. Although blebs do initiate the first cell-substrate contact sites, the cell does not spread quickly upon bleb-substrate attachment. Here we show that individual blebs actually possess three types of behavior: 1) permanent adhesion, 2) adhesion followed by partial detachment, and 3) adhesion followed by total retraction. Blebs which contribute to the total spreading area include those which permanently adhere and those which adhere and then partially detach. Blebs which simply touch the surface and completely retract do not contribute to the total spreading area. We infer that these blebs actually prevent the cell from entering a state of fast growth because it is necessary to reintegrate these blebs in order to create available membrane close to the surface, which is necessary for the development of lamellipodium and fast-spreading. Initially, it may appear that blebs

increase the adhesion area of the cell, as previously speculated (134). However, due to the numerous attachment/retraction dynamics (Figure 4.6) which we observe, this simple view does not seem to hold. We hypothesize that the difference between adhering versus retracting blebs is not due to differences in adhesive proteins, but rather the inability of adhering blebs to retract from the surface due to physical constraints (Figures 4.7 and 4.8). Further exploration of specific integrins and adhesion receptors would be beneficial in advancing the understanding of this phenomenon.

Although small bleb adhesions do contribute to the total spreading area, the most significant contributions to the attachment area are due to fast lamella spreading. The adhesion area due to blebs ( $A_0$ ), is related to the average adhesion area of individual blebs ( $\Delta A$ ) over time of adhesion ( $\Delta T$ ) for all individual blebs ( $N$ ), and can be written as:

$A_0 = \frac{N\Delta A}{\Delta T}$ . Here, during the initial adhesion process, the average total adhesion area contributed by individual adhering blebs,  $\Delta A = 1.65 \pm 0.7 \mu\text{m}^2$ , time of adhesion,  $\Delta T = 1.25$  min, and  $N \sim 3$  blebs per minute. This results in an approximate rate of spreading due to bleb adherence as  $\sim 4 \mu\text{m}^2/\text{min}$ . At 30 minutes of spreading, the cell would have spread  $120 \mu\text{m}^2$ , in agreement with Figure 4.3. Therefore, blebs of type 1 and 2 determine the rate of spreading initially, while the fast spreading rate of  $\sim 30 \mu\text{m}^2/\text{min}$  is determined by lamella.

The lamella extends during the end of the lag phase and the start of fast growth with an approximate speed of  $1.2 \mu\text{m}/\text{min}$ . At this growth rate, blebs that grow and retract within 2 minutes may be overcome by cell spreading. Possibly, lamella forms in an area of the cell which has already reintegrated the nearby blebs, and rate of lamella growth overcomes the remaining expanding blebs. Further identification of cytoskeletal

dynamics during lamella/bleb competition would be necessary to evaluate this possibility. Note, the speed of lamella extension we observe here is slightly less than that observed by others in fibroblasts, which ranges from 4-7  $\mu\text{m}/\text{min}$  (180, 181). However, here we measure the lamella extension during bleb/lamella coexistence, where the rate may be reduced due to membrane remodeling and actin organization during bleb reintegration, while data reported for fibroblasts is in reference to lamellipodial extension during migration.

In summary, cellular blebs are familiar features of the initial spreading process; however, until now little has been known about how cellular blebs affect spreading, in particular, the initial spreading dynamics. Here, we show that blebs initially create the first adhesion sites for the cell during spreading, and that their continuous protrusion and retraction events contribute to the increased slow spreading period prior to fast growth. The detailed effects of blebbing dynamics on spreading behavior that we demonstrate here present a new picture on blebs during initial cell spreading.

Treatment	Cytoskeletal and/or Membrane Effect	Effect on blebbing	% Blebbing after 1Hr	Effect on spreading
Control	N/A	Blebs appear following trypsin detachment	0%	N/A
Blebbistatin	Inhibits myosin II (165, 169) Decrease osmolarity and the forces which oppose blebbing (143, 144)	No blebs produced after addition of drug treatment.	0%	4Hrs
Media Dilution	Increases osmolarity and the forces which oppose blebbing (143, 144)	Blebs are typically larger.	9%	1Hr
Sucrose	Increases osmolarity and the forces which oppose blebbing (143, 144)	Blebs are typically smaller.	15%	1Hr, 4Hrs
Nocodazole	Disrupts microtubules by binding to $\beta$ -tubulin	Numerous blebs, typically covering the entire cell membrane surface.	65%	1Hr, 4Hrs
Latrunculin A	Depolymerizes actin filaments and disrupts microfilament mediated processes	Blebs appear incapable of retraction.	66%	1Hr, 4Hrs

**Table 4.1** BAECs were subjected to various cytoskeletal and membrane treatments. The effect on blebbing and total spreading area were observed. Percentage blebbing after 1Hr refers to the number of observed cells that possess blebs on the basal surface after 1 hr of spreading. Effect on spreading indicates the observed time points where the treated cells were significantly less spread cells (using Student's T-test  $p < 0.05$ ) compared to untreated control cells at 1 and/or 4 hours of spreading.

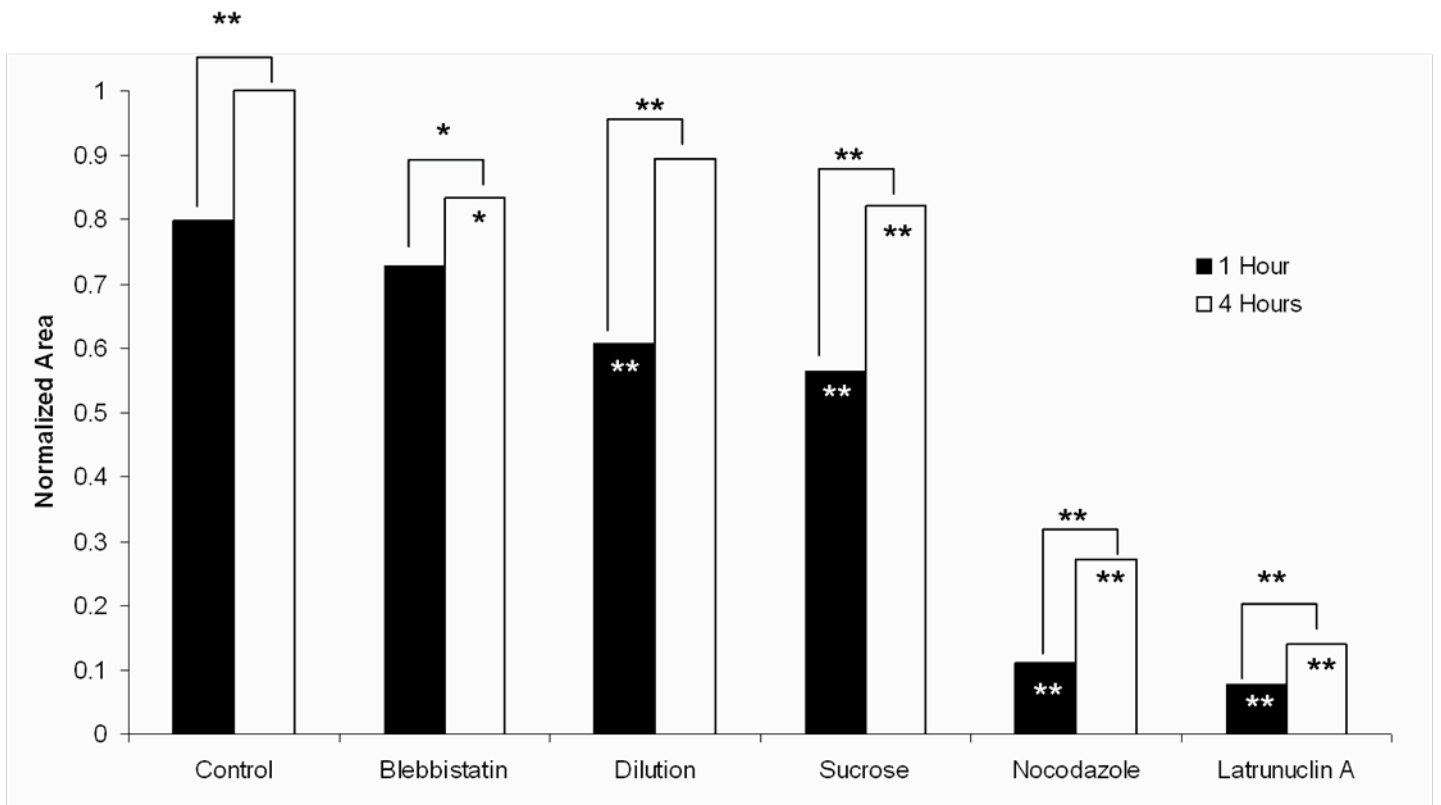


**Figure 4.1** Total spreading area was observed for cells (50-75) under each drug or osmotic treatment after 1 and 4 hours of spreading. Standard error is indicated, and statistical significance is reported using Student's T-test. \* for  $p < 0.05$  and \*\* is  $p < 0.01$ . All treatments, as well as control, significantly increase in area between 1 and 4 hours. At 1 hour, dilution, sucrose, nocodazole and latrunuclin A (latA) cells are less spread compared to control cells at 1 hour. After 4 hours, blebbistatin, sucrose, nocodazole and latA cells remain less spread compared to control cells at 4 hours.

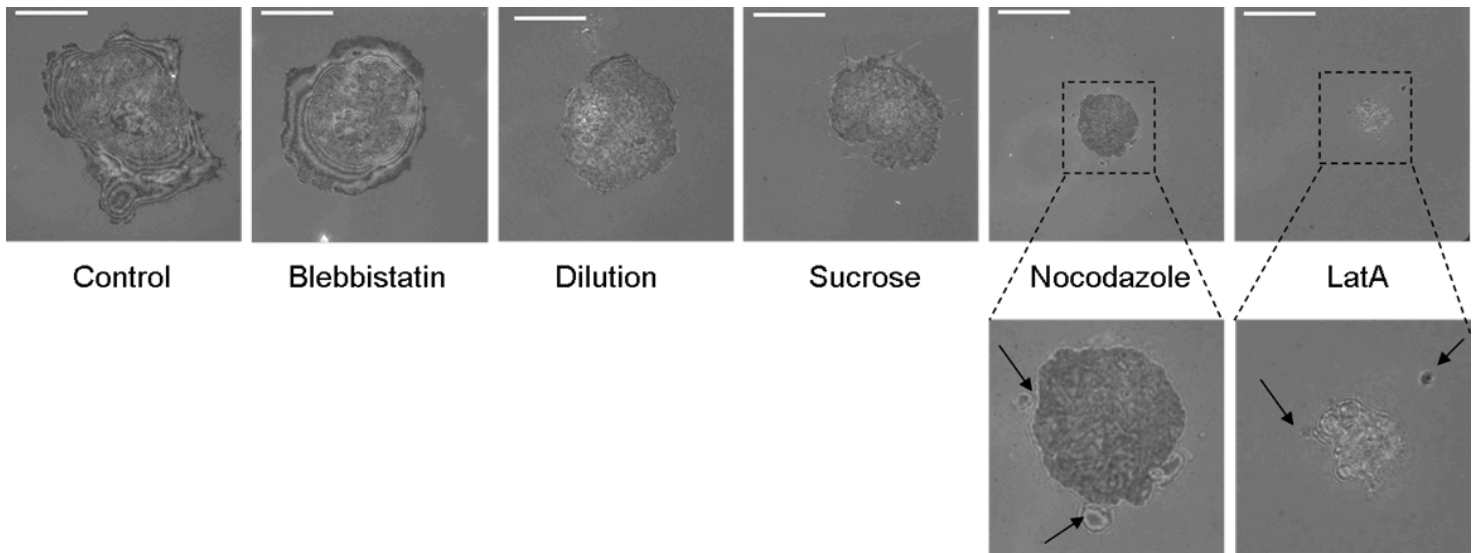


**Figure 4.2** Representative images of cells observed using interference reflectance microscopy (IRM) is illustrated for each treatment condition. Nocodazole and latA cells are magnified to illustrate blebs (arrows) observed on the basal surface during spreading after 1 hour. Note the white fringe-like appearance for latA treated cells. This light gray and white appearance observed using IRM illustrates weak attachment to the surface. Scale bar is 20 $\mu$ m.

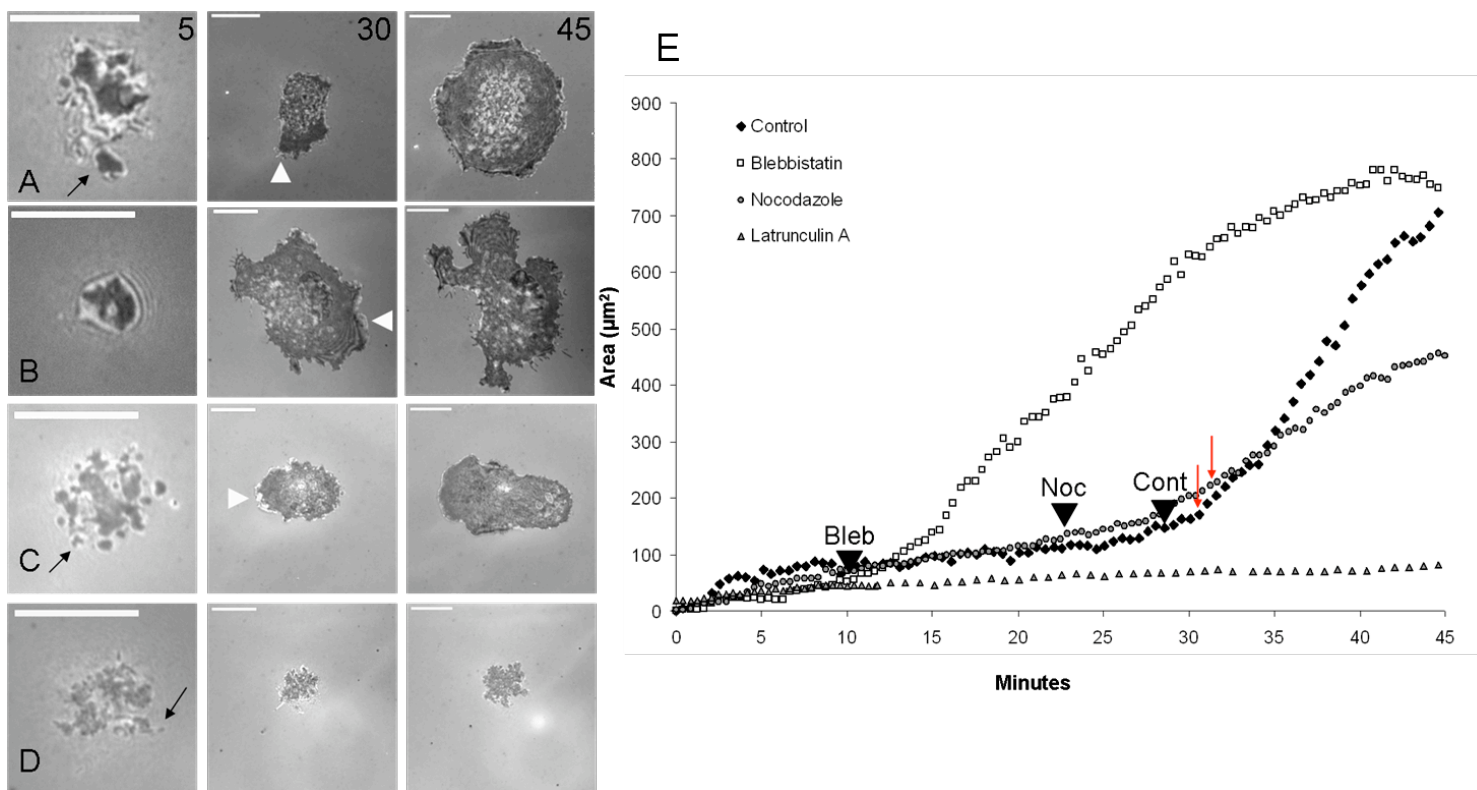


**Figure 4.3** (A-D) Snapshots of the single cell dynamics for control (A), blebbistatin (B), nocodazole (C), and latA (D) treated cells. Arrows represent blebs on the basal surface, while white arrowheads illustrate the appearance of lamella. Scale bar is 10μm in all images. (E) Single cell spreading dynamics for control, blebbistatin, nocodazole, and latA treated cells. Arrowheads indicate the initial observation of lamella on the basal surface for control (Cont) blebbistatin (Bleb) and nocodazole (Noc) cells, while the arrow indicates the disappearance of blebs.

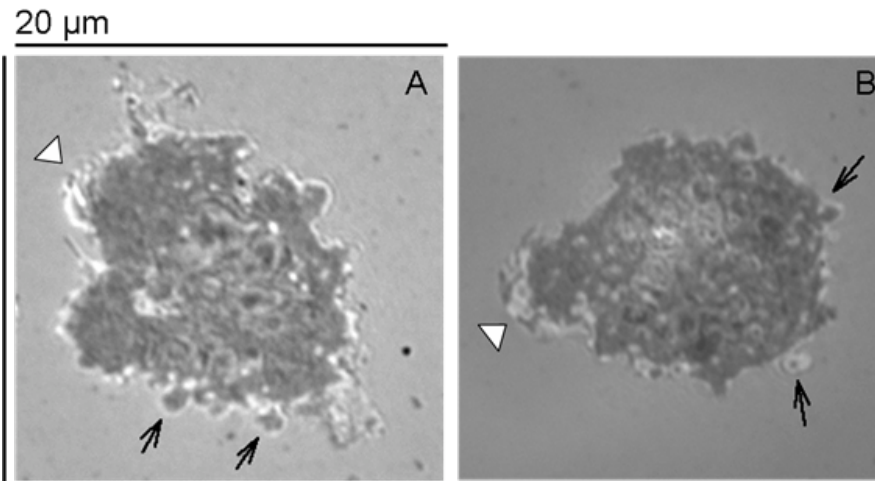


**Figure 4.4** Coexistence of blebs and lamella during spreading. These two separate examples illustrate that typically lamella (white arrowheads) appears in areas distant from the remaining blebs (black arrows). Lamella indicates the beginning of fast spreading, while the individual blebs continue to attach/retract from the surface.

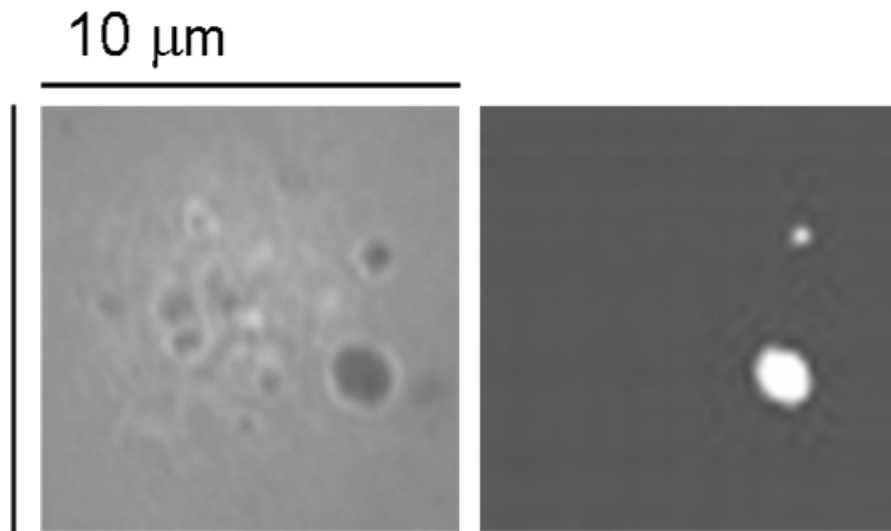


**Figure 4.5** Identification of individual bleb adhesions using self-written algorithms. The image on the left illustrates the initial attachment of blebs at T=0 minutes. The image on the right shows the identification of single blebs using the algorithms. Blebs are recognized and the area of bleb adhesion over time is stored from the first appearance of the bleb until it either completely retracts or attaches to another bleb or the central spreading area.

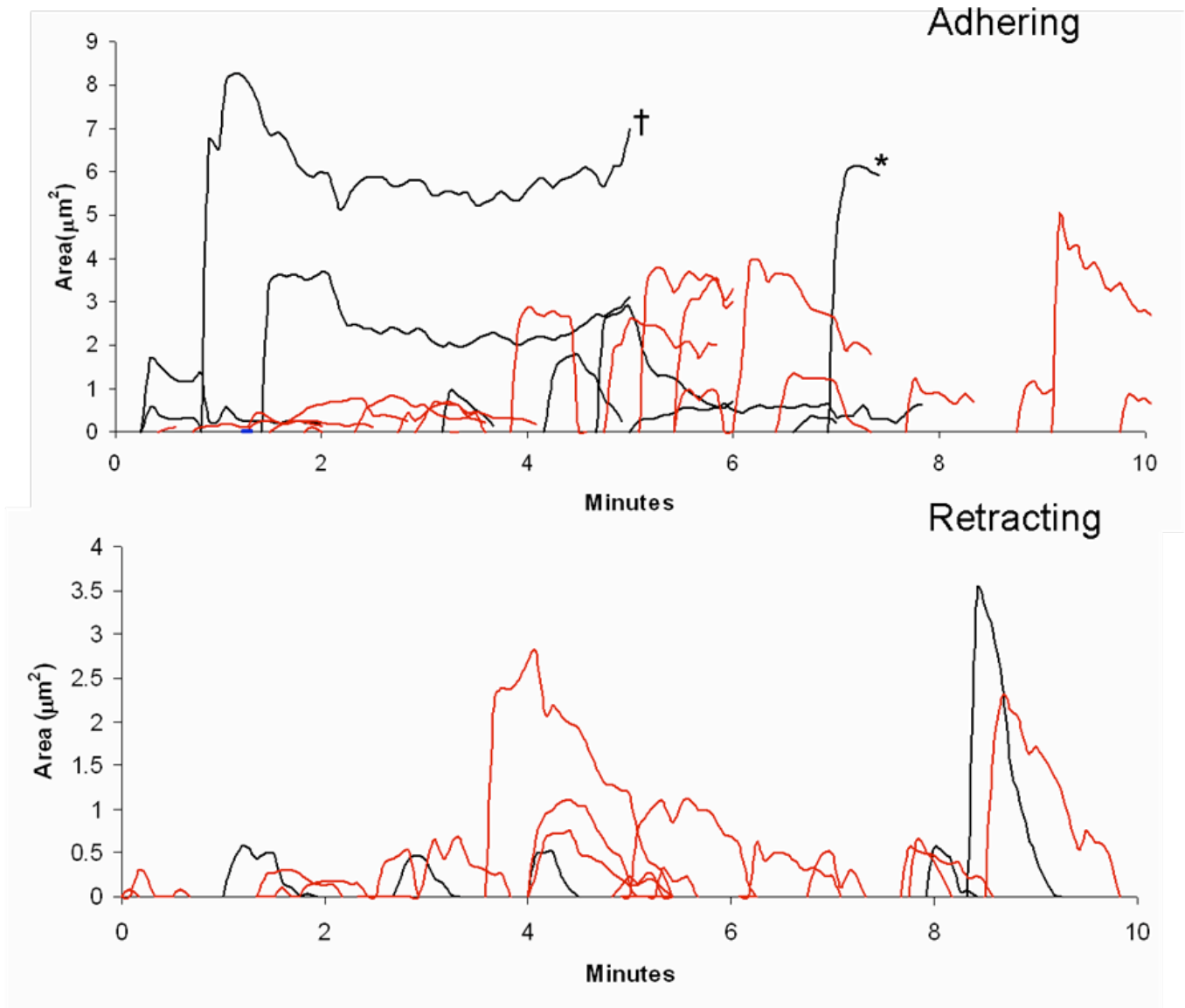


**Figure 4.6** Bleb-surface interactions observed using IRM reveal both adhering and retracting bleb-dynamics during the initial stages of spreading. Each line represents one bleb during the spreading process. Red lines correspond to nocodazole treated blebs, while control bleb dynamics are shown in black. Three types of adhesion behaviors were identified: 1) permanent adhesion 2) adhesion followed by partial detachment, and 3) adhesion followed by total retraction. Permanent adhesion is observed in blebs which have a sharp increase in adhesion area, with no subsequent decrease (marked with asterisk). Blebs often adhere and partially retract from the surface, illustrated by the sharp peak of adhesion followed by a slow decrease before solid attachment (marked with cross). Blebs which adhere and then completely retract are identified by a sharp increase and decrease in adhesion, which illustrate their quick adhesion and retraction dynamics. Initially, the majority of blebs appear to adhere to the surface, while blebs appearing later during the spreading process retract more frequently. These retracting blebs contribute to the slow spreading rate.

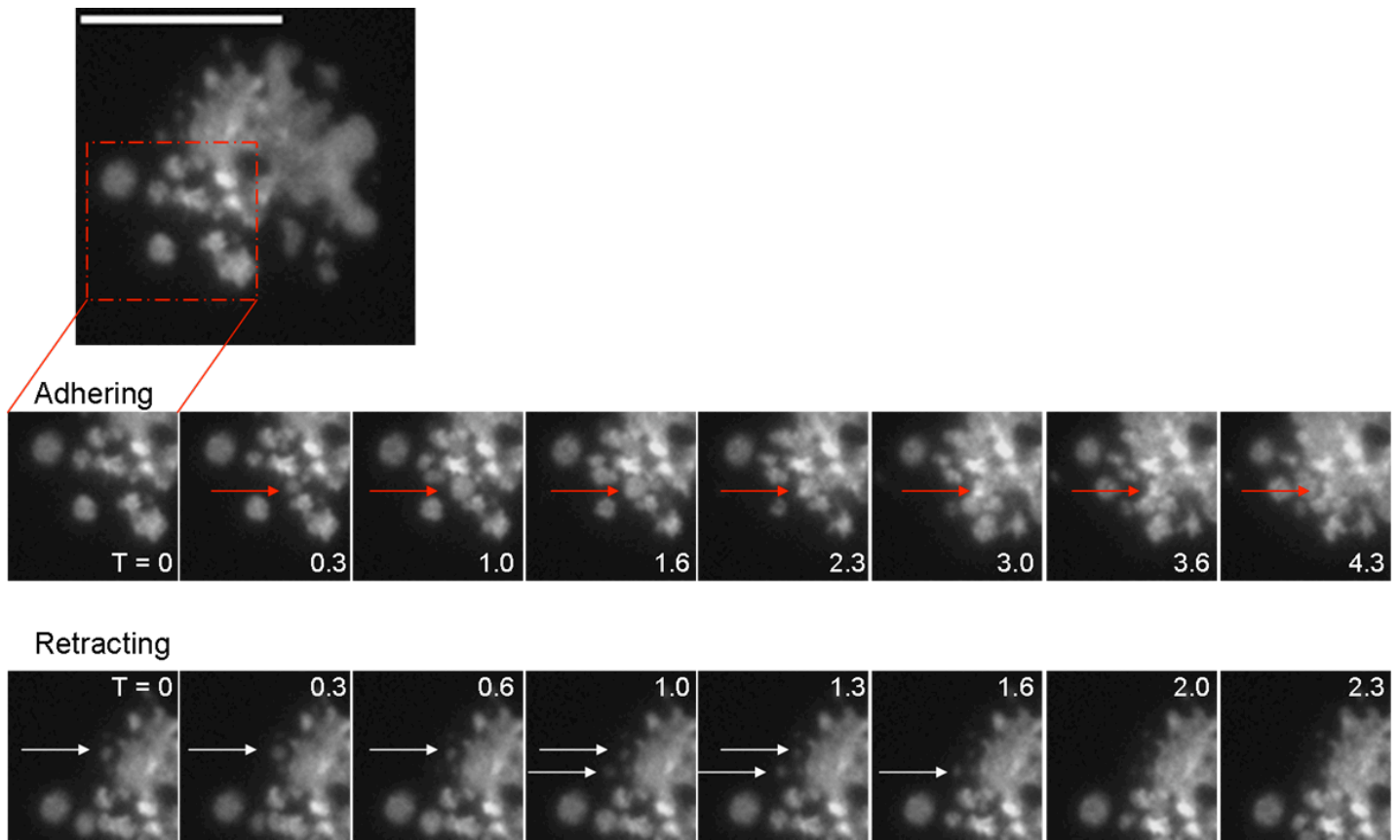


**Figure 4.7** Cellular bleb dynamics observed using total internal reflection fluorescence (TIRF) microscopy. BAECs were transfected with GFP-actin and allowed to re-spread on fibronectin-coated dishes (T = time in minutes). Characteristic adhering and retracting blebs are identified with arrows. Adhering blebs become “trapped” due to surrounding blebs and the spreading cell body. Retracting blebs are weaker in actin intensity and quickly touch and retract from the substrate. Scale bar = 5 $\mu$ m.

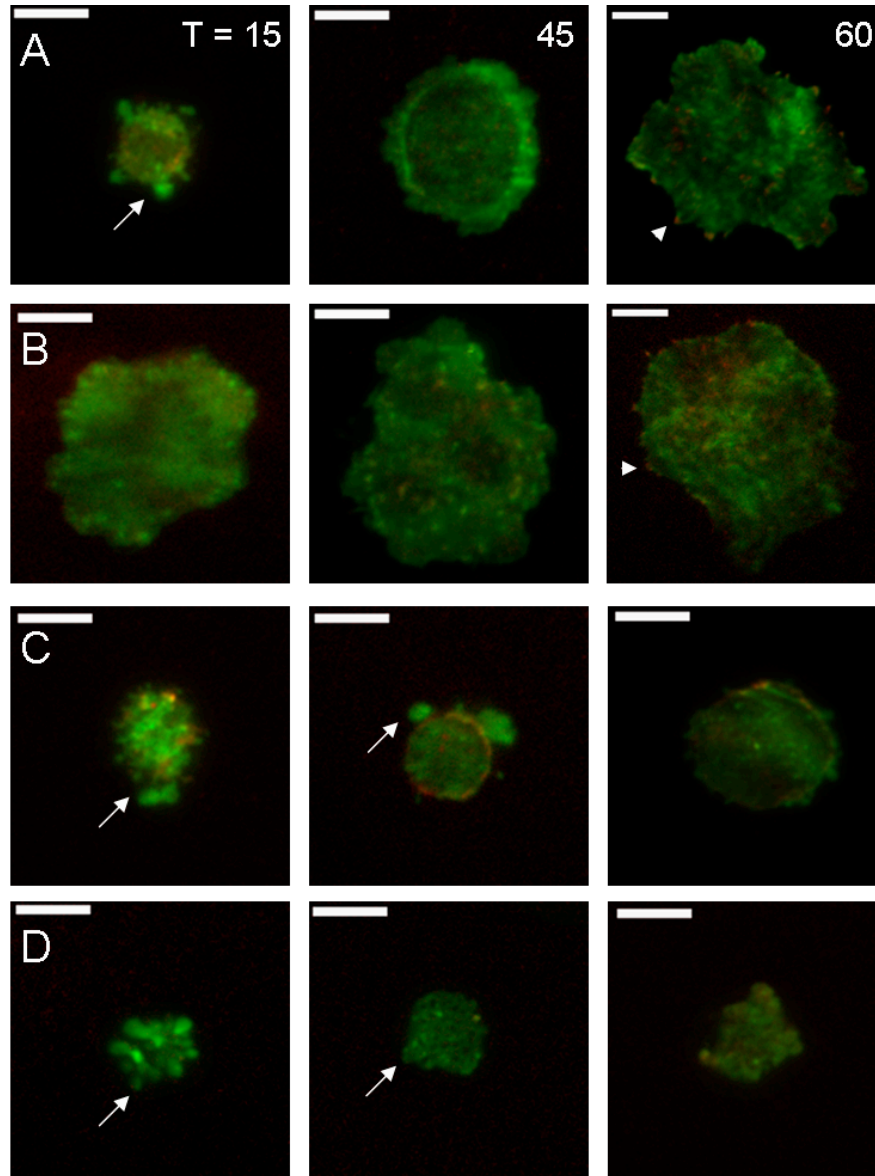


**Figure 4.8** Actin and paxillin organization during spreading of control (A), blebbistatin (B), nocodazole (C) and latA (D) treated cells. Cells were cotransfected with GFP-actin and mCherry-paxillin prior to the spreading process. Cells were detached and allowed to re-spread on fibronectin-coated dishes ( $T$  = spreading time in minutes). TIRF microscopy was used to observe actin/paxillin dynamics close to the substrate. Blebs are present on control, nocodazole and latA treated cells (arrows). Blebs have disappeared on control cells after 45 minutes of spreading, however they are still present on nocodazole and latA treated cells. In many nocodazole treated cells, paxillin appears on the periphery of the cell. After 60 minutes of spreading, distinct paxillin puncta are observed on both control and blebbistatin treated cells (arrowheads). Scale bars =  $10\mu\text{m}$ .

## **5 Modification of cellular cholesterol content affects traction force, adhesion and cell spreading<sup>†</sup>**

### **5.1 Introduction**

Cholesterol is one of the major lipid components of the plasma membrane, well known to be associated with multiple disorders such as atherosclerosis, lysosomal storage diseases (including Sandhoff, Tay-Sachs, and Niemann-Pick) and possibly Alzheimer's disease (182). Numerous studies have shown that cholesterol regulates a variety of membrane proteins, including multiple receptors and ion channels (183-187). More recently, however, it became increasingly clear that cholesterol effects are not limited to changes in membrane structure and altering the function of membrane proteins, but that cholesterol also has major indirect effects on the cytoskeleton. Several lines of evidence indicate that changes in membrane cholesterol can indirectly alter biochemical properties of the cytoskeleton and its association with the plasma membrane: (a) multiple studies have shown that cholesterol-rich membrane domains (lipid rafts) serve as focal points for membrane-cytoskeleton interactions (188); (b) depletion of membrane cholesterol increases cellular stiffness of endothelial cells (189), an effect that is the opposite to the expected changes in membrane lipid bilayer where cholesterol depletion results in a reduction in bilayer thickness (190) and a decrease in membrane stiffness in artificial lipid layers (191); (c) cholesterol depletion also increases contractile forces generated by the cells in 3D collagen matrix (192) and (d) strengthens membrane-cytoskeleton

---

<sup>†</sup> This section has been published as: Norman, LL *et al.* 2010. Modification of cellular cholesterol content affects traction force, adhesion and cell spreading. Cellular and Molecular Bioengineering. (DOI # 10.1007/s12195-010-0119x).

adhesion (193). Cholesterol depletion also facilitates shear stress-induced realignment of endothelial cells, as well as individual F-actin fibers, in the direction of flow (194). Interestingly, reported effects of cholesterol depletion on stress fibers have varied, with one group showing a decrease in the size of stress fibers in human fibroblasts (195) while, alternatively no differences in actin intensity were reported for cholesterol depleted bovine aortic endothelial cells (189). Differences in cell type, depletion times, and vehicle treatment for control cells are all factors which may contribute to these differences.

One possibility to explain the above mentioned increase in cell stiffness is that it is due to a decrease in actin turnover leading to the stabilization of the membrane-cytoskeleton complex (195-197). Alternatively, because cholesterol depletion increases cortical actin (183), this may also lead to larger traction stresses as observed in 3D collagen gels (192) and, therefore, the cell may appear stiffer (196). Indeed, a strong association between increased cell stiffness and tensile stress has been reported for human airway smooth muscle cells, even though the study did not focus on cholesterol modification (198). This suggests that identification of individual cell traction forces from cholesterol-modified cells is necessary to properly elucidate the association among cholesterol depletion, membrane stiffness and traction stresses.

Lipid organization and cholesterol content is not only critical at the single-cell level, but appears just as important in monolayer formation and regulation. For example, in cow pulmonary endothelial cells, the plasma membrane of the cells undergo functional and structural changes as the cells become a confluent monolayer. This includes an increase in the membrane cholesterol, adherens junctions formation, and tyrosine

dephosphorylation of adherens junctions proteins (AJPs) (199). This dephosphorylation is necessary for the formation of confluent endothelial monolayers, since increased tyrosine phosphorylation of AJPs results in the disruption of adherens junctions (200, 201). In cholesterol-enriched and untreated confluent cells, immunofluorescence staining of AJP pp120 was concentrated along adherens junctions. However, cholesterol depletion on confluent cells resulted in diffuse cytoplasmic staining and large gaps between adjacent cells. The observed results indicate that cholesterol depletion of confluent cells results in plasma membrane retraction from cell-cell interaction sites and disruption of adherens junctions by inducing tyrosine phosphorylation of AJPs. However, the mechanisms of cholesterol regulation on formation of confluent cells and stability of adherens junctions remain unknown (199).

Based on recent studies, which have shown that cholesterol depletion in human aortic endothelial cells increases cellular stiffness and force generation (192) and decreases L27 cell adhesion to fibronectin-coated substrates (202), we hypothesize that a similar effect will be seen in BAEC traction stresses, i.e. cholesterol depletion from cells increases the force that cells exert on the substrate. In turn, these larger forces translate into cell traction, which affects monolayer stability and cell spreading. We investigated the role of cholesterol in the force exerted by BAECs on polyacrylamide gels using traction force microscopy (TFM). Independently, we also studied the effect of cholesterol on cell adhesion and spreading dynamics, using TIRF and IRM to visualize the adhesive contact between the cell membrane and the substrate. Our results show that the total average traction force generated by cells increases in cholesterol-depleted cells and remains the same in cholesterol-enriched cells. The average size of focal adhesions

for single cells depleted of cholesterol also increases. Interestingly, we report a decrease in the spreading area of both single cells and monolayers for cholesterol- depleted cells. During spreading, depleted cells spread statistically less than controls, while enriched cells were not statistically different. Cell spreading is prevented initially due to an increase in cortical actin, and is likely further affected due to increased traction forces and adhesions at later times. Our results emphasize the importance of cholesterol in controlling and regulating the mechanical properties of the actin-plasma membrane complex, and the cellular mechanisms required for spreading.

## ***5.2 Materials and methods***

### **5.2.1 Cell culture**

Bovine aortic endothelial cells (BAECs) were purchased from Cambrex (East Rutherford, NJ) and cultured as described above in section 3.2.1. Cells were plated on polyacrylamide (PA) gels for traction force microscopy measurements, or glass coated with 0.1 mg/mL fibronectin (Sigma-Aldrich, St. Louis, MO) for IRM and TIRF microscopy measurements.

### **5.2.2 Coverslip activation and polyacrylamide gel preparation**

Cover slips were chemically activated to allow covalent attachment of PA sheets (described further in Appendix A and (203)). Acrylamide gels were prepared as described elsewhere (204) with a few modifications (see Appendix A for further details). Fluorescent latex spheres (1  $\mu\text{m}$  Flurospheres, Molecular Probes, Eugene, OR) were added to the acrylamide solution in volume ratio of 1:100. After the solution was degassed, polymerization was initiated by addition of 1:200 volume of ammonium

persulfate (10% w/v solution, Bio-Rad) and 1:20,000 volume of N'-Tetramethylethylene diamine. Afterwards, the acrylamide solution was placed onto a circular cover slip (No. 1.5, 22-mm diameter, Fisher Scientific, Pittsburgh, PA) and the activated cover slips were placed on top. The resulting assembly was turned upside-down and polymerized for 45 minutes. The circular cover slip was removed and the gel was rinsed with 50 mM HEPES. Then, 250 $\mu$ L of 0.1mg/mL fibronectin solution (Sigma-Aldrich) was placed on the activated gel. After 2 hrs, the gel was rinsed with PBS and further incubated in 300 $\mu$ L of ethanolamine diluted 1:100 in PBS + 50 mM HEPES at room temperature for 30 minutes, and finally sterilized with UV radiation. The thickness of the polyacrylamide gel was estimated to be 80  $\mu$ m with a Young's modulus of 2,500 Pa as characterized previously (204).

### **5.2.3 Cholesterol treatment**

BAECs were rinsed with serum-free DMEM and the cholesterol content was modified by incubating for 1 hr in methyl- $\beta$ -cyclodextrin (M $\beta$ CD) saturated with cholesterol (enrichment), M $\beta$ CD not complexed with cholesterol (depletion), and M $\beta$ CD/M $\beta$ CD-cholesterol mixture at a molar ratio that the level of cellular cholesterol was identical to the untreated cells (control) (184, 205). The cells were rinsed again with serum-free DMEM after cholesterol treatment.

For spreading experiments, cells were plated in the presence of cholesterol enrichment or depletion; 2mls of (M $\beta$ CD) saturated with cholesterol, and without cholesterol, respectively was added to a fibronectin-coated glass bottom dish (No. 1.5, MatTek Co., Ashland, MA). Control cells were exposed to M $\beta$ CD/M $\beta$ CD-cholesterol mixture at a molar ratio that the level of cellular cholesterol was identical to the untreated

cells during spreading experiments. For all experiments, cholesterol depletion, enrichment and control were performed in the same manner (as described above) and observed after 1 hour to ensure identical conditions.

#### **5.2.4 Fluorescence labeling of BAEC monolayers**

Cells were plated onto fibronectin-coated glass-bottom dishes and reached confluence within 2 days. After cholesterol treatment, the monolayers were stained for 3 minutes using a lipophilic probe (lipid analog) 5  $\mu$ M of 1,1'-dihexadecyl-3,3,3',3'-tetramethylindocarbocyanine perchlorate (DiIC<sub>16</sub>) in DMEM. The monolayers were rinsed with PBS and fixed with 2% paraformaldehyde for 20 minutes at room temperature before a final rinse with PBS.

#### **5.2.5 Traction force microscopy**

TFM is a common method to measure the forces exerted by cells on compliant substrates (198, 206-209). Here, we used the method developed by Dembo *et al.*, where the traction forces generated by migrating cells on the underlying substrate were quantified based on the displacements of the beads embedded in the substrate (208). Briefly, cells are plated on PA gels embedded with fluorescent markers and the cells are allowed to adhere and spread on the substrate for 24 hrs. Fluorescent and phase contrast images of the spread cells and embedded beads are captured. Finally, the cells are removed using trypsin-EDTA and the final fluorescence images of the relaxed markers are captured. Based on the properties of the PA gel and the bead displacements, the traction forces can be calculated using the technique described by Dembo and Wang (208). As previously described (210), the overall force of the cell,  $|F|$ , is an integral of

the traction field magnitude over the area,  $|F| = \iint \sqrt{T_x^2(x,y) + T_y^2(x,y)} dx dy$  where  $\mathbf{T}(x,y) = [T_x(x,y), T_y(x,y)]$  is the continuous field of traction vectors defined at any spatial position  $(x,y)$  within the cell.

### **5.2.5 Interference reflection microscopy**

IRM was used to evaluate cell spreading behavior in the same manner as that described above in section 3.2.3 and Appendix B.

### **5.2.6 Total internal reflection fluorescence microscopy**

TIRF microscopy was used to evaluate cell-substrate interactions. For further details on this method see Appendix B. Single BAECs were fixed as described above for monolayers and stained for vinculin using first a 1:200 dilution of Anti-vinculin primary antibody (Sigma), followed by a 1:200 dilution of Alexa-fluor 488 Anti-mouse secondary antibody (Invitrogen). TIRF images were captured on an inverted microscope (Olympus) fibre-optically coupled with two ion lasers (Melles Griot, Rochester, NY) for 488nm and 561nm excitation, and a CCD camera (Rolera-MGi, QImaging).

### **5.2.7 Data Analysis**

For spreading area measurements of single cells, ImageJ (National Institutes of Health, Bethesda, MD) software was used to trace the cell borders and to quantify the total area. To quantify the area covered by the cells of control and treated monolayers, the light intensity threshold analysis of ImageJ software was used. In brief, snapshots were taken of 13-15 locations on separate monolayers after treatment and fixing procedure as mentioned above. These fluorescent snapshots were converted into binary

images, which distinguished cell adhesion areas (fluorescent due to DiIC staining) versus gaps in the monolayer (black). The amount of surface coverage from these binary images (not including gaps in the monolayer) is referred to as the average monolayer area.

ImageJ was also used for the quantification of the average vinculin adhesion area. All images were converted to binary images to isolate individual vinculin adhesions, and the particle analyzer in ImageJ was used to detect all adhesions greater than  $0.5\mu\text{m}^2$  to prevent the quantification of background noise. The average vinculin adhesion area was recorded for each individual cell.

## ***5.3 Results***

### **5.3.1 Cholesterol-depletion increases the average traction force**

TFM was used to measure the total average force exerted by endothelial cells on polyacrylamide (PA) gel substrates. Figure 5.1A shows an endothelial cell on a PA gel with  $1\mu\text{m}$  fluorescent embedded beads and the corresponding traction map in pseudocolor (Figure 5.1B), indicating regions of low and high traction stresses in Pascals (dark blue to light pink). The traction forces were determined based on displacements of the embedded beads due to deformations on the gel surface, and the colored map indicates that the traction stresses are larger at the edges of the cell. The localization of larger traction stresses at the edge of the cell is consistent with previous work (204), where it was shown that increased traction stresses exists underneath actin-rich pseudopodia compared to areas of adhesion underneath the nucleus. Note that cells that had no contact with adjacent cells were chosen to ensure no cell-cell interaction effect on cell spreading area and traction force. Traction forces were quantified in this manner for

both cholesterol-depleted (cells treated with methyl- $\beta$ -cyclodextrin (M $\beta$ CD)) and cholesterol-enriched cells (M $\beta$ CD saturated with cholesterol) as well as control cells (M $\beta$ CD/M $\beta$ CD-cholesterol mixture at a molar ratio that the level of cellular cholesterol was identical to the untreated cells).

The average total force exerted by cells onto the PA gel was statistically greater in cholesterol-depleted cells, with an almost two-fold increase compared to control and cholesterol-enriched cells (Figure 5.1C). No statistical differences occur between control and cholesterol-enriched cells. This is in agreement with work that shows no significant effect of cholesterol enrichment on the membrane stiffness (189); therefore, we would not expect to see increases in traction forces. Although force and cell spreading area vary among individual cells, it has been shown that these are dependent variables (204), meaning that cells with increased areas exert increased traction forces. In this study, we specifically chose cells of similar spreading areas when performing TFM, which ensures that the increase in traction forces with cholesterol-depleted cells is not due to an increase in cell spreading area. To ensure that selected cells were characteristic of the entire population, cells were blindly selected within one standard deviation from the mean of the entire population. Figure 5.1D illustrates that for the cells which were selected, there are no statistical differences in the average area among control, cholesterol-depleted, or cholesterol-enriched cells. This does not suggest that cholesterol modification does not affect the cell spreading area, but rather that cells observed for force traction experiments were selected with similar areas to ensure that increased traction forces is not a result of increased spreading area. In addition to increased membrane stiffness for cholesterol depleted cells, it is possible that increased cell-substrate adhesion may contribute to the

observed increases in traction forces, as many others have shown close relationships between focal adhesions and force (206, 211, 212). To further evaluate this possibility, we used TIRF microscopy to quantify cell-substrate adhesion.

### **5.3.2 Cholesterol-depletion increases focal adhesion size**

Earlier studies have shown an association between increased forces and increased focal adhesions (206, 209, 213). Focal adhesions are involved in anchoring cells to the extracellular matrix substrates via actin-myosin and integrin receptors. These mechanosensitive cellular features can modify their shape, size and distribution in response to applied stress (206, 214). Due to the observed increase in traction forces for cholesterol-depleted cells, one would expect to see a potential increase in focal adhesion formation. To further understand the effect of cholesterol treatment on focal adhesions, vinculin (a focal adhesion protein) staining was observed using TIRF.

Vinculin staining is displayed in Figure 5.2A for a characteristic cell using TIRF microscopy. ImageJ software was used to create binary images and to identify individual vinculin adhesion sites (Figure 5.2B). The contact area of each vinculin site was quantified for each cell (as described in the Materials and Methods section) and the average size for each treatment is reported in Figure 5.2C. The average contact area of individual vinculin adhesion sites is significantly increased in cholesterol-depleted cells, compared to cholesterol-enriched and control cells. No differences appear between control and cholesterol-enriched cells. This is consistent with earlier studies (206) and confirms the suspected relationship between increased focal adhesions and increased traction forces.

In addition to focal adhesions, stress fibers are also associated with traction forces (215). Although it was previously reported that BAECs do not display differences in actin intensity when depleted of cholesterol (189), we repeated these experiments by fixing cells and staining with phalloidin-TRITC. We then used TIRF microscopy to quantify the amount of actin fluorescence for control, depleted and enriched cells. Consistent with this previous work (189), we do not see any significant differences in the actin intensity between control and cholesterol modifications (data not shown). Collectively, this illustrates that although it appears that focal adhesions (as determined through vinculin staining) contribute to the observed increased traction forces, it does not appear to be the case for actin. Note that force traction experiments are performed on compliant substrates, and TIRF microscopy is performed using glass substrates; therefore the formation of focal adhesions may be magnified on glass, since others have observed increased vinculin staining on increased stiffness (216, 217). However, we do not have reason to suspect that the relationship between treatments would change. To further elucidate these concepts, future approaches would require a more thorough understanding of how cholesterol modification may be altered on substrates of varying stiffness.

To determine whether cell-substrate spreading area changes during the process of cholesterol depletion, as previously shown by Ramprasad *et al.* for L27 cells (202), snapshots were captured using IRM during cholesterol depletion at 10 minute intervals. As expected, cells depleted of cholesterol which were well spread out, detached significantly from the substrate during the first 20 minutes of incubation. However, after 20 minutes detachment ceased (data not shown). Cells remain statistically less adhered for the remainder of the observed hour, illustrating that cholesterol depletion decreases

the spreading area of single cells. Figure 5.3 illustrates the significant decrease in spreading area for cholesterol-depleted cells plated on glass, while no differences are observed between control and cholesterol-enriched cells. Collectively, these data show that increased traction forces are associated with an increase in focal adhesion and also cell-substrate detachment.

### **5.3.3 Cholesterol treatment affects spreading behavior**

As previously mentioned, cholesterol depletion has been shown to increase cortical F-actin (183), and plasma membrane stiffness (189, 192). Increased membrane stiffness and cortical actin concentration suggest that cholesterol depletion may cause decreased cell spreading. The increase in cortical actin might result in an increase of cellular tension. This increase in tension can inhibit the initial cell spreading stages (181), and may result in less spread cells. The increase in traction forces and adhesion for cholesterol-depleted cells are additional variables which may contribute to the inhibition of spreading (by increasing forces which oppose lamellipodial spreading); however, these variables would be involved later in the spreading process.

The effect of cholesterol on cell spreading was identified by observing spreading behavior during the process of cholesterol depletion or enrichment. To do so, cells were detached from the substrate as described for continuous passaging, and plated immediately onto freshly fibronectin-coated glass bottom dishes filled with M $\beta$ CD saturated with cholesterol (enrichment) without cholesterol (depletion), or vehicle (control). Cells were left undisturbed for 1 hour, and individual cells were then first identified using bright field microscopy to ensure single cells. Snapshots were taken using IRM to determine total spreading area (2). The average spreading area for each

condition is illustrated in Figure 5.4. As expected, statistical differences in total spreading area are observed between cholesterol-depleted and control cells, as well as cholesterol-depleted and cholesterol-enriched cells ( $p < 0.001$ , Student's T-test). No differences are observed between cholesterol-enriched and control cells. Although previous experiments illustrate no difference in cell areas between control and cholesterol-depleted cells after 24 hours (194), we do report differences during the first hour of spreading. Since cells continuously regulate cholesterol levels over time in order to maintain homeostasis, we observe the early stages of spreading to ensure that cells do not have time to properly modify cholesterol content.

Cholesterol depletion decreases spreading area more than 30% compared to controlled cells (Figure 5.4). This dramatic effect is consistent with others who show decreased motility and adhesion to fibronectin-coated substrates (202). This group shows that cholesterol depletion in L27 cells plated onto fibronectin-coated surfaces resulted in the disappearance of lamellipodia and stress fibers, and an increase in cortical actin concentration. This indicates higher cortical tension (known to inhibit spreading (181)) and decreased motility, in agreement with the decrease we observe during the first hour of spreading for cholesterol-depleted cells. Also of importance, Ramprasad and colleagues (202) show that actin stress fibers were reformed when membrane cholesterol content was restored, suggesting that the changes observed in motility and adhesion are related to the reorganization of the actin cytoskeleton. Therefore, cholesterol does not appear to have a direct effect on actin polymerization, but rather on the organization of F-actin cytoskeleton and membrane stiffness at the leading edge of the lamellipodia (202), critical components of cell spreading.

The increase in cell-substrate adhesion that we report above (Figure 5.2) correlates with the increased cytoskeleton-membrane adhesion occurring after cholesterol depletion, which is expected to significantly affect cell functions, including endocytosis (193). It is suspected that this increase in adhesion makes it difficult for cells to form endocytic vesicles and therefore, the rate of endocytosis is decreased. This reduction in endocytosis would agree with our decreased spreading rates, since various endocytic pathways have been associated with spreading and ruffling (218). In addition to endocytosis, exocytosis has also been shown as a critical component of the cell spreading process, by aiding to increase the plasma membrane area (150). Others have suggested that cholesterol and sphingolipid-rich microdomains of alveolar epithelial type II cells serve as functional platforms during exocytosis (219). When these cells were depleted of cholesterol, exocytosis was inhibited (219). Together these results suggest that cholesterol depletion can cause a decrease in exocytosis, which in turn reduces the spreading area, consistent with our observation (Figure 5.4). In addition, others have previously shown that depletion of cholesterol from the plasma membrane of fully spread cells causes a reduction in cell adhesion and motility (202). Our measurements further support these observations by showing decreased spreading for cells depleted of cholesterol. This data emphasizes the important relationship between membrane composition, adhesion and cell spreading.

#### **5.3.4 Monolayer area decreases with both cholesterol depletion and enrichment**

Endothelial cells approaching confluence undergo intense structural and functional alterations, including a 3-fold increase in cholesterol levels and the formation of adherens junctions (199). This significant increase in cholesterol levels suggests a

critical role of cellular cholesterol in regulatory pathways involved in cell-cell interactions and plasma membrane regulation. Previous studies have shown that cholesterol depletion on confluent cells disrupts intercellular junctions, and causes cell detachment (199, 220), however, specific cell-substrate interactions and retraction behavior is not completely clear. In our study, we aimed to observe the effect of cholesterol treatment on BAEC confluent monolayers plated on fibronectin-coated glass, by observing the changes in cell-substrate and cell-cell adhesion over the course of 1 hour. The cholesterol treatment includes control, and 30 and 60 min cholesterol-depleted and enriched confluent cells. The confluent monolayers were stained with lipid analog DiIC<sub>16</sub> and fixed with 2% paraformaldehyde. Images of the monolayers were captured and ImageJ software was used to quantify the total monolayer area after treatment.

Figure 5.5A shows the average monolayer area and indicates that cholesterol depletion significantly reduces the average monolayer area compared to control monolayer. This effect is even more pronounced for a longer time period of cholesterol depletion. Statistical differences are reported between cholesterol depletion at 30 minutes compared to 60 minutes (Student's T-test,  $p < 0.05$ ). Within 30 minutes of incubation, cholesterol enrichment also significantly decreases the average monolayer area. Representative monolayer images after 60 minutes of treatment are shown in Figure 5.5B, with the identified boxed region magnified in Figure 5.5C. For the control cells, the monolayer remains intact, as illustrated by the continuous cell coverage and very little substrate (black) observed. For cholesterol depleted cells, some cells have rounded up and are almost entirely detached from the substrate (white arrow). This observed detachment of the endothelial sheets is also consistent with the behavior observed for

single cells, which slightly retract from the surface during cholesterol depletion as mentioned above and displayed in Figure 5.3. Cell-substrate detachment is also noticed in cholesterol-enriched monolayers, although to a lesser degree. Cell-cell detachment is observed in both cholesterol-enriched and cholesterol-depleted monolayers and can be easily distinguished based on tethering observed between cell groups (Figure 5.5C). This illustrates that both cholesterol enrichment and depletion affect the average monolayer area, with 60 minutes of cholesterol depletion having the most dramatic influence.

Since cholesterol-depleted cells show a decrease in spreading area for both single cells (Figure 5.3) and monolayers (Figure 5.5), it was of interest to determine whether the increase in focal adhesions observed for single cells (Figure 5.2) was retained in cholesterol-depleted monolayers. Control, as well as cholesterol-depleted and cholesterol-enriched monolayers were fixed and stained for vinculin as described for single cells. However, no difference in the average size of focal adhesions was identified among the treated monolayers compared to control (data not shown). This is contrary to the effect observed in single cells; however, it is not entirely surprising due to differences in integrin clustering, actin organization, spreading area and/or force traction, which are all variables that can affect adhesion and focal adhesion morphology (41, 204, 206, 221). In addition, differences in the integrity of the monolayer (as shown in Figure 5.5) due to cholesterol modification may affect focal adhesion morphology for monolayers.

In sum, these observations confirm that cholesterol is a critical component in the proper formation of cell-cell and cell-substrate contacts necessary to maintain BAEC monolayers. Endothelial sheets serve in a variety of ways to maintain essential vascular tissue physiology by helping to regulate blood clotting and blood vessel diameter, and by

serving as a barrier which selectively allows for the transport of molecules between blood and tissue surfaces (199, 222). The endothelium also functions as a critical component of the immune response system by regulating leukocyte docking and transmigration (199). Our results illustrate that cholesterol-depletion (as well as enrichment) compromises the integrity of the endothelial barrier by inducing cell-cell and cell-substrate detachment.

#### ***5.4 Conclusions***

This work demonstrates that cholesterol depletion from BAECs increases the force that cells exert on the substrate. In turn, these increased cell tractions affect individual cell spreading dynamics, adhesion and monolayer stability. Our results emphasize the importance of cholesterol in controlling and regulating the mechanical properties of the actin-plasma membrane complex, and the cellular mechanisms required for spreading. In addition, these results suggest that cellular cholesterol has global effects on cell properties through changes in actin cytoskeleton, beyond the local membrane environment. Interaction of the cell membrane with the underlying cytoskeleton (membrane-cytoskeleton adhesion) has a major impact on vital cell functions, such as endocytosis, exocytosis, membrane extension and retraction, cell morphology, and migration (223). Ultimately, the results we present here emphasize the importance of cholesterol in regulating cell adhesion and spreading as well as monolayer structure and maintenance. Additional studies correlating the relationship between cellular changes following cholesterol modification and the signaling pathways which may relate these changes to disease will be of significant interest in relation to treatments for atherosclerosis and lipid organization disorders.

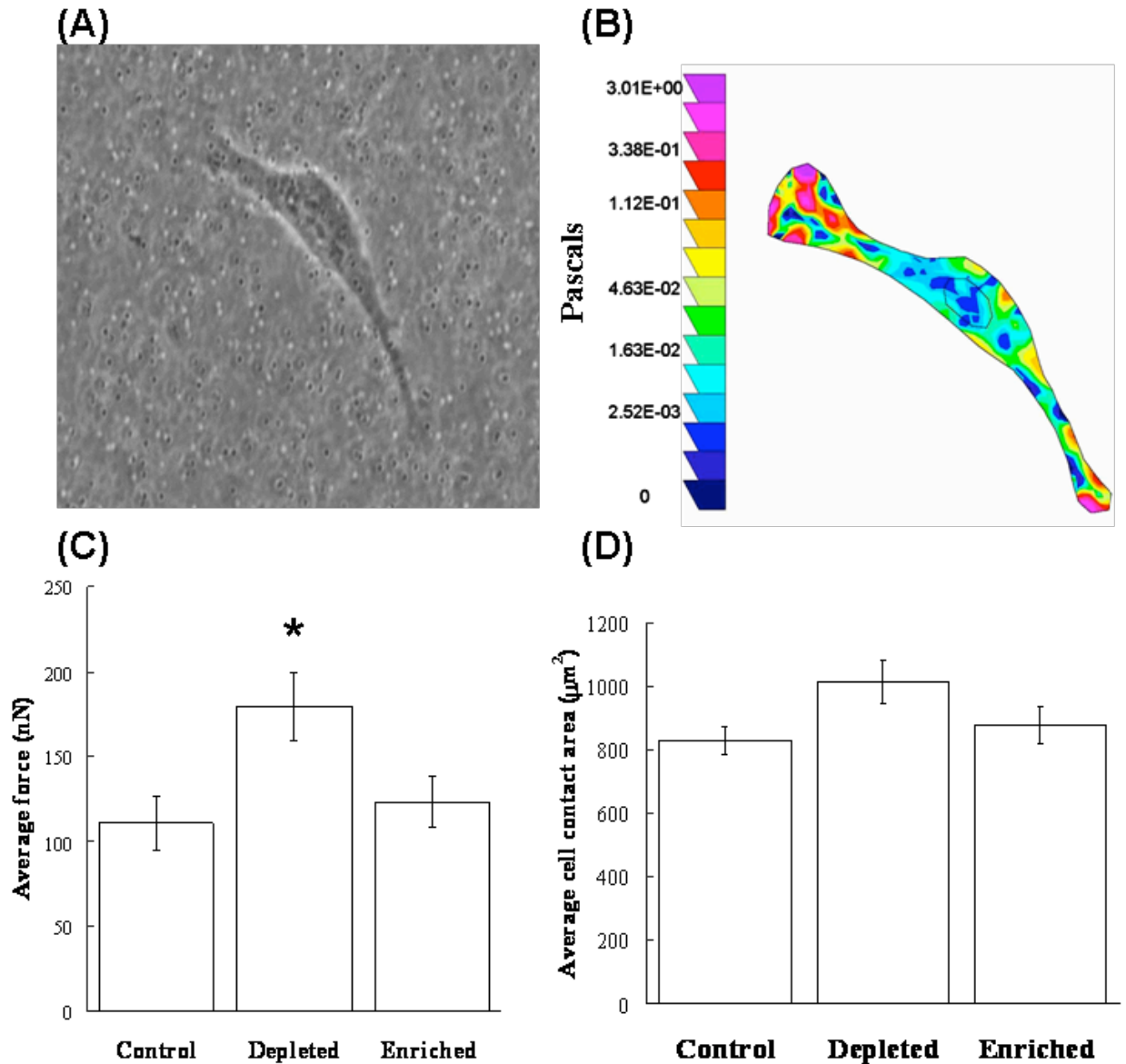


**Figure 5.1** Effect of cellular cholesterol on cell traction forces. (A) Bovine aortic endothelial cells (BAECs) were cultured onto polyacrylamide gels embedded with fluorescent beads for traction force microscopy. Cells spread for 24 hours, and fluorescent images were taken before and after cell detachment. (B) Traction forces were quantified by measuring the bead displacements, and a corresponding color traction maps illustrates the largest forces appear at the cell edge. The pseudocolor bar represents traction stresses in Pascals. (C) Average force exerted by the cell for control (N=18), cholesterol-depleted (N=21), and cholesterol-enriched (N=18) cells. The traction forces for cholesterol-depleted cells were statistically larger than the control and cholesterol-enriched cells (using Student's T-test, with  $p < 0.05$ ). (D) No significant differences are observed in the average cell area for control (N=18), cholesterol-depleted (N=21), or cholesterol-enriched (N=18) cells. Note this area represents the average spreading area only for cells selected for traction experiments, and does not represent the entire population of cholesterol treated cells. Error bars represent standard error.

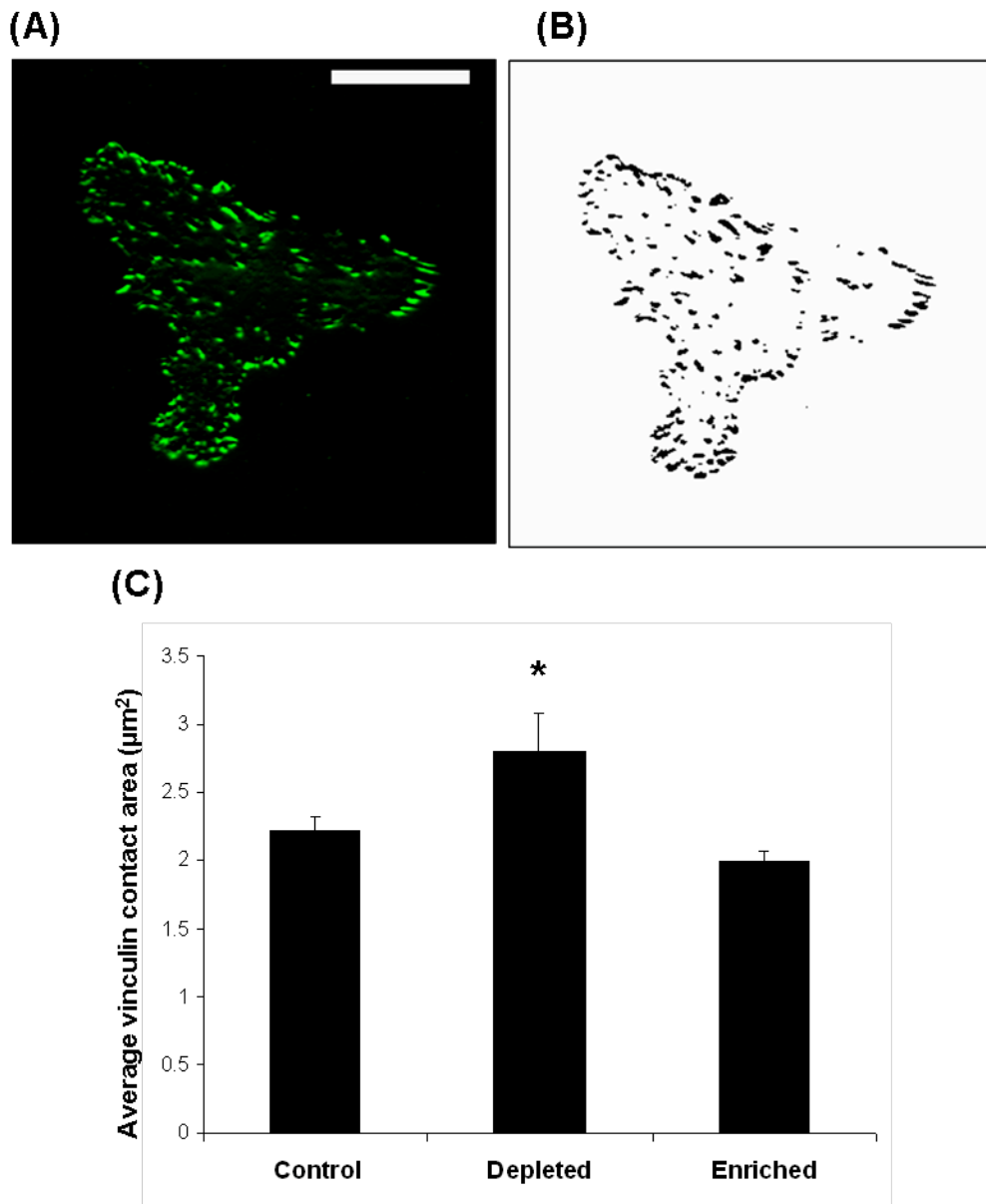


**Figure 5.2** Identification of the average vinculin contact area using total internal reflection fluorescence (TIRF) microscopy. (A) TIRF microscopy is used to identify vinculin adhesion sites close to the substrate (Scale bar is 25 µm.). Binary images are created (B) and the area of each individual vinculin adhesion site is quantified. The average vinculin adhesion area is significantly increased in cholesterol depleted cells compared to both control and cholesterol enriched cells (Using Student's T-test with  $p < 0.05$ ). No significant differences occur between control and cholesterol enriched cells. Error bars represent standard error. (N = 28, 26, and 25 cells for control, depleted and enriched, respectively).

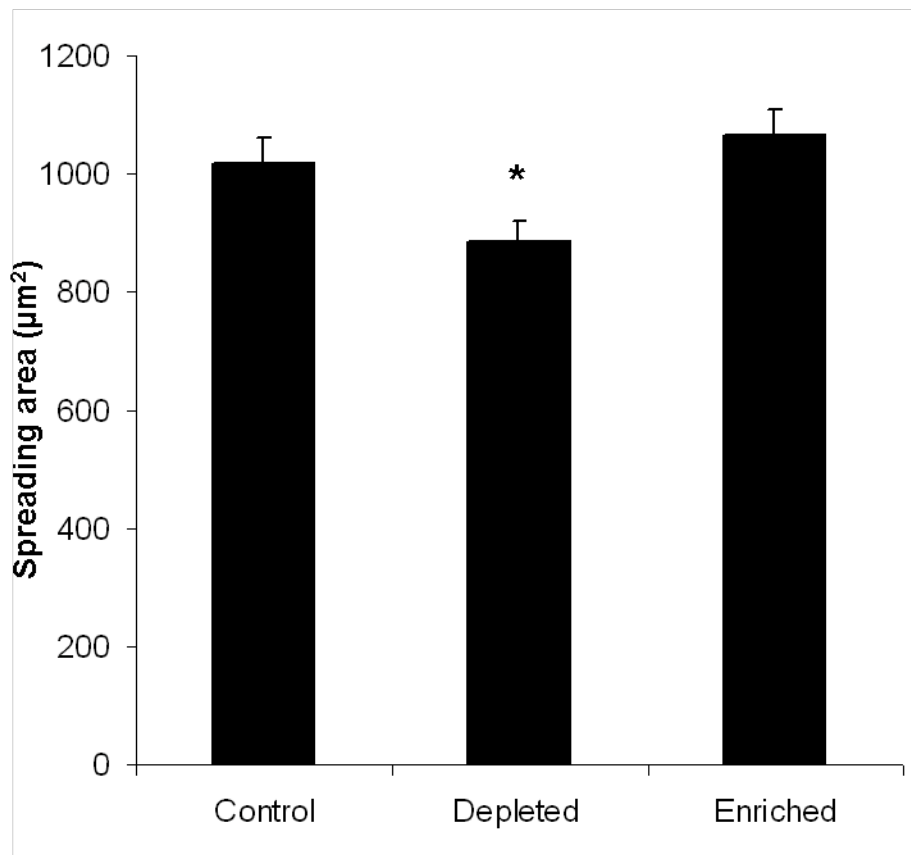


**Figure 5.3** Single cell spreading on fibronectin-coated glass substrates. Spread BAECs incubated for 1 hour with control solution (1:1 M $\beta$ CD:M $\beta$ CD-cholesterol mixture), M $\beta$ CD solution (depleted) or M $\beta$ CD saturated with cholesterol solution (enriched), and are observed using IRM. Cells depleted of cholesterol are significantly less spread compared to control cells, while no differences are observed between control and cholesterol-enriched cells. Asterisk denotes significant difference using Student's T-test with  $p < 0.05$ . Error bars represent standard error. (N = 36 – 44 cells per condition).

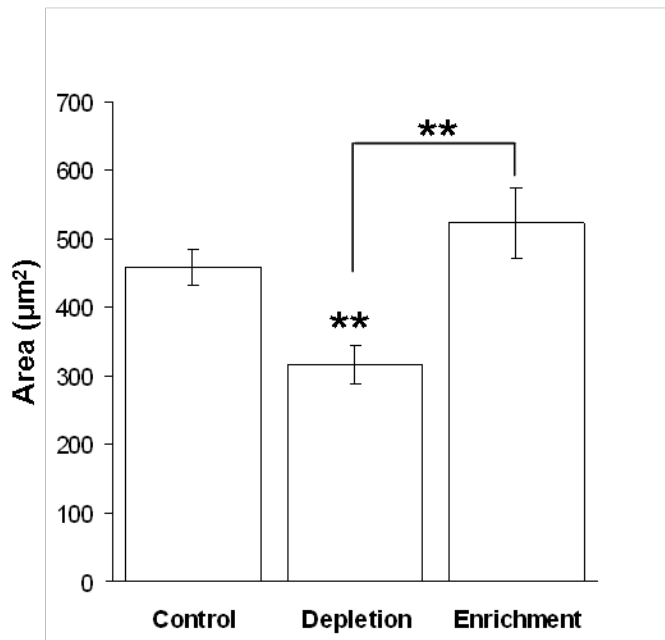


**Figure 5.4** Cells were plated onto fibronectin-coated glass bottom dishes containing control, cholesterol-depletion or cholesterol-enrichment solutions. Total spreading area was observed for untreated control cells (N=40), cholesterol depleted (N=60) and cholesterol enriched cells (N=53) after one hour of spreading using IRM. ImageJ was used to trace cell boundaries and quantify total spreading area. Error bars illustrate standard error with statistical significance reported at 95% confidence using a Student's T-test. Depleted cells are statistically less spread compared to control cells, while enriched cells are not statistically different.

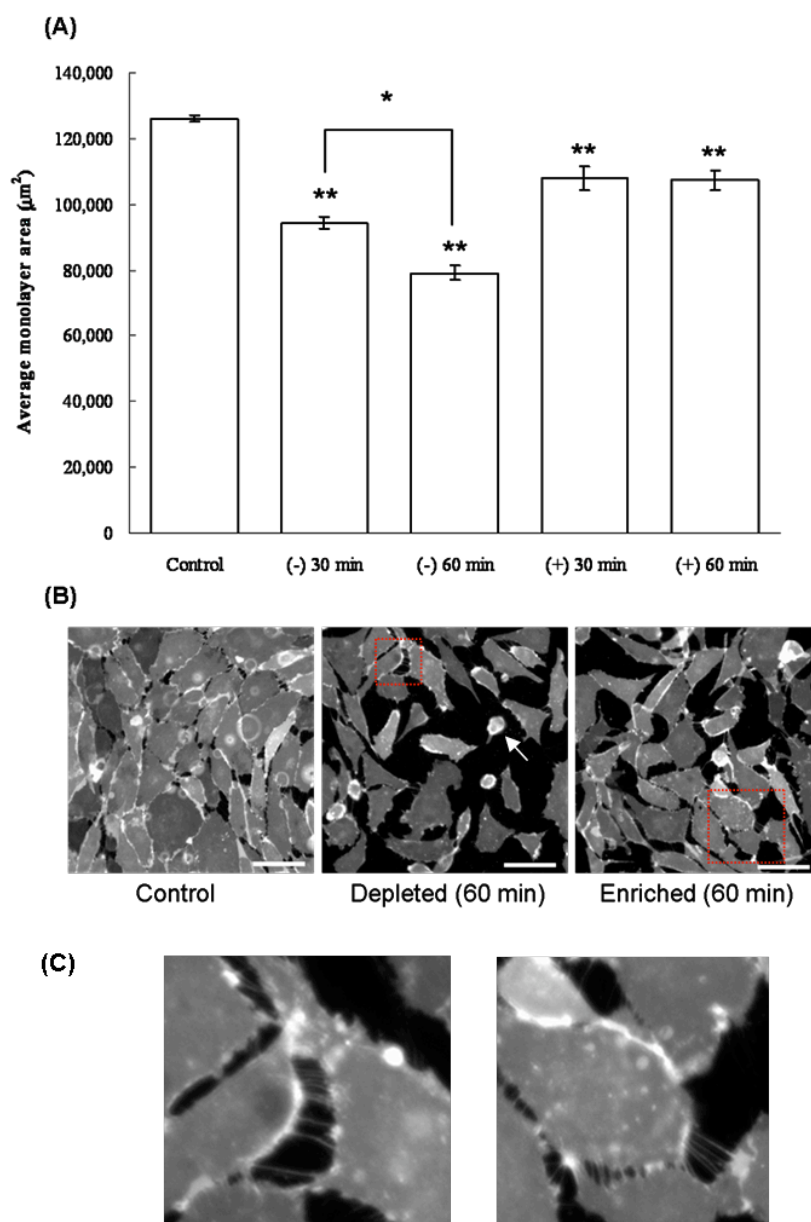


**Figure 5.5** Effect of cholesterol treatment on BAEC confluent monolayer plated on a fibronectin-coated glass for control, 30 minute, and 60 minute cholesterol-depleted (-) and cholesterol-enriched (+) cells (A). Monolayers were stained using the lipophilic probe DiIC<sub>16</sub>, and fixed after their respective treatment as described in the materials and methods section. The average area of monolayer coverage was quantified for 13-15 separate monolayer areas using ImageJ thresholding software. Error bars represent standard error obtained from the experimental data points. Statistical significances of all cholesterol treatment from control experiment are reported at 95% confidence level using Student's T-test. (Double asterisk =  $p < 0.01$ , single asterisk =  $p < 0.05$ ). Representative images are shown for control, as well as cholesterol-depleted and cholesterol-enriched cells after 60 minutes of treatment. Scale bar is 50 µm. (B) After 60 minutes of cholesterol depletion, some cells have rounded up and are almost entirely detached from the substrate (white arrow). In addition to cell-substrate detachment, cell-cell detachment is also observed and can be distinguished based on tethering observed between cell groups (C). Tethering of cholesterol depleted cells (C, left) appears similarly as that for cholesterol enriched cells (C, right), suggesting that both treatments result in a disruption of cell-cell adhesion.

## **6 Effects of substrate stiffness on cortical neuron outgrowth and differentiation<sup>†</sup>**

### ***6.1 Introduction***

Critical correlations between matrix stiffness and disease, including the stiffening of tissue in cancer tumors (224), changes in stiffness during the process of liver fibrosis (225), and the hardening of arteries in atherosclerosis (24, 226) have generated a vast amount of research aimed at understanding how these physical alterations affect cellular behavior and disease. Substrate stiffness has shown impacting effects on cell behavior, including migration and morphology for an assortment of cell types including epithelial (39), endothelial (41), vascular smooth muscle (227, 228), fibroblasts (39, 41), neutrophils (25) and stem cells (45, 66, 229). Understanding the way in which substrate stiffness affects these cellular responses may shed light onto how to treat and/or prevent diseases which involve changes in matrix compliance.

Recently, attempts aimed at understanding the effect of substrate stiffness on neuronal cells has been of significant interest, in particular, for understanding embryonic development and for designing tissue engineered materials for central nervous system injury and disease (47). To date, published studies have shown contrasting effects of substrate compliance on neurite outgrowth, with some reporting increases in the rate of neurite outgrowth (73) and branching (75) with decreased gel stiffness, while others report decreases in outgrowth and branching (67) with decreased compliance. In contrast, for cortical neurons grown in an astrocyte/neuron co-culture, there were no

---

<sup>†</sup> This section has been submitted as: Norman, LL and Aranda-Espinoza, H. 2010. Cortical neuron outgrowth is insensitive to substrate stiffness. (Under Review).

differences in axon length due to substrate compliance, however differences in actin assembly were observed (71). Numerous factors which likely influence these discrepancies include physical differences such as variations of substrate stiffness or dimensionality (i.e. 2D versus 3D), as well as differences in signaling which may arise from variations in ligand selection and concentration, as well as culture conditions. Also, the age and class of neurons, as well as time and length of observation, are variables that could account for differences in observed behaviors.

When evaluating substrate compliance, most studies select a range of stiffness that covers a general span of the native tissue. However, these “native” compliance ranges typically gathered from literature can vary between animal of origin, tissue type and preparation, as well as testing method (230). For example, the elastic modulus of swine brain has been reported between 260 - 490 Pa (231), while a more detailed evaluation of the rat brain revealed a heterogeneity among the hippocampus with stiffness ranging between 137 – 308 Pa using AFM and 662 Pa using macroscopic testing methods (128). This is in sharp contrast to other neuron-rich environments, such as the spinal cord, which has been measured at 89 kPa for human (232), yet dramatic variations in mechanical properties are observed among other vertebrates (233). In addition to differences among species, variation in the mechanical properties of animals also differs with age. For instance, Clarke *et al* (234) observe an increase in elastic modulus for adult rat compared to neonatal spinal cord, while Prange and Margulies (235) report an increase in the shear relaxation modulus of infant versus adult brain. This suggests the likelihood that stiffness changes during development are tissue dependent, and in the case of neuron-rich tissues, can also depend on the amount of gray versus white matter since

mechanical properties of these areas are known to differ as well (236). In addition to determining the stiffness of native tissue, the compliance of the cell itself has also been of recent interest. The elastic storage modulus of the growth cones of PC12s (neuron-like cells) was reported at approximately 300 Pa, which was the same stiffness at which growth cones were able to detectably deform compliant substrates (126), illustrating the importance of a cell's own compliance on mechanical impact. The viscoelastic properties of hippocampal and retinal neurons has also been evaluated, with reported elastic modulus ranging between 480 - 970 Pa for hippocampal pyramidal neurons, and 650 - 1590 Pa for retinal neurons (127). Collectively, the range of mechanical properties reported in the literature illustrate the importance of properly selecting the most appropriate stiffness range when attempting to recapitulate the native environment of the desired cell type.

Here, we determine the stiffness of the E17 fetal rat cortex using atomic force microscopy (AFM) and use the derived Young's modulus to determine an appropriate range of stiffness necessary to evaluate the effect of substrate mechanics on cortical neuron behavior. Using the well-characterized polyacrylamide (PA) gel system, we evaluate the relationship between substrate compliance and ligand coating to morphology, differentiation, and outgrowth behavior of primary cortical neurons. Interestingly, we see an insensitivity of cortical process length and migration to substrate stiffness. We observe differences in the tortuosity of process extension on laminin versus poly-d-lysine, as well as differences in the cell body migration; however these differences are independent of substrate compliance. Inhibition of myosin II also revealed effects independent of stiffness, yet dependent on extension behavior. Collectively, this work

suggests that cortical neurons are capable of differentiating and extending processes regardless of substrate stiffness. We suspect that at this stage of development, cortical neurons are not mechanotactic due to the homogeneity of their native environment and their unwarranted need to distinguish substrate compliance.

## ***6.2 Materials and methods***

### **6.2.1 Preparation of substrates**

Coverslip activation and polyacrylamide gel (PA) preparations were performed according to the methods of Wang and Pelham (237) and as described in Appendix A. Sulfosuccinimidyl-6-(4'-azido-2'-nitrophenyl-amino) hexanoate (sulfo-SANPAH, Pierce Chemicals, Rockford, IL) was used to crosslink either 100 $\mu$ g/ml poly-d-lysine (PDL; Sigma Aldrich) or 5 - 40 $\mu$ g/ml laminin (Sigma Aldrich) onto the gel surface. Solutions were allowed to incubate on the gel surface for 2 hours at room temperature (PDL) or 37°C (laminin), and were then rinsed three times with PBS.

### **6.2.2 Determination of Young's moduli using dynamic mechanical analysis**

Dynamic mechanical analysis (DMA) was performed using a Q-800 Dynamic Mechanical Analyzer (TA Instruments, New Castle, DE) and Q Series Explorer software to determine bulk mechanical properties of all PA gels except 3% Acrylamide, 0.06% Bisacrylamide and 3% Acrylamide, 0.04% Bisacrylamide. PA gels measuring 3 - 4mm in height were cyclically compressed (1 Hz) to a strain of 1%. Within this strain range, the linear elasticity of PA gels allows for the determination of the Young's modulus. The Young's moduli were determined as the slope of the linear stress-strain curves for each

gel. Our reported Young's moduli are similar to those reported by others for similar concentrations of bis and acrylamide (75).

### 6.2.3 Determination of Young's moduli using atomic force microscopy

Due to the inability to properly size and transfer the extremely soft gels into the Dynamic Mechanical Analyzer, the stiffness of the 3% Acrylamide, 0.06% Bisacrylamide and 3% Acrylamide, 0.04% Bisacrylamide gels was determined using atomic force microscopy (AFM; Agilent, Santa Clara, CA). AFM was performed using a silicon nitride cantilever (Novascan, Ames, IA) with a spherical glass SiO<sub>2</sub> probe of diameter 2.5µm. Using a glass surface, the deflection sensitivity was measured, while the program Thermal K (Molecular Imaging Corporation, San Diego, CA) was used to measure the spring constant. PA gels attached to glass coverslips were positioned under the AFM tip and force curves were captured for 4 - 8 regions. This was repeated for 3 - 5 individual gels. Force curve data was fit with a custom-written Matlab (The MathWorks) program, using the Hertz-Snedon model for a paraboloid indenter (238):

$$F_{paraboloid} = \frac{4}{3} \left( \frac{E}{1-\nu^2} \right) R^{1/2} \delta^{3/2}$$

Here,  $F_{paraboloid}$  is the load exerted by the paraboloid indenter and  $\nu$  is the Poisson's ratio. In this work  $\nu = 0.5$  for evaluation of PA gels (assuming gels are incompressible) and  $\nu = 0.45$  for measurements of cortical slices (assuming cells are nearly incompressible (239)).  $E$  is the Young's modulus,  $R$  is the radius of curvature of the indenter (i.e. the radius of the sphere; 1.25 µm), and  $\delta$  is the indenter to sample distance. To solve for the Young's modulus, a maximum indentation of 500nm was selected for fittings, since the Hertz-Snedon model does not hold at large indentations, yet at small indentations, the Young's

modulus depends significantly on the depth of indentation (240). Compared to the thickness of the gels (80 - 100 $\mu$ m), 500nm is adequately small, yet remains in the region where Young's modulus is independent of indentation depth. The data was fit from the point of contact (the point at which the derivative of the Force-distance curve became nonzero) to the maximum indentation. The Young's modulus was determined for each gel using the average of all force curves.

The abovementioned methods for determining the Young's modulus of PA gels using AFM was also used to determine the Young's modulus of cortex explants. Briefly, isolated fetal rat cortices were dissected and sliced into approximately 50 - 150  $\mu$ m long pieces. Cortex slices were plated onto a glass coverslip coated with 100 $\mu$ g/ml PDL and allowed to settle to the surface for approximately 45 minutes. Within this short time, attachment to the surface was minimal but precautions were taken to avoid movement of the cortices due to the AFM tip. The explants were positioned under the AFM tip as described above and force curves were taken for multiple locations for each explant. Multiple explants from 3 separate animals were analyzed and averaged.

#### **6.2.4 Characterization of surface-bound laminin**

After coating glass and gel surfaces with laminin as described above, 5% of bovine serum albumin (BSA; Sigma) in PBS was applied to each substrate for 3 hours. Substrates then incubated with a 1:40 dilution of primary anti-laminin (Sigma) in 3% BSA+PBS overnight at 4°C in a humidity chamber. Gels were gently rinsed with PBS and incubated with a 1:40 dilution of secondary anti-rabbit fluorescein-linked whole antibody (GE Healthcare; Piscataway, NJ) for 3 hours at 4°C in a humidity chamber. After incubation, substrates were washed twice with PBS. Fluorescence images were

taken of the substrates, with mean gray value levels quantified using ImageJ software (National Institutes of Health, Bethesda, MD). For control, PA gels without laminin-coating were immunostained as described above. Also, to verify that the amount of anti-laminin antibody was not at a saturated level, the initial amount of attached laminin was increased from 40 $\mu$ g/ml to 100 $\mu$ g/ml and a significant increase in the fluorescence intensity was observed (data not shown).

### **6.2.5 Cell Culture and experimental conditions**

Cortical neurons were isolated from E17 rat embryos (Taconic Farms, Hudson, NY) as described elsewhere (241), with a few modifications. All experiments were carried out in accordance to protocols approved under the Institutional Animal Care and Use Committee at the University of Maryland, College Park. All chemicals and media reagents were purchased from Invitrogen (Carlsbad, CA) unless otherwise specified. In brief, neurons were isolated from cortices and dissociated with 0.25% Trypsin with EDTA for 20 minutes at 37°C. Trypsin was inhibited with the addition of 1mg/ml soybean trypsin inhibitor and cells were centrifuged for 5 minutes. After centrifugation, cells were resuspended in neuronal culture medium and filtered through a 70 $\mu$ m cell strainer (Fischer Scientific). Neurons were grown in neuronal culture medium consisting of neurobasal medium, 2% B-27, 0.5mM L-Glutamine, 5% fetal bovine serum, and 1% penicillin/streptomycin. After 24 hours, media was removed and neurons were cultured in the abovementioned neuronal culture medium supplemented with 10ng/ml NGF, and 10 $\mu$ M FdU and 10 $\mu$ M Uridine (Sigma-Aldrich) to prevent cell division of non-neuronal cells. Mitotic inhibitors and NGF were removed after 30 hours, and cells were supplied with fresh neuronal culture medium. Dorsal root ganglion neurons were isolated from the

periphery of the E17 spinal cord and cultured with the same technique described above. Here we quantify only the outgrowth lengths of single cells which lack contact to neighboring cells. This ensures that outgrowth is not influenced by factors such as cell-cell adhesion molecules or membrane-associated guidance molecules, which have regulatory roles in axon guidance and selective fasciculation (242).

All snapshots and time lapse experiments were performed using an inverted microscope (Olympus American Inc, Center Valley, PA) and a 100W mercury lamp (Olympus). A CCD camera (Retiga SRV camera, QImaging, Surrey, BC Canada) was used for recording the images. All experiments were performed in a closed microscope chamber (Precision Plastics, Inc, Beltsville, MD) with culture conditions set at 37°C, 5% CO<sub>2</sub> and 50% humidity.

### **6.2.6 Inhibition of myosin II with blebbistatin**

Neurons were plated on laminin-coated substrates of varying stiffness. Extension behavior was observed for 30 minutes prior to the addition of blebbistatin (referred to as pretreatment). After 30 minutes, media was removed and supplemented with 25µM Blebbistatin (Sigma-Aldrich), a myosin II inhibitor. Cells were observed for an additional 30 minutes. Finally, cells were rinsed and supplied with fresh media and observed for an additional 30 minutes (referred to as washout). Time lapse sequences were quantified with ImageJ as described in the “Image Analysis” section below.

### **6.2.7 Antibodies and immunostaining**

Specific antibodies were selected to observe the appearance of neurofilaments and dendrites during cortical outgrowth. After the specified time, cells were fixed as

described elsewhere (243). Briefly, cells were initially rinsed with PHEM buffer. PHEM buffer was made using 60mM PIPES, 25mM HEPES, 10mM 0.5M EGTA, 2mM MgCl<sub>2</sub> and sterile water, and had a final pH of approximately 7.0. After two rinses, the cells were simultaneously fixed and the membrane was extracted using 0.25% glutaraldehyde and 0.1% Triton-X-100 in PHEM buffer (referred to as FEX solution). Cells were incubated in the FEX solution for 15 minutes at room temperature. Cells were rinsed again twice with PHEM buffer, and then incubated in 5% BSA for 25 minutes at room temperature. For the identification of neurites, primary rabbit anti-microtubule-associated protein-2 (MAP2) antibody (1:1000 dilution; Abcam, Cambridge, MA) was added to cells overnight. Cells were rinsed and then incubated in secondary anti-rabbit fluorescein-linked whole antibody (1:25 dilution, GE Healthcare) for 2 hours. All incubations were performed at 4°C in a humidity chamber. For axon specification, cells were also stained for the appearance of neurofilaments using primary mouse monoclonal (SMI31) antibody (1:1000 dilution; Abcam). Cells were incubated in the primary antibody overnight and were gently rinsed. Lastly, the secondary AlexaFluor594 goat anti-mouse antibody was added (1:200 dilution; Invitrogen) for 30 minutes. Cells were rinsed again and stored in PBS during observations.

### **6.2.8 Image analysis and statistics**

Neuronal process lengths and centers of mass (in x, y coordinates) were traced by hand using ImageJ analysis software. Analysis included only those neurites which did not contact other cells or processes and were greater than 5µm in length. All cortical experiments were repeated in triplicate, using different E17 rat embryos for each independent experiment. ImageJ analysis was also used to identify the length of the

process during extension and retraction observations, as well as blebbistatin experiments. To determine extension and retraction rates, single snapshots were taken approximately every 30 seconds for a total duration between 30 - 500 minutes, and the length of processes were measured by hand. The slope of individual extension and retraction periods were quantified and averaged for multiple cells. Data was quantified for statistical significance using either one-way ANOVA analysis or Student's T-test. One-way ANOVA analysis was used when evaluating statistical significance among multiple groups (i.e. comparisons among stiffness), while Student's T-test was used for determining statistical significance for single situations (i.e. comparisons of pretreatment spreading rate versus blebbistatin-treated spreading rates).

## **6.3 Results**

### **6.3.1 Identification of cortex stiffness using atomic force microscopy**

The majority of biological tissues and organs are soft viscoelastic materials which exhibit elastic moduli ranging on the order of  $10^2$  Pa to  $10^5$  Pa (230). In order to thoroughly evaluate the effect of substrate mechanics on cortical neuron outgrowth we first determined the native stiffness of the fetal rat cortex using atomic force microscopy (AFM). Force curve measurements were taken for multiple locations for 7 separate cortex explants (see Materials and Methods section for determination of Young's modulus). The average Young's modulus for fetal rat cortex was determined as  $305 \pm 25$  Pa (S.E.M.). This stiffness is in the same range (263-491 Pa) of that for the swine brain predicted theoretically and supported using an *in vivo* indentation method (231). Quantifying the Young's modulus of the native fetal rat cortex was critical in determining

the range of polyacrylamide (PA) gel stiffness necessary to ensure observations both below and above the native environment rigidity. Thus, we decided to make gels with the range of stiffness 260 Pa – 13 kPa.

### **6.3.2 Specification of substrate ligand concentration and Young's modulus**

Preparation of PA gels (see Materials and Methods) was performed with slight adaptations of the method described by Pelham and Wang (237), and either a dynamic mechanical analyzer or AFM was used to determine the mechanical properties of the gels. Dynamic mechanical analysis (DMA) and AFM verified that increasing concentrations of bis-acrylamide (and acrylamide) yielded PA gels with increasing Young's moduli. DMA resulted in gels with Young's modulus values of  $13.15 \pm 2.0$  kPa (8% acrylamide, 0.2% bis, as previously reported (25)),  $986 \pm 140$  Pa (3% acrylamide, 0.2% bis), and  $867 \pm 180$  Pa (3% acrylamide, 0.1% bis). AFM resulted in gels with Young's modulus values of  $422 \pm 6$  Pa (3% acrylamide, 0.06% bis) and  $260 \pm 2$  Pa (3% acrylamide, 0.04% bis).

To ensure that observed neurite outgrowth dynamics and behavior result from substrate stiffness and not the concentration of adhesive ligand, the concentration of laminin was adjusted for glass coated substrates such that the differences between the gels and glass were not significant. To do so, substrates were incubated with 40 $\mu$ g/ml of laminin and anti-laminin antibodies were used to identify the intensity of laminin present on the substrate surface (see Materials and Methods section for more details). Epifluorescence snapshots were captured for 5 - 12 locations on each gel and the mean gray value was determined using ImageJ. The arbitrary fluorescence intensity values were similar for all gel substrates, and only glass illustrated a significantly increased

concentration of laminin (Figure 6.1A). Laminin titrations were created to determine the necessary amount of protein required on the glass surface to compliment the concentration present on the gel surfaces (Figure 6.1B). Therefore, to reach similar protein content, 5 $\mu$ g/ml laminin was added to glass substrates, while 40 $\mu$ g/ml was added to PA gels (Figure 6.1B). Typically, gels of similar acrylamide concentration do not vary in the amount of present surface ligand (25, 39, 244, 245), therefore it was not unexpected that all gels of 3% acrylamide (and varying percentages of bisacrylamide) were similar in intensity. It is also not entirely unusual that we did not see a significant increase in the amount of ligand present on the 8% acrylamide, 0.2% bisacrylamide, since others have shown similar ligand concentrations between polyacrylamide gels with a 6% difference in acrylamide percentages (67). Correcting for the concentration of ligand present on the surface ensures that differences in cellular behavior are due to mechanical differences and not the concentration of surface ligand. Although we were unable to qualitatively determine the amount of PDL on the substrates due to a lack of comparable fluorescent tags, we suspect that gels will have similar expression on their surface after coating, as seen with laminin. We also coated glass coverslips with varying concentration of PDL, 10, 50 or 100 $\mu$ g/ml PDL, and observed no significant differences in the length of the longest process (data not shown).

### **6.3.3 Axonal differentiation of cortical neurons is insensitive to substrate stiffness**

Although a significant amount of work has been recently performed on the effect of substrate compliance on neurite outgrowth for spinal cord (75), DRG (72, 73), hippocampal (246) and PC12 cells (67), less work exists on the mechanosensitive properties of cortical neurons. Recently, Georges *et al* (71) has reported similar lengths

in process outgrowth for cortical neurons plated onto substrates of varying stiffness; however, this study used neuron and glial co-cultures which were observed after 6 days. After this length of time, dissociated cortices were abundant on both soft and hard substrates and were densely packed with multiple processes connecting (71). It is possible that this cell-cell contact and synapse formation can alter the behavior of neurons, since outgrowth can be influenced by cell-cell adhesion molecules and membrane-associated guidance molecules (242, 247), and spontaneous synapse connections and current can be detected as early as 4 days in culture (248). Here we hypothesized that if cortical neurons were sensitive to substrate stiffness then the differences in outgrowth behavior would most likely be observed during the first 72 hours or even during bursts of growth and retraction, when axons differentiate. To investigate the effects of substrate stiffness on cortical neuron differentiation, cortices were isolated, dissociated and plated onto laminin or PDL substrates and cultured for 72 hours.

To qualitatively determine when axons are specified, cells were fixed at 6, 24, 48, and 72 hours and were then stained with MAP2 to stain the microtubule associated proteins in neurites, and SMI31 to stain the neurofilaments (NF) present only in the axon of each cell (Figure 6.2). Among stiffness and protein coating, we notice similar staining presence during the course of the 72 hours observed. First, after 6 hours small neurites are present, as identified in green with the MAP2 antibody. No SMI31 (red) staining is present in the processes, illustrating that no NF are present in any of the processes, and thus no neurites have differentiated into axons. After 24 hours, however, some cells stain positive for neurofilaments, although the stain is typically weak in expression and is not

present in the majority of cells. The most noticeable NF staining occurs at the 48 hour time point, where neurites are clearly stained green and one process is positively stained red for the presence of NF. After 72hrs, this becomes even more noticeable. Overall, this suggests that cortical neurons begin differentiating after the addition of NGF (24 - 48 hours) and the most apparent NF positive staining occurs at 72 hours when the axon is clearly specified. It is not surprising that the time at which axons begin to differentiate corresponds to the time at which NGF is added to the media, since NGF encourages differentiation of many cell types (69, 249) and is required for nerve growth during development (250). However, what is surprising is that differentiation occurs regardless of substrate stiffness.

To quantitatively confirm these observations, we used the three-stage process of differentiation originally described by Dottie *et al* (53) and also used by others (246). Neurons were classified as Stage 1 when there was an absence of neurites. For us, the majority of Stage 1 neurons were observed around 6 hours of plating. Stage 2 was used to classify neurons where the neurites were similar in length. Typically, these cells did not stain for SMI31. Lastly, neurons were classified as Stage 3 when a significantly long axon emerged and stained positive for SMI31, indicating that this process is indeed an axon. The majority of Stage 3 neurons were observed between 48 - 72 hours. The percentage of cells in Stage 3 from 24 – 72 hours is displayed in Figure 6.2 for laminin (Figure 6.2C) and PDL-coated (Figure 6.2D) substrates. For laminin, differentiation occurred for 40– 50% of cells at 24 hours, 50–60% of cells at 48 hours and 70–80% of cells at 72 hours. Similarly, for PDL, differentiation occurred for 40–50% of cells at 24 hours, 60–70% of cells at 48 hours and 75 – 85% of cells at 72 hours. Overall, the

percentage of neurons classified as Stage 3 increased during this time period, however, unlike hippocampal neurons where more Stage 3 neurons are observed on soft substrates (246), for cortical neurons we did not observe a trend among stiffness for either protein coating. This illustrates that cortical neuron differentiation is insensitive to matrix compliance and protein coating.

#### **6.3.4 Cortical outgrowth is insensitive to substrate stiffness**

The length of the longest process during differentiation has long been used as a method to distinguish axons versus dendrites and to classify cells as Stage 3 neurons (50). Although we illustrate above that axons differentiate similarly regardless of substrate compliance, it remains unknown whether the axons also extend to similar lengths during this differentiation process. To quantify the length of axons during extension, snapshots were captured at 6, 24, 48 and 72 hrs post plating and images were analyzed for the number of neurites and individual neurite lengths. The average length of the longest process for each neuron is displayed in Figure 6.3 for both laminin and PDL coated substrates. Interestingly, after 72 hours, we did not see statistically significant substrate-dependent differences in the length of the longest process for either protein coating (using one-way ANOVA analysis,  $p > 0.01$ ). This data shows that cortical neurons are capable of extending processes of similar lengths regardless of the substrate compliance for both integrin-mediated (laminin-coating) and non-integrin-mediated adhesion (PDL coating). When comparing the length of the longest process to the second longest process, this ratio was also similar for all stiffness. The longest process was on average 3–5 times the length of the second longest process at 48 and 72 hours for both laminin and PDL substrates (data not shown). This emphasizes that the longest process is many times

longer than the other neurites, which has been also used as a method to classify neurons as Stage 3 and to distinguish an axon versus dendrite, and is consistent with our differentiation observations (50). From this, one can also conclude that at 72 hours, the longest process, which is typically 90–120  $\mu\text{m}$  in length is indeed the axon, since the majority of cells at this time point (approximately 80%, see Figure 6.2) have differentiated. In addition to the longest process per cell, substrate stiffness did not affect the average number of processes per cell (Figure 6.3B and E), unlike others (67) who see increased neurites for PC12s plated on stiffer substrates. Also, we observe no substrate affects on the average length of all processes per cell (Figure 6.3C and 6 F) after 72 hours of culture (using one-way ANOVA analysis,  $p > 0.01$ ).

Although Figure 6.3 may suggest that neurite and axon extension is a linear phenomenon, it is known that this is not the case (251, 252). Rather than extending a continuous process slowly over the course of 72 hours, axons actually exhibit periods of extension, retraction and stalling. One explanation for the lack of difference in process lengths at the observed time points is the possibility that neurons extend processes at different rates on different stiffnesses. For example, it may be possible that differences in extension and retraction rates are occurring; however this dynamics is not observed when single snapshots are recorded at each time point. To further evaluate this possibility, we observed individual neurites during outgrowth using time lapse microscopy. Snapshots of individual neurites were taken every 30 seconds for a period of observation ranging from 30 - 500 minutes for soft (240 Pa and 870 Pa) intermediate (13 kPa) and stiff (glass) substrates. Neurite lengths were traced using ImageJ (see Materials and Methods) and the rate of individual periods of extension and retraction were quantified (Figure 6.4).

Interestingly, for laminin-coated substrates, there were no significant differences (one-way ANOVA analysis,  $p > 0.01$ ) in the rate of extension on glass ( $0.92 \pm 0.07$   $\mu\text{m}/\text{min}$ ;  $N=59$ ), 13 kPa ( $0.83 \pm 0.09$   $\mu\text{m}/\text{min}$ ,  $N=67$ ), 870 Pa ( $0.87 \pm 0.06$   $\mu\text{m}/\text{min}$ ,  $N=61$ ), or 240 Pa ( $1.05 \pm 0.1$ ,  $N = 43$ ) substrates. The rate of extension on PDL-coated substrates was significantly reduced on all substrates compared to laminin, similar in behavior to retinal explants (253). However, as seen with laminin substrates, there were no significant differences among glass ( $0.56 \pm 0.07$   $\mu\text{m}/\text{min}$ ;  $N=38$ ), 13 kPa ( $0.50 \pm 0.04$   $\mu\text{m}/\text{min}$ ,  $N=58$ ), 870 Pa ( $0.64 \pm 0.06$   $\mu\text{m}/\text{min}$ ,  $N=45$ ), or 240 Pa ( $0.73 \pm 0.12$   $\mu\text{m}/\text{min}$ ,  $N=22$ ) PDL substrates. There were also no significant differences (one-way ANOVA analysis,  $p > 0.01$ ) in the rate of retraction on glass ( $-1.64 \pm 0.32$   $\mu\text{m}/\text{min}$ ;  $N=23$ ), 13 kPa ( $-1.39 \pm 0.47$   $\mu\text{m}/\text{min}$ ,  $N=22$ ), 870 Pa ( $-1.70 \pm 0.25$   $\mu\text{m}/\text{min}$ ,  $N=22$ ), or 240 Pa ( $-1.30 \pm 0.18$ ,  $N = 19$ ) laminin substrates. As with extension, the rate of retraction on PDL-coated substrates was also statistically reduced on all substrates compared to laminin. Yet, again as seen with laminin substrates, there were no significant differences among retraction dynamics on glass ( $-0.93 \pm 0.26$   $\mu\text{m}/\text{min}$ ;  $N=7$ ), 13 kPa ( $-0.59 \pm 0.12$   $\mu\text{m}/\text{min}$ ,  $N=14$ ), 870 Pa ( $-1.08 \pm 0.22$   $\mu\text{m}/\text{min}$ ,  $N=15$ ), or 240 Pa ( $-0.55 \pm 0.14$   $\mu\text{m}/\text{min}$ ,  $N=12$ ) PDL substrates.

To further verify that the PA gel system which we are using in this study is appropriate for mechanosensitive neurons, we observed the outgrowth behavior of dorsal root ganglion (DRG) neurons. Because increased neurite outgrowth on softer substrates has been illustrated for DRGs in 3D gels (72, 73), we suspected that we should also see a significant increase in the extension of DRG processes when plated onto PA gels of varying stiffness. DRGs were isolated from E17 rat pups, dissociated, and plated onto PDL coated substrates. Cells were plated onto stiff (glass), intermediate (13 kPa) and

soft (870 Pa) substrates and snapshots were captured after 24, 48 and 72 hours of culture (Figure 6.5). Based on previous investigations of DRG outgrowth which report differences with stiffness (72, 73), we suspect that this selected stiffness range is appropriate to observe substrate-dependent affects and is also physiologically relevant based on measurements of spinal cord and brain (128, 232, 235, 254). This stiffness range also allowed us to compare mechanotactic behavior of DRG versus cortical neurons. Processes were observed on all substrates, however, the longest processes were present on the softest (870 Pa) gel. Process extension on the softest gel was statistically increased compared to both the stiff and intermediate stiffnesses at all observed time points. This data illustrates that similarly to that reported with 3D gels (72, 73), DRG neurons retain their mechanosensitive properties on 2D PA gels.

### **6.3.5 Process extension is more directed on laminin-coated substrates**

Although the average length of the longest process was comparable between laminin and PDL-coated substrates after 72hrs (Figure 6.3), differences in extension morphology were apparent (Figure 6.2A and B and Figure 6.6B). The differences in process extension were most noticeable at 72 hours, when the longest process had extended to approximately 90 - 120  $\mu\text{m}$  in length. To quantify the differences in extension, we defined a persistence index (or tortuosity) for each condition calculated by measuring the contour length,  $L_c$  and the “end-to-end” outgrowth length,  $L_s$ . The schematic shown in Figure 6.6A illustrates these two parameters. When the ratio of  $L_c/L_s = 1$ , the process is perfectly straight. Increased tortuosity is represented by an increase in  $L_c/L_s$ . For all compliances, cells on PDL coated substrates had a significantly increased persistence index, illustrating that they were more meandering during outgrowth

compared to laminin-coated substrates (Figure 6.6C). Also, when plated at a higher concentration, aggregated cells extended differently on laminin versus PDL. On PDL, neurons aggregated into a more interwoven pattern, with processes extending in an undirected manner (data not show), similar to that described by Lemmon *et al* (253). When neurons were plated at a higher concentration on laminin, aggregation was still observed but processes were more aligned on top of each other and extended more directly from aggregated groups. Meandering processes may serve as a method for the axon to find synaptic targets that it wouldn't necessarily encounter if extending with a straight trajectory and has therefore been suggested as a possible mechanisms to search for specific targets (255). Extension and retraction behavior as well as adhesion likely contribute to this increase in tortuosity on PDL substrates.

In addition to the observed difference in axon extension morphology, the amount of cell body movement during the initial stages of process outgrowth was also noticeably different between PDL and laminin-coated substrates (See supplementary movies S1 and S2). Cells were observed before a long process had differentiated, since this was the period where the most displacement was noticed. To quantify cell body displacements, the center of mass of the cell body (in x, y coordinates) was tracked for each frame of the time lapse sequence (30 min sequence with 1 frame per 30 sec) using ImageJ tracing tools. Mean squared displacements (MSD) were calculated for 10-15 cells with the averages plotted in Figure 6.7. Overall, cell-body displacement was independent of stiffness, although neurons cultured on laminin-coated substrates exhibited statistically larger cell body displacements during axon extension compared to those cultured on PDL. Note, however, that is difficult to directly compare the two different protein

coatings because laminin is an integrin-based adhesion and PDL involves electrostatic (or integrin independent) interactions. The decrease in cell body movement is likely caused by an increase in cell-substrate adhesion, which has been reported for polylysine (256). The decrease in extension rate for processes extending on PDL versus laminin-coated substrates also supports this increase in adhesiveness (Figure 6.4).

It is important to note that although neurons plated onto both laminin and PDL exhibit some degree of cell body displacement, the magnitude of these displacements may contribute to the measurements of the longest process between 6 – 72 hours (Figure 6.3A and D). Since the cell body displaces more on laminin substrates, it is possible that this could cause axons to be shorter in length, since if the cell body moves in the direction of the growth cone, this would reduce the length between cell body and the tip of the longest process. This may be a reason why process extension length on laminin-coated substrates is similar to PDL substrates during the first 72 hours of culture (Figure 6.3A and D). Although it is impossible to distinguish from snapshots whether the cell body has recently displaced, using time lapse microscopy we were able to determine these precise events and ensured that they did not contribute to the retraction or extension speeds reported in Figure 6.4. Extension was considered only if the growth cone itself was moving forward, while retraction was considered only if the growth cone moved towards the cell body.

### **6.3.6 Myosin II inhibition is independent of substrate stiffness**

Myosin II (MII) is a motor protein that, in combination with actin, can generate cellular contractile forces and is required for growth cone motility (257). Recent focus on the role of MII (as well as other isoforms) has shown implications of myosin in both

the extension and retraction phases of axon development. For example, down-regulation of MIIA and MIIB has illustrated an inhibition of neurite extension in N2A cells (258), and the protrusion of filopodia (an essential step in growth cone advancement (259)) requires myosin activity (257). Myosins are also implicated in axon retraction. For instance, axon retraction was prevented by the inhibition of MII for sever-induced axons (260), as well as for established axons *in vivo* following negative regulation of RhoA or ROCK (261). More recently, it has been suggested that MII functions in a substratum-dependent manner (262). Although Ketschek *et al* (262) report differences in myosin inhibition for cells extending on laminin versus lysine, the role of MII during axon extension on substrates of varying compliance remains unknown. Because rigidity sensing has been shown to be integrin-dependent (246, 263), we evaluate how MII inhibition affects both the extension phase as well as the stalled phase of axon outgrowth on laminin-coated surfaces of varying stiffness. We hypothesized that if cortical neuron extension is independent of substrate stiffness, then the inhibition of MII should affect axons similarly regardless of substrate compliance.

To test the effects of MII inhibition on axon extension, time lapse sequences were taken for individual processes for 30 minutes prior to treatment (pretreatment). After 30 minutes, 25  $\mu$ M blebbistatin was added and processes were observed for an additional 30 minutes. Lastly, the blebbistatin solution was removed and fresh media was added while extension was observed for an additional 30 minutes (washout). The length of extension over the course of this 90 minute period was quantified using ImageJ (see Materials and Methods for a detailed explanation). Cells were classified as either “extending” or “stalled” based on the rate of the first 30 minutes of observation, prior to the addition of

blebbistatin. “Extending processes” were those which were increasing in length with a speed  $\geq 0.2 \mu\text{m}/\text{min}$ , while those considered “stalled processes” exhibited little or no extension with rates between  $-0.15 - 0.2 \mu\text{m}/\text{min}$ . The average rate of extension during pretreatment as well as blebbistatin treatment is displayed in Figure 6.8. The rates of extension during the washout period were comparable to that of the pretreatment rates (data not shown). MII inhibition caused no significant differences in the extension rate of previously extending axons for all laminin-coated substrates. Although the extension rate during blebbistatin treatment on glass appears larger (Figure 6.8), there were no significant differences between the speeds during blebbistatin treatment among laminin-coated substrates of varying stiffness. Unlike Ketschek *et al* (262), we do not see a decrease in the rate of extension during blebbistatin treatment of laminin-coated glass. These discrepancies could be due to differences in laminin concentration ( $25\mu\text{g}/\text{mL}$  (262) versus  $5 \mu\text{g}/\text{mL}$ ), type of neurons (E7 chicken DRGs versus cortical neurons), and dissociated single cells versus cultured explants (262). We also note that the pretreatment rate for laminin is slightly reduced compared to that reported in Figure 6.4, however these rates are not significantly different and remain within one standard deviation from the mean. Most interestingly, we report statistically significant increases in the speed of extension when MII is inhibited during a stalled period of axon development regardless of substrate stiffness (Figure 6.8B). As seen with axons which were initially extending, there are no significant differences between the extension rates during blebbistatin treatment for laminin, illustrating again that this is not dependent on substrate stiffness. Collectively, this data illustrates that MII does not appear to be regulated

differently on different stiffnesses, and also suggests MII inhibition as a method to encourage axon outgrowth when processes were previously in a stalled period of growth.

## **6.4 Conclusions**

Dramatic changes in the mechanical environment of various organs and tissues have been associated with both disease and injury. With respect to the nervous system, a focus on the mechanical changes occurring following spinal cord injury and traumatic brain injury has been of much current interest (47). Recent work has illustrated that the hippocampus is a mechanically heterogeneous environment, possessing regions of varying elastic moduli (128) and differences in the viscoelastic properties of neuron versus non-neuronal cell populations (127). Due to the differences in the mechanical environment of the hippocampus, it is not surprising that isolated hippocampal neurons are mechanosensitive, growing preferentially on softer substrates (246). Here, we show that, unlike DRG (Figure 6.5) and hippocampal neurons (246), cortical neurons appear to be insensitive to the substrate stiffness. We report not only similar times of differentiation (Figure 6.2), but also similar behavior in process length and number (Figure 6.3), extension and retraction dynamics (Figure 6.4), and myosin activity (Figure 6.8). The ability of cortical neurons to extend long processes on substrates with varying stiffness is not entirely surprising, as others have briefly mentioned this phenomenon (71), although they do not consider extension and retraction behavior.

One might initially suspect that the length of processes on PDL-coated substrates should be reduced compared to laminin, since the individual extension rate was significantly increased on laminin-coated substrates (Figure 6.4). However, although axon extension on laminin substrates is increased, the retraction rate is also significantly

larger than on PDL substrates. Therefore, extension on PDL substrates is occurring more slowly, while retraction is less dramatic and possibly less frequent. In addition, for individual extension and retraction events, the average duration of extension was longer for PDL substrates, while the average duration of retraction was shorter. Characteristic examples of axon extension on glass coated with laminin and PDL are shown in Figure 6.9A. Note that the cells are captured at a similar time in outgrowth (between 49 - 53 hours of culture) and begin with similar process lengths (the laminin data is shifted up 25 $\mu$ m for clarity). The difference in outgrowth dynamics is very clear, with laminin-coated substrates illustrating many more periods of rapid retraction and extension. In certain cases, rapid retraction may cause sharp movement of the cell body, displacing it towards the growth cone. Again, these events are not included in average retraction rates; however, they are present more frequently on laminin-coated substrates and do contribute to the overall effect on length. Alternatively, the growth cone also exhibits rapid retraction events, such as that marked with a cross in Figure 6.9A, and illustrated in Figure 6.9B. This decrease of approximately 30 $\mu$ m occurs over the course of 2 minutes and is interestingly comparable to the rate of microtubule depolymerization, which occurs between 20-30  $\mu$ m/min (264). Other retraction events (such as that marked with an asterisk in Figure 6.9A) occur more slowly, with an average rate of approximately -1.64  $\mu$ m/min for laminin-coated glass, and are likely caused by a combination of acto-myosin contraction, traction stresses and cell tension, which we further address below.

Initially, it was surprising that neurons plated on different compliances extend and retract with similar rates, considering Franze *et al* (126) have recently illustrated that neurons retract when stress applied to the growth cones of cortical neurons is increased.

In their work, Franze *et al* applied a mechanical stress to the tip of PC12 growth cones and reported a retraction threshold ( $274 \pm 41$  pN/ $\mu\text{m}^2$ ). Below this level growth cone protrusion is not disturbed, yet above this level growth cones retract. From this, we suspected that we may see differences in the retraction behavior for cells plated onto our softest gels (260 Pa) compared to more stiff substrates. However, as shown in Figure 6.4, we observe similar retraction (and extension) behavior regardless of stiffness. Even more, during the stalling periods MII forces dominate the dynamics of the growth cone, if there were any differences due to stiffness we should have seen different outgrowth upon MII inhibition, however we observe the same rate of growth in all stiffness tested. This leads us to believe that, because cortical neurons appear to have all the basic machinery necessary to sense substrate stiffness (including myosin, actin, and cell-substrate adhesions), we suspect that cortical neurons may lack or down-regulate some form of rigidity-sensing mechanisms such as receptor-like protein tyrosine phosphatase  $\alpha$  (RPTP $\alpha$ ), which is required for mechanosensing in hippocampal neurons (246), or potentially an unidentified mechanotactic protein.

Various cell types subjected to mechanical stimuli *in vivo*, including epithelial (39), neutrophils (25), endothelial (41), fibroblasts (39, 41) and stem cells (45, 66, 229) have all been shown to respond to the mechanical properties of their environment whether in changes in morphology, migration or differentiation. In the brain, however, cortical neurons do not generally bear significant load and are secluded to their environment due to their discrete localization. We suspect that the insensitivity to substrate stiffness which we report here may arise due to the native properties of the fetal rat cortex during the selected stage of development. During corticogenesis, neurons

exhibit radial migration, starting from the ventricular zone and ending up in one of the six layers of the cortex (265). The development of these cortical layers occurs throughout the last weeks of gestation for the fetal rat. In particular, layer VI, the deepest and innermost neuron layer, is generated between E13 - E16, while layer II/III neurons are not produced until the very end of the gestation period, around E18 – E21 (241). The higher the cortical layer, the closer to the ventricular zone the neurons are, illustrating that the neurons are reaching final cortical development at the end of gestation when layers II and III are formed. Like others, we isolate cortical neurons from E17 fetal rats due to the maximal proliferation of neurons at this date (241). It is possible that the migration of these neurons *in vivo* is independent of substrate stiffness, since the signaling required to order cortical neurons into distinct layers appears more chemical in nature and is reliant on the presence of the glycoprotein Reelin (266). Due to the very soft nature of the cortex during this stage of development, we were not able to isolate separate layers of the cortex in order to determine the stiffness of each cortical layer; however, as described above, we did probe various random slices of the cortex and found a similar stiffness ( $E = 305 \pm 25$  Pa) for each tested sample. Collectively, the data we present here suggest that, during this early stage of development, there are no discernible differences in stiffness in the cortex. This mechanical homogeneity of the cortex may contribute to the inability of cortical neurons to sense stiffness at this stage of development. It would be interesting to determine whether this homogeneity is retained throughout the rest of fetal and neonatal development.

An additionally valuable result from this work is the identification that myosin II inhibition during a previously stalled stage of axon outgrowth encourages axon extension

for all laminin-coated substrates (Figure 6.8). The effects on outgrowth which we observe following MII inhibition can be explained by the forces involved in axon outgrowth. A simplified schematic of the cytoskeletal components and forces involved in extension/retraction events are illustrated in Figure 6.10. Axon outgrowth requires a driving polymerization force at the tip of the growth cone  $F_p$ , which is balanced by ECM adhesion, using integrins. These integrin based adhesions have been associated with the rigidity sensing of both neuronal (246) and non-neuronal cell types (263) and create traction force coupled with the substrate,  $F_s$ . An additional force,  $F_m$ , present during axon extension arises from acto-myosin contractility. Acto-myosin forces arise from the contractility of myosin subunits on actin bundles, and the “pulling” of these acto-myosin complexes contribute to forward movement (267). Overall, an appropriate balance between F-actin turnover and acto-myosin contractility is necessary for proper axonal outgrowth dynamics (243, 257). Periods of axon extension, retraction and stalling can all be explained based on the balance of these forces. When axons are extending,  $F_p > F_s + F_m$ , and alternatively, when axons are retracting, the contractile forces are greater than the force of polymerization, thus  $F_p < F_s + F_m$ . Lastly, if axon outgrowth is stalled, there is a balance of forces such that  $F_p = F_s + F_m$ . During MII inhibition, we notice that for all substrates, axons which were initially extending continue to extend with similar outgrowth rates, meaning  $F_p > F_s$ . On the other hand, when axons are stalled and MII is inhibited, we see rapid extension because the polymerization force greatly exceeds that of the integrin and substrate-mediate traction forces, such that  $F_p \gg F_s$ . Microtubule engorgement has been observed on laminin substrates; however the rate of axon extension was not increased (262), which the authors attribute to decreased substratum

attachment. In our system, it is possible that the rapid engorgement of microtubules into the growth cone triggers enough force in the leading growth cone to encourage rapid extension. For cells which were already extending, this engorgement force may not be as dramatic, since the polymerization force at the leading edge of the growth cone was already contributing to axon extension, therefore the growth rate continues unaffected. These results emphasize the critical balance in forces necessary for proper outgrowth dynamics and also suggest the ability to encourage axon extension from a previously stationary state. These results have important implications for various therapeutic techniques and tissue engineering applications, such as the encouragement of axon outgrowth across engineering platforms in the spinal cord (47).

This work demonstrates that cortical neurons differentiate and extend processes similar in length and number on substrates of varying stiffness. Also, cortical extension and retraction dynamics, as well as myosin activity, are all independent of substrate stiffness. We observe only morphological differences between laminin versus PDL-coated substrates; however, we do not observe any substrate dependent effects. Collectively, these results demonstrate that, unlike DRG (Figure 6.5 and (72, 73)) and hippocampal (246) neurons, cortical neuron behavior is not affected by substrate compliance. We hypothesize that this mechano-insensitivity results from the homogenous environment of the developing cortex. Ultimately, the results presented here emphasize that mechanotactic behavior is cell type specific, and the native environment of the cell likely dictates its response to modifications in mechanical properties.

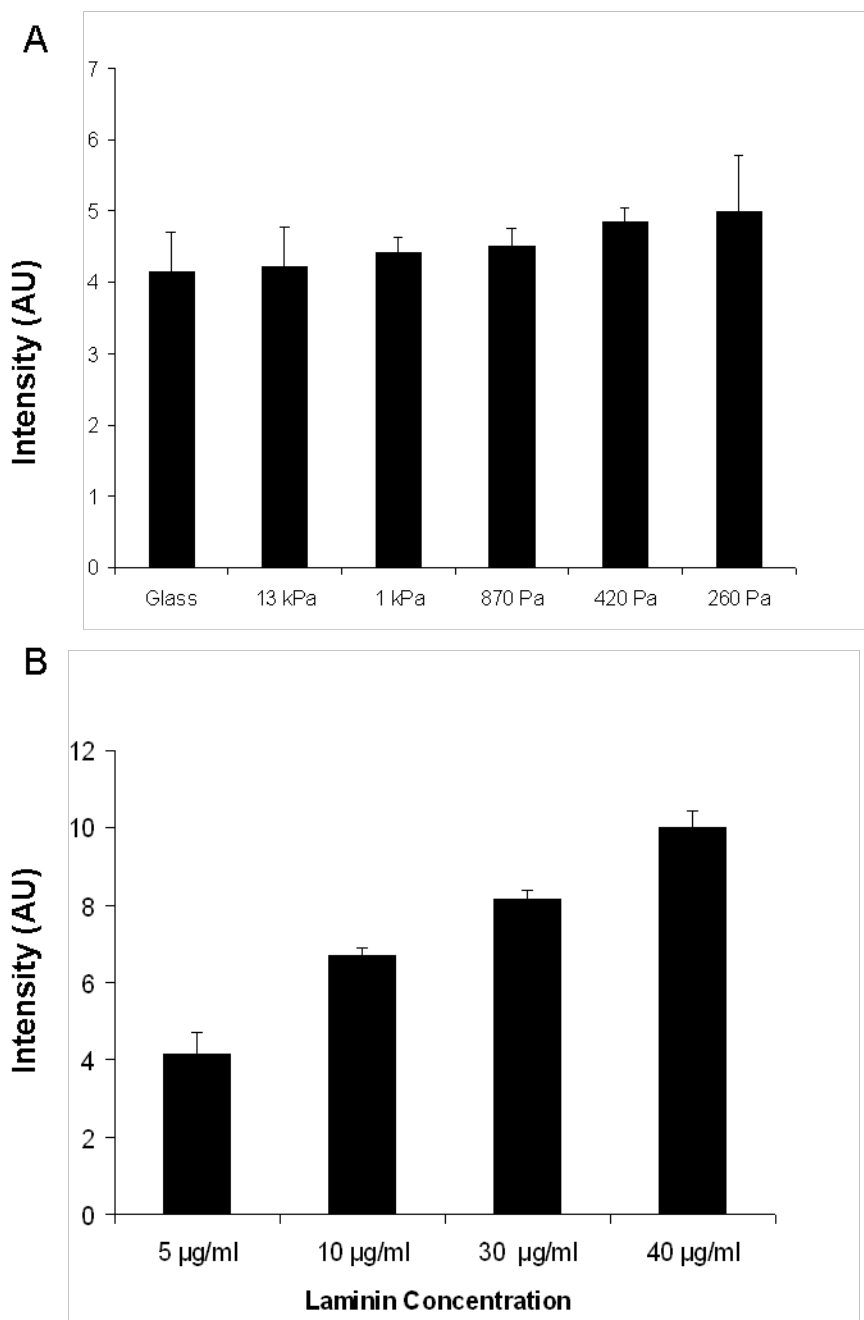


**Figure 6.1** Specification of ligand concentration was determined by adding fluorescently labeled anti-laminin antibody to laminin-coated substrates. Epifluorescence snapshots were captured for each gel with the average mean gray value displayed. The arbitrary fluorescence intensity values were similar for all gel substrates when incubated with 40µg/ml of laminin; however the intensity was significantly increased on glass substrates (A). Laminin titrations were performed to determine the approximate amount of laminin protein required on the glass surface to compliment the concentration present on the gels (B). To minimize effects from ligand concentration, 5µg/ml laminin was added to glass substrates, while 40µg/ml was added to PA gels to reach similar fluorescence intensities (as shown in A), after which no differences among intensities are reported. Error bars represent standard error.

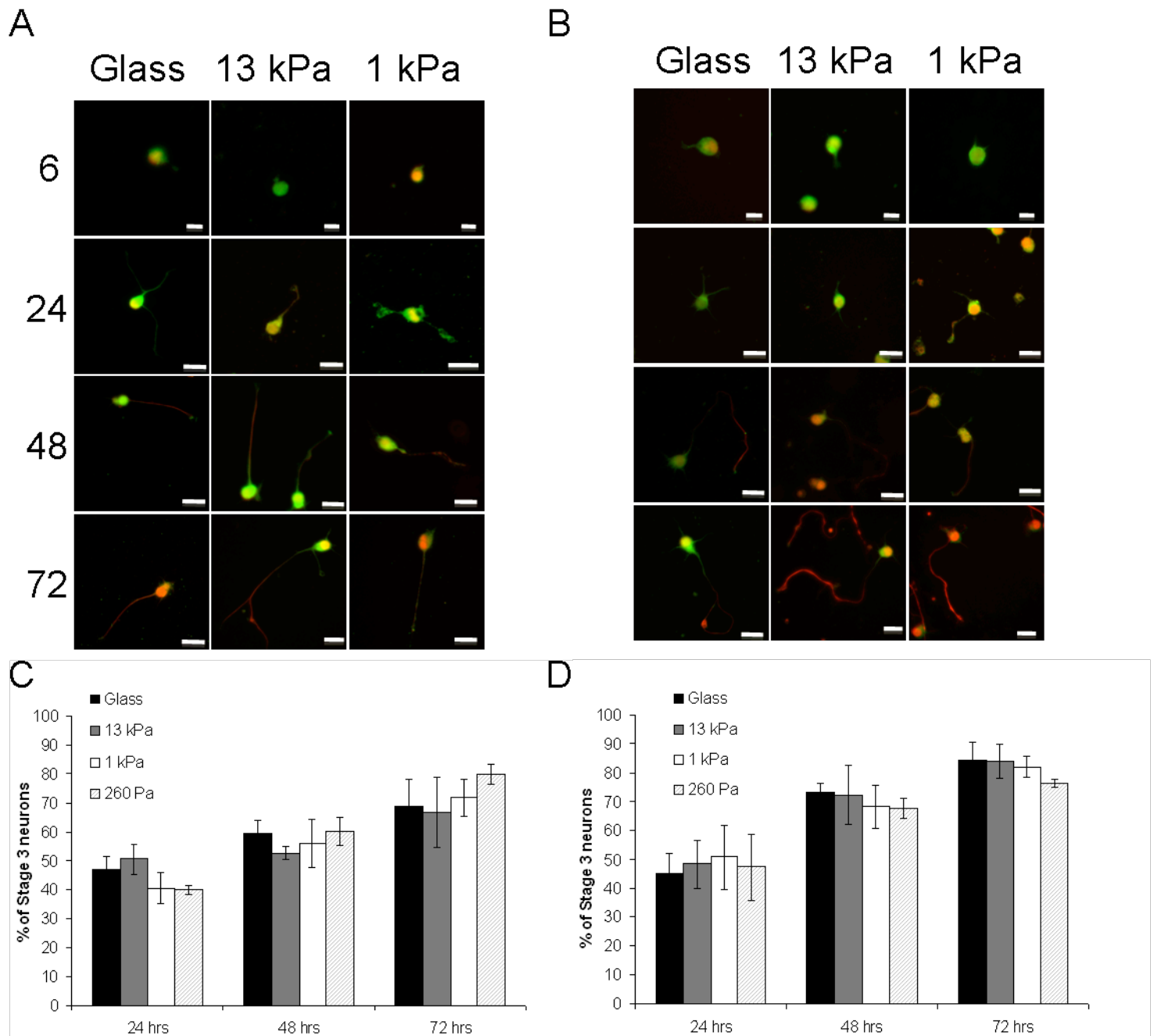


**Figure 6.2** Cortical neurons exhibit similar differentiation behavior regardless of stiffness. Cells were fixed at 6, 24, 48, and 72 hours after plating on laminin (A) and poly-d-lysine (PDL; B) coated substrates of varying stiffness. Cells were stained with MAP2 (green) to identify microtubule associated proteins in neurites, and SMI31 (red) to identify neurofilaments (NF) present only in the axon of each cell. Overall, a similar staining presence is observed during the course of the observed 72 hours. At 6 hours, small neurites are present, and stain positive for MAP2, but not SMI31. After 24 hours, some cells express positive staining for SMI31, however the majority of the cells only express MAP2 staining. At 48 hours, more noticeable NF localization occurs, with the strong identification of red axons most apparent after 72 hours. Cells were classified as Stage 1, 2 or 3 neurons for laminin (C) and PDL-coated (D) substrates. Stage 3 neurons refer to those cells with specified axons (positive staining for SMI31 in one process). No significant differences are observed among substrate compliance for either protein coating (using one-way ANOVA analysis,  $p > 0.01$ ), illustrating that cortical neurons differentiate independently of substrate stiffness. Error bars represent standard error.

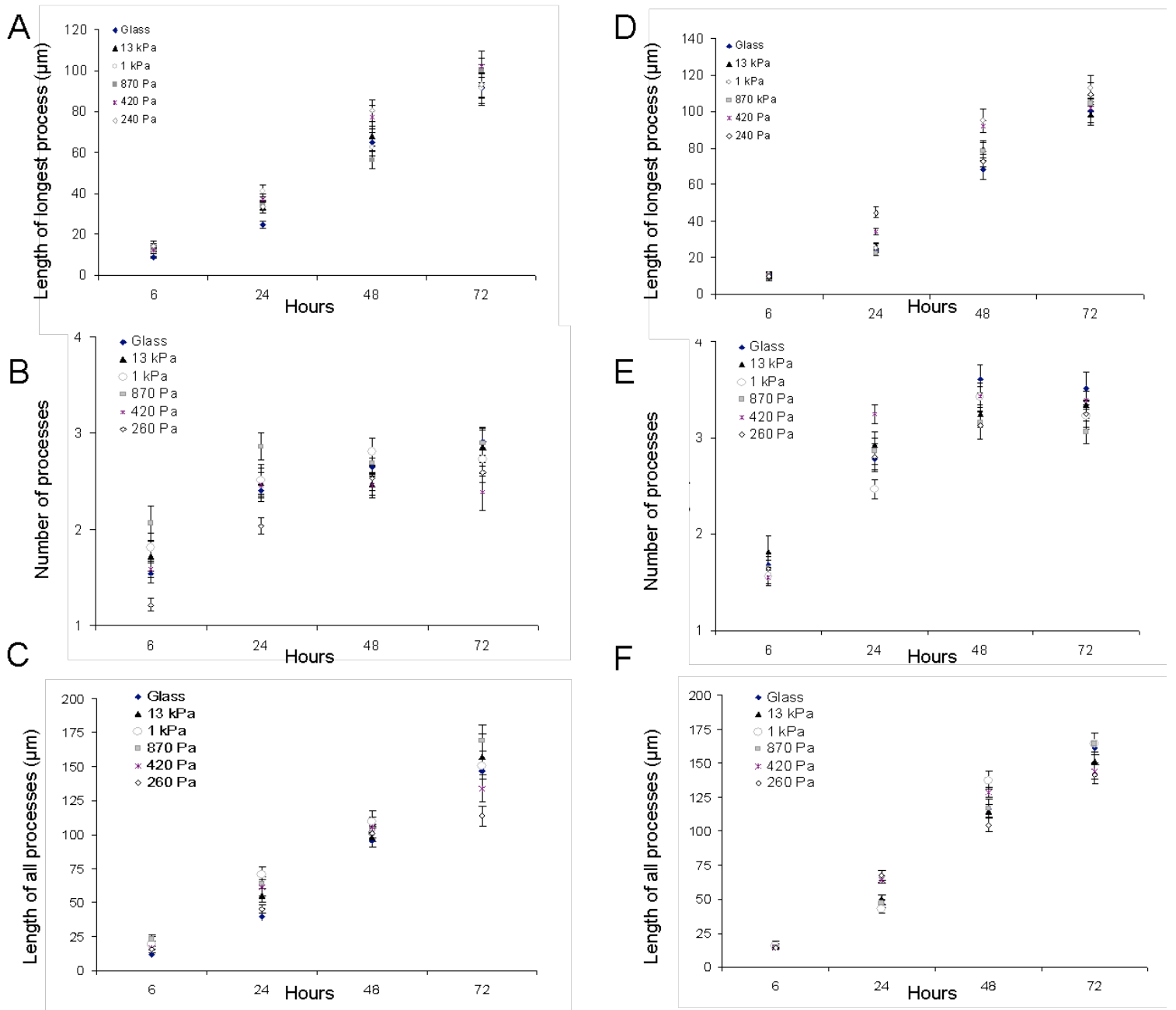


**Figure 6.3** Cortical neuron outgrowth was observed for cells plated onto substrates of varying stiffness. Cells were plated onto laminin (A-C) or PDL (D-F) substrates. The average length for the longest process (A and D), average number of processes (B and E) and the average length of all processes (C and F) per cell illustrate similar behavior regardless of substrate stiffness for both laminin and PDL substrates. All parameters illustrate no statistically significant differences after 72 hours (using one-way ANOVA analysis,  $p > 0.01$ ). (For all cases, error bars represent standard error and  $N = 30-60$  cells).

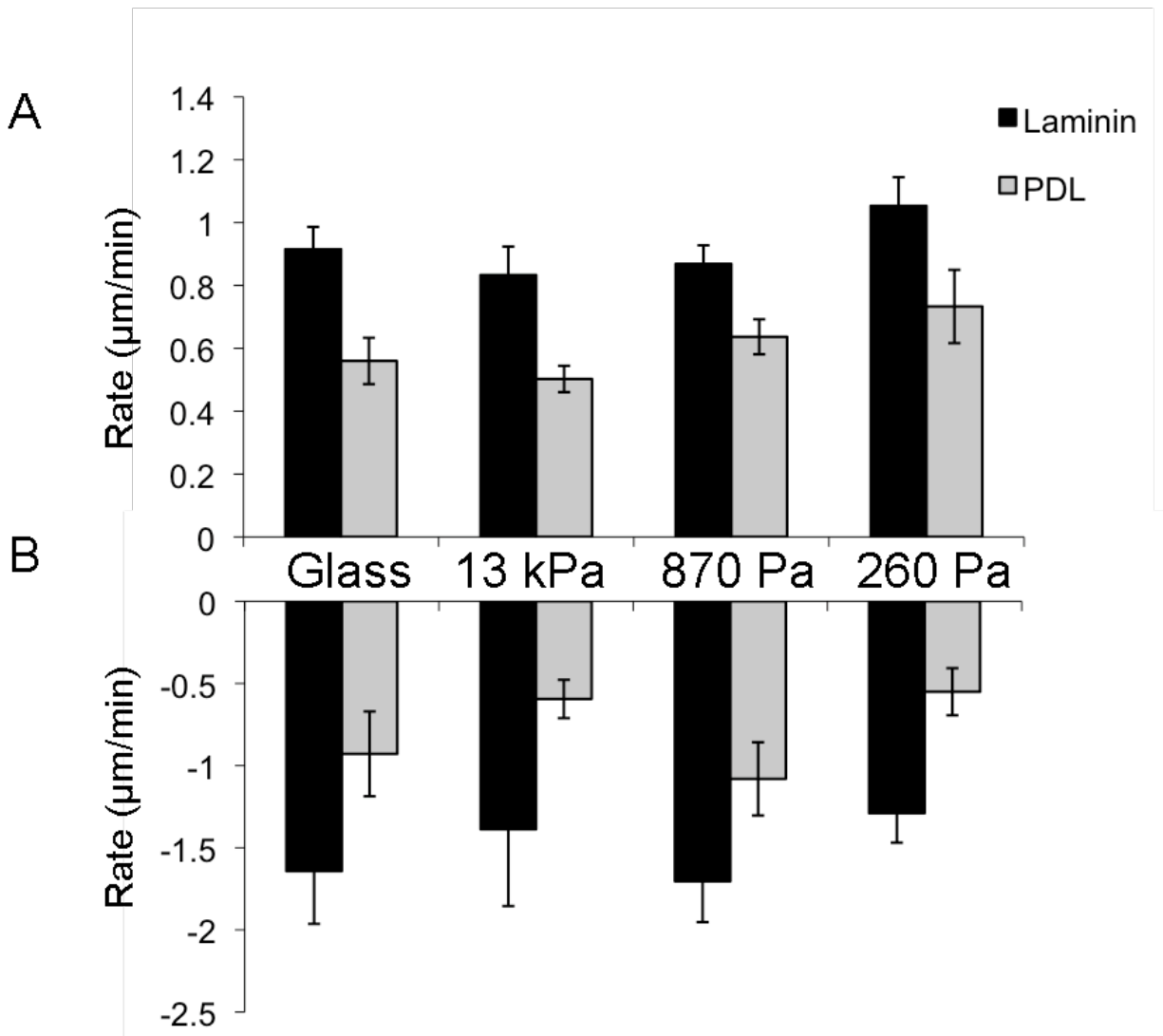


**Figure 6.4** Axon extension and retraction dynamics for laminin and PDL-coated substrates. The average rate of process extension for laminin and PDL-coated substrates (A). For extension, N = 59, 67, 61, and 43 for laminin coated glass, 13 kPa, 870 Pa and 240 Pa, respectively, while N = 38, 58, 45, and 22 for PDL-coated substrates. The average retraction rate for laminin and PDL-coated substrates (B). For retraction, N = 23, 22, 22, and 29 for laminin coated glass, 13 kPa, 870 Pa and 240 Pa, respectively, while N = 7, 14, 15, and 12 for PDL-coated substrates. Overall, both extension and retraction rates occur independently of substrate modulus for both laminin and PDL-coated substrates, with no significant differences occurring among stiffnesses (using one-way ANOVA analysis,  $p > 0.01$ ). Error bars represent standard error.

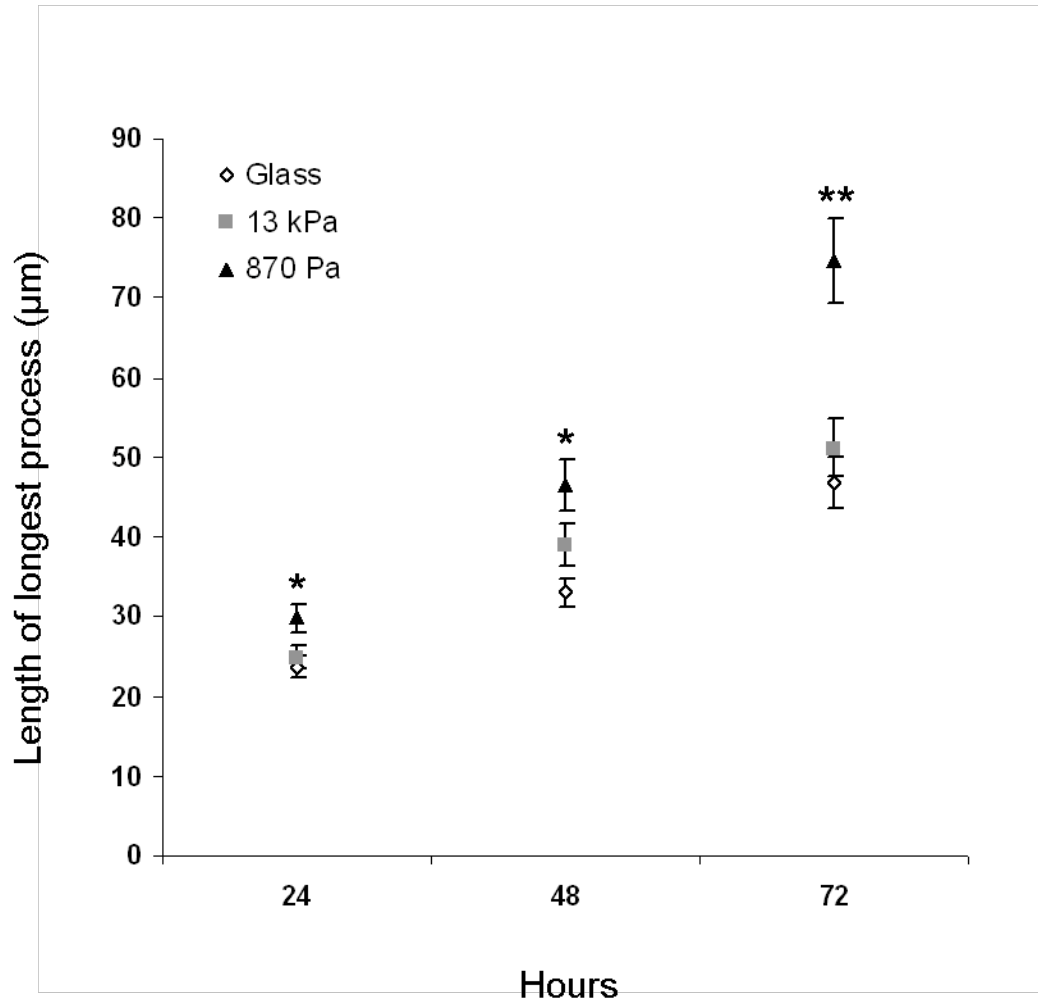


**Figure 6.5** Dorsal root ganglion (DRG) outgrowth on substrates of varying stiffness. Dissociated DRG neurons were plated onto stiff (glass), intermediate (13 kPa) and soft (870 Pa) PDL-coated substrates. The average length of the longest process per cell is reported at 24, 48 and 72 hours of culture. At all time points, process extension is statistically increased on 870 Pa PA gels compared to both glass and 13 kPa substrates (Using Student's T-test,  $p < 0.05$  (single asterisk) and  $p < 0.01$  (double asterisk),  $N = 30-50$  neurons per time point). Error bars represent standard error.

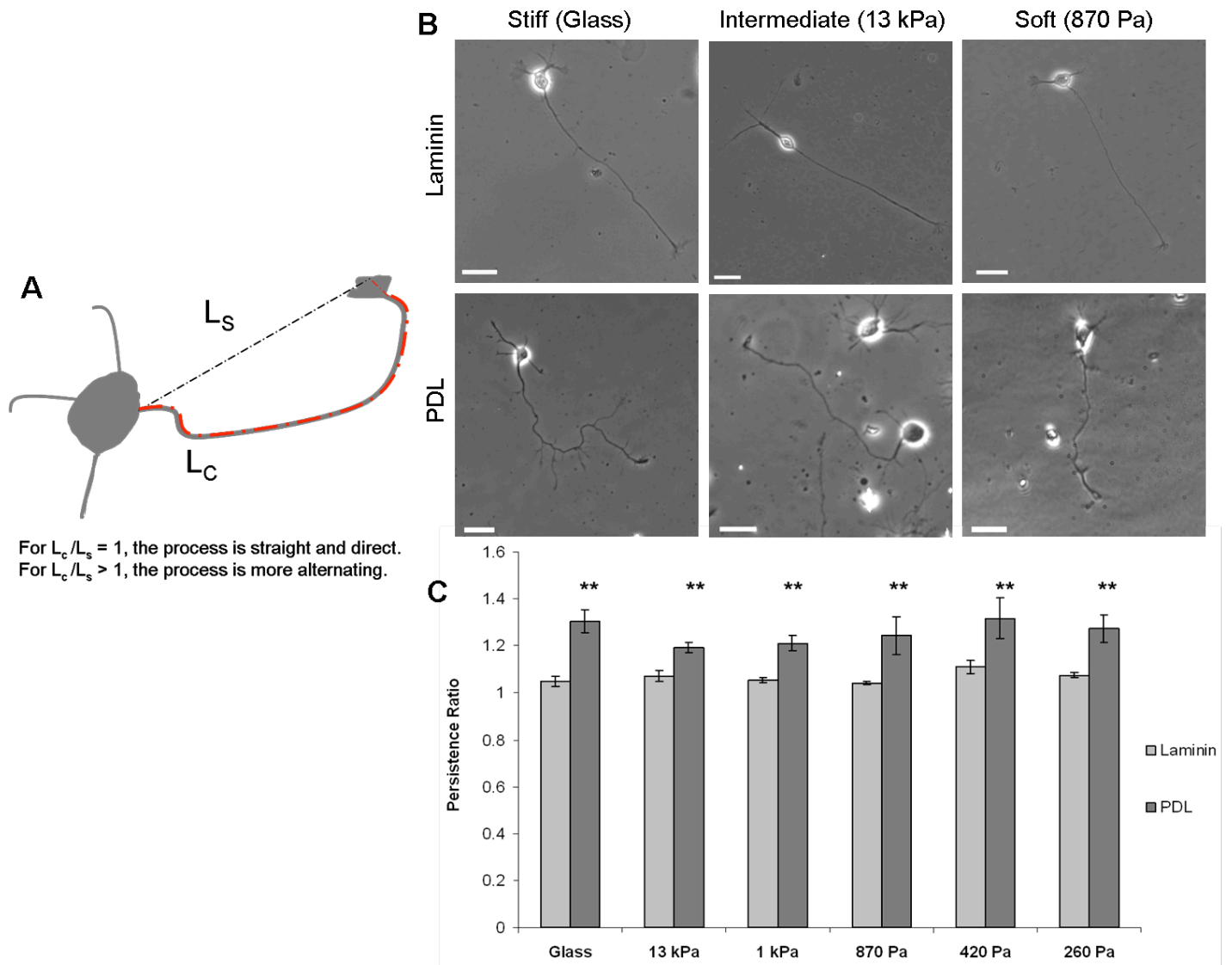


**Figure 6.6** Process extension occurs differently on laminin versus PDL-coated substrates. Schematic representation of persistence measurements (A). To quantify extension, we define an average persistence index ( $L_c/L_s$ ) for each condition, calculated by first measuring the contour length (red line), followed by the straight outgrowth length (black line). If  $L_c/L_s = 1$ , the process is directed and straight,  $L_c/L_s > 1$  identifies processes which are less directed. Representative images are shown after 72 hour for soft (870 Pa), intermediate (13 kPa), and stiff (glass) substrates (B). Noticeable differences in directionality are observed between PDL and laminin. Scale bar is  $25\mu\text{m}$  in all images. Quantified data illustrates that all processes extending from PDL coated surfaces are less persistent (higher ratio) (C). Asterisks denote statistical significance (Student's T-test  $p < 0.01$ ). Error bars represent standard error.

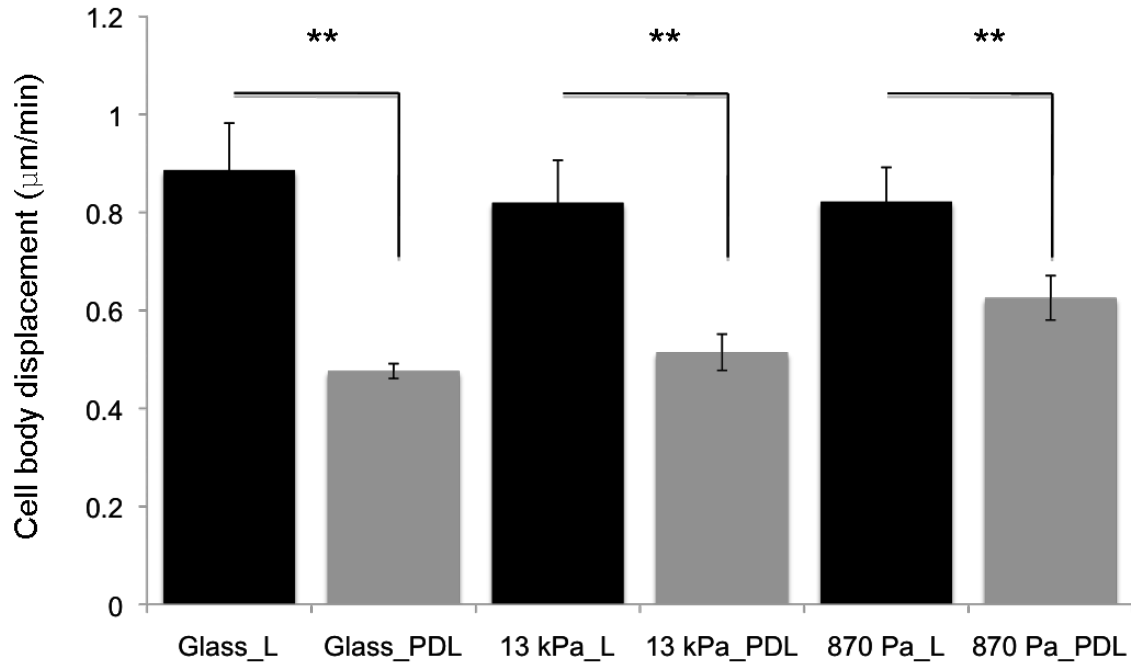


**Figure 6.7** Cell body displacements are increased on laminin-coated substrates. Mean squared displacements (MSD) were calculated for 10-15 cells. Neurons cultured on laminin-coated substrates (“L”) exhibit significantly larger cell body displacements during axon extension compared to those cultured on PDL (Student’s T-test,  $p < 0.01$ ). Error bars represent standard error.

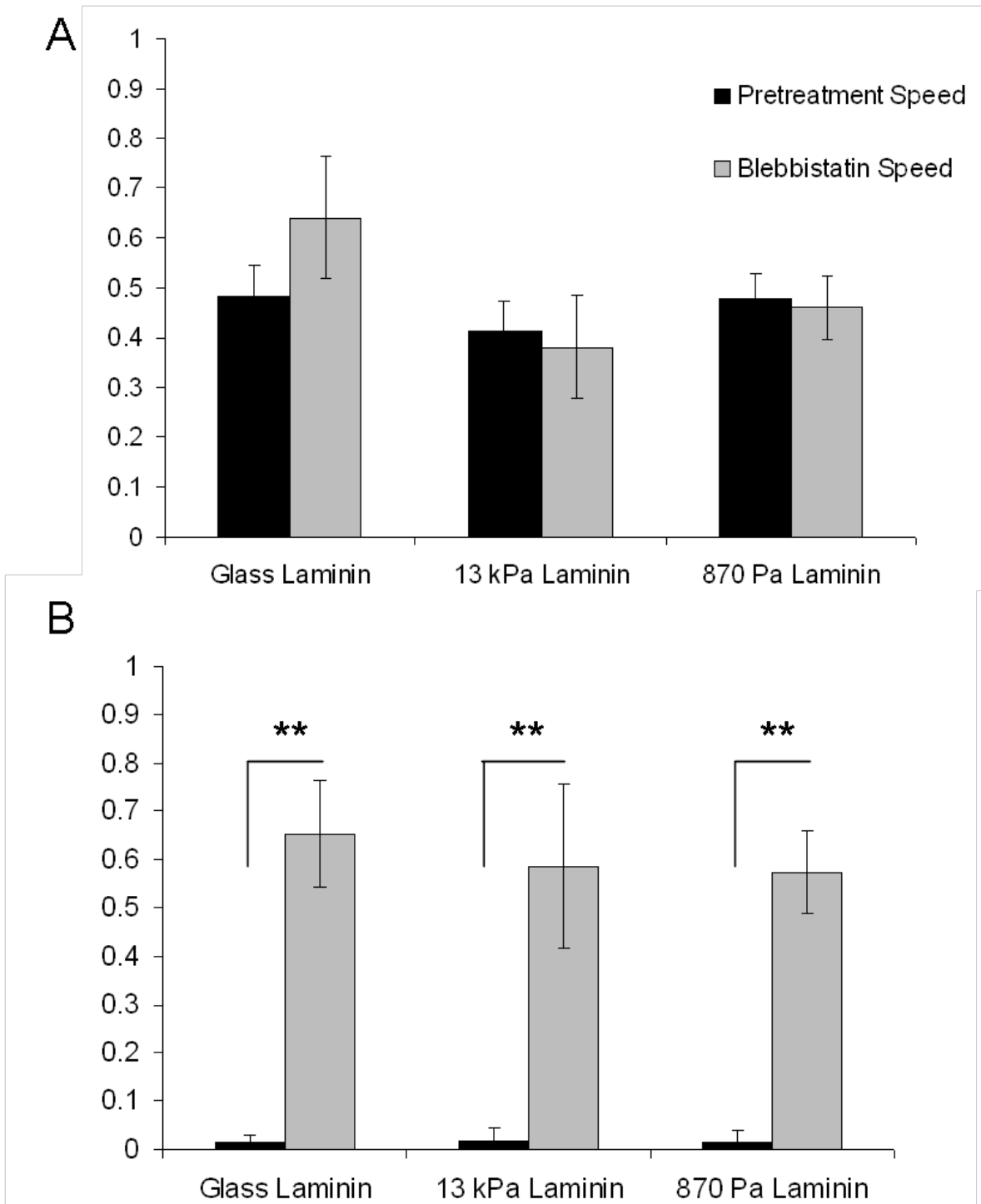


**Figure 6.8** Inhibition of myosin II with blebbistatin identifies extension dependent effects. Neurons plated onto laminin coated substrates were affected by blebbistatin similarly regardless of substrate stiffness, but dependent on extension behavior. MII inhibition caused no significant differences ( $p > 0.05$ , using Student's T-test) in the extension rate of previously extending axons for all laminin coated substrates (A). Also, there were no significant differences between the speeds during blebbistatin treatment between laminin-coated substrates of varying stiffness. When cells are initially in a stalled state, the inhibition of MII causes a statistically significant increase (asterisk denotes statistical significant using Student's T-test with  $p < 0.01$ ) in extension regardless of substrate stiffness (B). Error bars represent standard error.

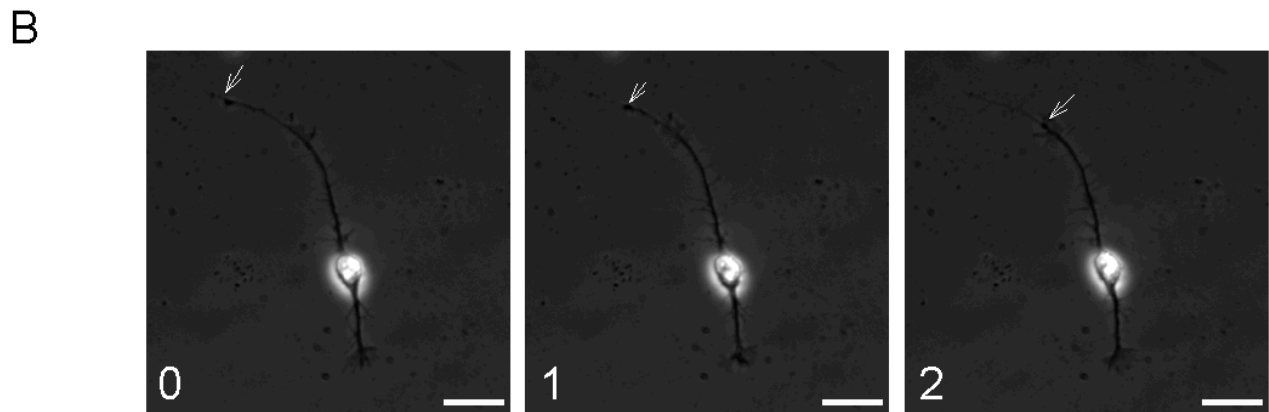
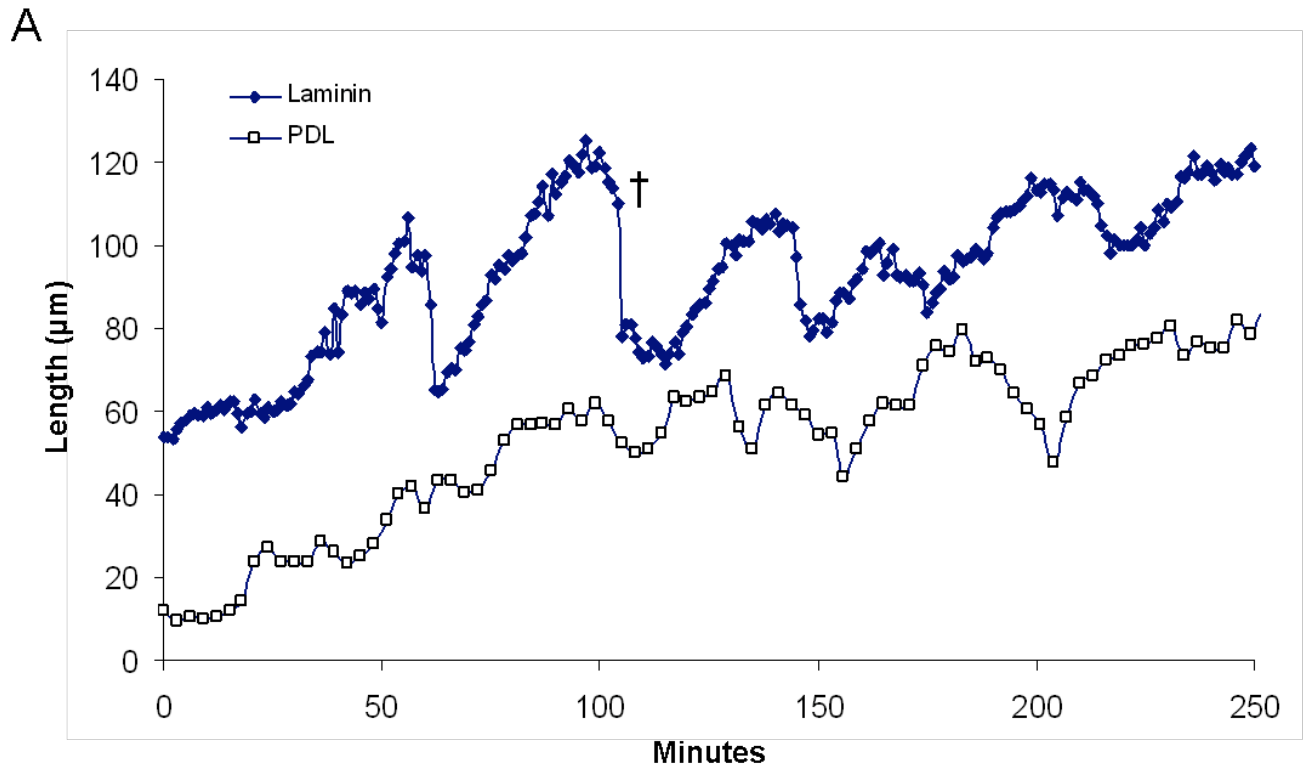


**Figure 6.9** Long-term observations of axon outgrowth between 49-53 hours of culture on laminin and PDL-coated glass substrates reveal numerous periods of extension, retraction and stalling (A). Note the laminin curve is displaced up  $25\mu\text{m}$  for clarity. The frequency of retraction events is increased for laminin substrates. An example of rapid retraction of the growth cone (marked by a cross in A) is illustrated in B. A reduction in approximately  $30\mu\text{m}$  occurs over the course of 2 minutes (time marked in lower left corner), while less dramatic retraction events are also observed (marked with an asterisk in A). This figure illustrates the increased duration of extension periods on PDL substrates and also highlights both the increased extension and retraction rates on laminin substrates. Scale bar is  $25\mu\text{m}$ .

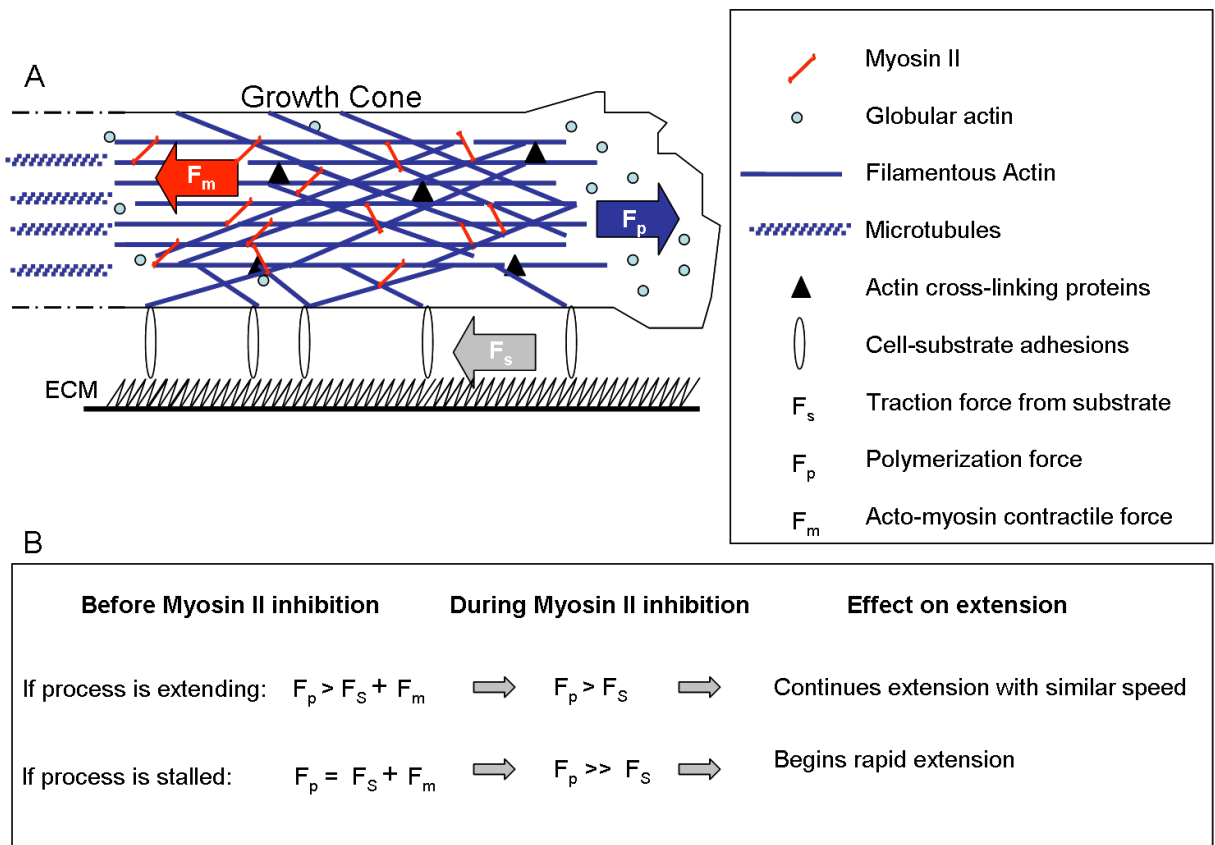


**Figure 6.10** A simplified schematic illustrating some of the major cytoskeletal components and forces involved in axon extension and retraction (A). Three major forces in the growth cone arise from the traction force the cell exerts on the substrate ( $F_s$ ) and extracellular matrix (ECM), the force of polymerizing actin filaments at the leading edge ( $F_p$ ), and acto-myosin contractile forces which are involved in both axon extension and retraction ( $F_m$ ). The effects of MII inhibition on axon outgrowth can be explained based on the balance of forces within the cell (B). When cells are initially extending prior to the addition of MII, the polymerization forces are greater than opposing traction and contractile forces, therefore the cell favors extension. When the process is stalled, however, the forces remain balanced, meaning the polymerization force is equal to the traction and contractile forces. During MII inhibition, the acto-myosin contractile force is compromised and extension is favored. This is consistent with our observations that during MII inhibition cells which were initially extending continue to extend, while cells which were previously stalled also begin to extend rapidly.

## 7 Summary and conclusions

It has been illustrated that cell spreading is a critical component of multiple biological phenomena, including embryonic development, cancer metastasis, immune response, and wound healing. The overall goal of the work presented here was to evaluate the biophysical properties of cell-substrate interactions during cell spreading and migration in order to develop a more comprehensive understanding on how cells interact with their substrates during critical biological phenomena.

The first objective was to investigate and characterize the initial stages of endothelial cell spreading and blebbing using cell-substrate specific microscopy techniques. We identify that cellular blebs appear after a sharp change in cellular tension, such as following rapid cell-substrate detachment with trypsin. Further, we illustrate that an increased lag phase of spreading appears with increased blebbing; however, cellular blebbing can be tuned by supplying the cell with more time to perform plasma membrane recycling. In sum, this aim illustrates that cellular blebs are very critical components of cell spreading and contribute to this mechanical homeostasis of the cell.

The second objective was to investigate the effects of cytoskeletal disruption and membrane modification on surface interactions and endothelial cell spreading. The first part of this objective involved disrupting cytoskeletal components and observing the effects on cell spreading and blebbing. We identify an inverse correlation between the amount of cell blebbing and the degree of spreading, consistent with our first aim. We developed software algorithms to detect individual bleb dynamics from TIRF and IRM images, and characterize three types of bleb-adhesion behaviors. Overall, we show that blebs initially create the first adhesion sites for the cell during spreading; however, their

continuous protrusion and retraction events contribute to the increased slow spreading period prior to fast growth. The detailed effects of blebbing dynamics on spreading behavior that we demonstrate presents a new picture on blebs during initial cell spreading. In the second part of this objective, we observed the effect of membrane cholesterol-modification on cell spreading event. We identify that cells which have been depleted of cholesterol exert more traction force than control or cholesterol-enriched cells. We are able to contribute this increase in traction to increased focal adhesions, which in turn, caused a decrease in total spreading area for single-cells as well as monolayers. Collectively, the work on cholesterol-modification emphasizes the importance of cholesterol in controlling and regulating the mechanical properties of the actin-plasma membrane complex, and the cellular mechanisms required for spreading. In addition, these results suggest that cellular cholesterol has global effects on cell properties through changes in actin cytoskeleton, beyond the local membrane environment.

Lastly, the third aim of this research was focused on investigating the effects of substrate stiffness on cortical neuron morphology, outgrowth and differentiation. In this work, we identify the elastic modulus of the cortex and characterize a polyacrylamide gel system that evaluates the effects of substrate stiffness on cortical outgrowth. Remarkably, we illustrate that unlike DRG and hippocampal neurons, cortical neuron differentiation and outgrowth is insensitive to substrate stiffness. We observe only morphological differences between laminin versus PDL-coated substrates; however, we do not observe any substrate dependent effects. Inhibition of myosin II results in similar extension behavior regardless of substrate stiffness. We hypothesize that this mechano-

insensitivity results from the homogenous environment of the developing cortex.

Ultimately, the results presented in this section emphasize that mechanotactic behavior is cell type specific, and the native environment of the cell likely dictates its response to modifications in mechanical properties.

Together, this research identifies cell-specific behaviors critical to spreading and migration. The thorough evaluations of spreading and migration behavior presented here contribute to the understanding of critical cellular phenomena and suggest potential therapeutic targets for treatment of cardiovascular disease and neurological disorders.

## 8 Future work and applications<sup>†</sup>

The work completed thus far opens up a variety of potential future studies. First, we have identified a critical role of cellular blebs during spreading. In particular, we show that blebbing can be modified through the regulation of membrane tension, directly affecting the degree of cell spreading. Future goals of these studies may be targeted towards understanding the role of blebs in cancer migration. It is likely that inhibition of cellular blebbing may serve as a potential approach to minimize cancer metastasis.

Second, we observe that cortical neurons do not sense substrate stiffness. It is possible that cortical migration *in vivo* is independent of substrate stiffness, since the signaling to order cortical neurons into distinct layers appears more chemical in nature and is reliant on the presence of the glycoprotein Reelin (272). It would be interesting to pursue future studies to determine whether the homogeneity of the cortex is retained throughout the rest of fetal and neonatal development. Differences in the mechanical properties during development may contribute to aberrant migration patterns that lead to diseases such as lissencephaly (described in section 2.2.2). A more thorough understanding of how these mechanical properties may change with age may contribute to the understanding of these migration disorders and potential ways to modify the mechanical properties of the environment through the incorporation of biomaterials with regulated stiffness patterns. In addition, it would be of importance to determine whether cortical neurons lack some form of mechanosensitive machinery, and whether this mechano-insensitive behavior is retained as single cells develop into intricate cortical networks. These studies may contribute to the treatment of neurological conditions

---

<sup>†</sup> Adapted from: Norman, LL, Stroka, K, and Aranda-Espinoza, H. 2009. Guiding axons in the central nervous system: A tissue engineering approach. *Tissue Engineering Part B*. 15(3) 291-305.

following traumatic brain injury, where sudden impact may alter both the chemical and mechanical environment of the brain.

It has become apparent that continued research concerning neuron regeneration is going to require combinatorial strategies which utilize the advantageous characteristics of mechanical, chemical and cellular responses. In terms of biomaterials, this would include a biomaterial that is capable of degrading after the axon has passed the trauma site and reached the synapse target. Degradable materials which are capable of releasing controlled amounts of neurotropic factors would also be beneficial, in particular for encouraging directed growth over a lesion site. Furthermore, developing materials which are heterogeneous in nature may allow for more directed axonal extension. Since different stiffness can dictate varying cell responses, this could be used to create scaffolds with heterogeneous mechanical properties, tailored to suit growth in a particular direction. A heterogeneous nature of various pits and precise linear channels, such as those described by Stokols, et al. (268) that have illustrated directed axonal extension, should also be considered when designing an extension pathway. Also, varying the concentration of ECM proteins and types of signaling molecules along the scaffold could potentially direct the neuron using chemoattractive or repulsive signaling mechanisms. Lastly, it is likely that materials will need to be tailored to specific class of axons, considering the wide variety of effects seen when using mechanically similar substrates with different neuron types. It is important to note, that even with complete axon extension across the distal portion of the biomaterial, it is still not well understood what type of functional recovery will be restored, and whether the remyelination of axons will need to be promoted with additional interventions (103). Further focus on functional

recovery and myelination will be important following the observation of complete axon regeneration using axon guidance materials.

The field of tissue engineering has an unmistakable importance in the development of nerve regeneration materials. The mechanical properties, design, and chemical delivery methods will be critical components in guiding axons to their proper target sites. The final step in functional recovery after neurological trauma or disease requires appropriate synapse formations, which can only occur after proper growth cone migration. The most reliable biomaterials will require optimizing advantageous qualities of both mechanical and chemical components. Collectively, this work identifies specific cell-spreading events and behaviors which contribute significantly to the understanding of neuronal development and cell spreading phenomena. Applying the information gathered in this research to the development of more optimized biomaterials for spinal cord injury and alternative therapeutics, such as regulating the environmental stiffness during injury or disease, will greatly impact the field of bioengineering.

## 9 Appendix:

### *Appendix A: Coverslip activation and polyacrylamide gel polymerization*

Polyacrylamide (PA) gels are attractive substrates for the evaluation of substrate stiffness effects on cell behavior due to the ability to easily tune the stiffness of the gel. First, glass coverslips must initially be activated to allow the attachment of the PA gels. To perform the activation procedures, glass coverslips (22 x 22 mm; Fischer Scientific, Pittsburgh, PA) were coated with 0.1M NaOH (Fischer Scientific), followed by 3-aminopropyltrimethoxy silane (Sigma, St. Louis, MO), which allows for polyacrylamide binding. Coverslips were then fixed with 0.5% glutaraldehyde (Sigma) and allowed to air dry. Polyacrylamide gels were prepared with varying concentrations of acrylamide (40% Acryl; Bio-Rad, Hercules, CA), and bisacrylamide (2% Bis; Bio-Rad) using 3% or 8% acrylamide, and 0.04 - 2% bisacrylamide for final concentrations. A total of 25 - 35 $\mu$ L of gel solution was placed on top of the activated coverslip, and covered with a glass slide (Fisher Scientific) in order to ensure a flat gel. After 30 minutes of polymerization, the coverslip was removed and the attached gel was measured by microscopy to be approximately 80 - 100 $\mu$ m thick. Gels were rinsed and stored in PBS.

## ***Appendix B: Imaging conditions***

### ***Interference reflection fluorescence (IRM) microscopy***

As previously mentioned, IRM is a technique used to detect surface-to-surface distance based on interference between light rays reflected from the substrate/medium interface and those reflected from the medium/cell interface. Patterns with varying degrees of dark and light zones arise from this interference, and gray scaled images identify the areas of the membrane closest to the surface as dark gray or black, while those further appear as lighter shades of gray or white. IRM is therefore an optimal method when evaluating cell attachment, adhesion and spreading behavior (269). Bovine aortic endothelial (BAEC) cells were observed with an inverted microscope (Olympus American Inc.) and fitted with a 100x oil immersion objective lens and a 100 W mercury lamp (Olympus). A CCD camera (Retiga SRV camera, QImaging) was used for image recording. All time-lapse experiments were performed in a closed microscope chamber (Precision Plastics, Inc.) to ensure characteristic culture conditions including 5% CO<sup>2</sup>, 50% humidity and 37°C.

### ***Total internal reflection fluorescence (TIRF) microscopy***

Total internal reflection fluorescence (TIRF) microscopy has recently become a popular method for evaluating cell dynamics including actin kinetics (120, 270) and cell-substrate interactions (28). TIRF microscopy utilizes a thin layer of illumination, termed an “evanescent field”, which allows for excitation of fluorophores near the surface (~80 nm) while avoiding more distant fluorophores (120). TIRF spreading experiments were performed on an inverted microscope (Olympus American Inc, Center Valley, PA), fibre-optically coupled with two ion lasers (Melles Griot, Rochester, NY) for GFP (488nm)

and mCherry (561) excitation. A CCD camera (Rolera-MGi camera, QImaging, Surrey, BC Canada) was used for image recording.

### ***Appendix C: IGOR image analysis software algorithms***

Algorithms previously written by Sengupta and Aranda-Espinoza (2) to characterize neutrophil spreading were used in order to quantify spreading area over time, and was modified to identify individual bleb adhesion zones. Algorithms were written based on fitting intensity histograms using IGOR-Pro data analysis software. Briefly, by exploiting the fact that the background intensity using IRM remains constant while the cell is spreading, time lapse images can be turned into binary images which identify the background versus the spreading cell. First, a pixel outside of the cell spreading area is selected and becomes the center of a 5x5 pixel matrix; which the intensity histogram can then be fitted with a Gaussian. The same is performed for a 5x5 matrix of a selected pixel within the cell boundaries. In the Gaussian distribution, the average intensity within each 5x5 matrix is the position of the center. The spread of intensity within each matrix is the width of the Gaussian. These two values are saved and stored in the program as the “average-image” and “width-image”, respectively. From the average width-image, a threshold can be determined so that all the pixels less than the threshold are assigned a value 0, and those above the threshold are assigned a value 2. This creates a binary image of background (black) versus spread cell (white). To automate these procedures, the abovementioned criteria define the cell versus the substrate for the initial frame of a time lapse. The same average values are then applied to each frame of the time lapse as the cell is spreading or moving across the substrate. This allows for consistent identification of zones of close adhesion, since the gray value, which identifies these “areas closest to the substrate”, remains consistent throughout the time lapse.

Lastly, the program can plot the area of the cell as it spreads (based on the binary images).

## ***Appendix D: Modeling cell blebbing and plasma membrane tension***<sup>†</sup>

The aim of the theoretical model is to obtain a general description for the kinetics of cell adhesion that includes area recycling between the plasma membrane (PM) and area storage within membrane blebs. The model seeks to reproduce the kinetic evolution of parameters that can be directly observed in the experiments, namely the cell area in contact with the substrate (which we call  $A_c$ ) and the number of blebs in the cell  $N_b$ . All other variables introduced in the model, and in particular the various relevant tensions, are relative variables which are chosen to vanish in the reference state of a fully relaxed, non-adhering cell.

### ***Constitutive and kinetic relations for the spreading of a visco-elastic cell***

From a mechanical point of view, a cell is a very complex visco-elastic system powered by energy consumption. Nevertheless, it has been theoretically proposed and experimentally verified (1, 147) that as far as spreading is concerned, the cell essentially behaves as a viscous drop. The adhered area kinetics follows from a balance of forces between the adhesion driving force (characterized by an adhesion energy per unit area  $\varepsilon$ ) and a viscous dissipation:  $\eta_c \dot{A}_c = \varepsilon$ , where  $\eta_c$  (Energy x time /length<sup>4</sup>) characterizes energy dissipation during cell spreading and is mostly controlled by viscous flow through the cytoskeleton cortex as the cell spread (1). Cells stop spreading after a while, meaning that some elastic stress must be stored during spreading, that eventually balances the adhesive driving force at large strain. Here, we assume that this elastic stress is stored as membrane tension  $\gamma_m$ , and replace the spreading equation above by  $\eta_c \dot{A}_c = \varepsilon - \gamma_m$ . By

---

<sup>†</sup> This section has been submitted for publication as supplementary information for: Norman, LL *et al.* Cell blebbing and membrane area homeostasis in spreading and retracting cells. (Under Review, April 2010).

analogy with giant unilamellar vesicles (GUVs) (271), in which the membrane tension is known to be related to the difference between the apparent area and the true membrane area (called  $A_m$ ), we adopt the simple linear relationship  $\gamma_m = k_m(A_c - A_m)$ , where  $k_m$  is the membrane effective stretching modulus.

The plasma membrane of a cell constantly exchanges material with the cell interior by endo and exocytosis, with the entirety of the PM being recycled over about one hour (152). The rate of endocytosis is known to inversely correlate with the tension of the plasma membrane (272), and a general relationship between rates of membrane transport and difference of membrane tensions within the cell can be expected (156, 273). In order to translate these facts into a mechanical equation, we assume that the balance of endo and exocytosis depends on the difference between the membrane tension and the tension  $\gamma_i$  of inner organelles (e.g. the Golgi), again assuming linear kinetics:

$\eta_i \dot{A}_m = \gamma_m - \gamma_i$ , where the area at the cell surface includes the PM area, but also the area  $A_b$  contained in blebs:  $A_m = A_c + A_b$ . Finally, in order to comply with our assumption that cell spreading is eventually limited by an increase of membrane tension, the inner tension is assumed to increase as area is transferred to the PM:  $\gamma_i = k_i A_m$ .

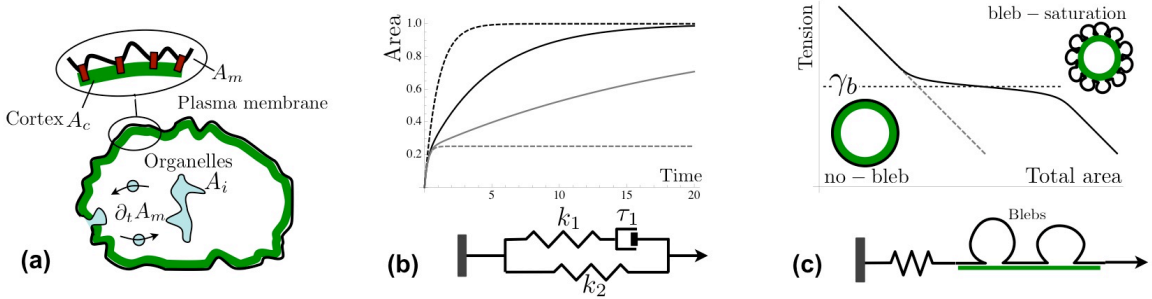
### ***Kinetic equations***

Combining all the rules described above, the evolution of the adhered area is described by the set of equations:

$$\eta_c \dot{A}_c = \varepsilon - \gamma_m \quad \text{with} \quad \dot{\gamma}_m + \frac{k_m + k_i}{\eta_i} \gamma_m = k_m(\dot{A}_c + \dot{A}_b) + \frac{k_m k_i}{\eta_i} (A_c + A_b) \quad [1]$$

We will see below that the area contained in blebs  $A_b$  is fixed by the membrane tension  $\gamma_m$ , so this set of equation uniquely determines both the cell shape and its mechanical

properties ( $A_c$  and  $\gamma_m$ , respectively). The visco-elastic model leading to Eq.[1] for the tension  $\gamma_m$  is equivalent to the so-called “standard linear solid model” for the total apparent membrane area (apparent cell area plus blebs  $A_c + A_b$ ). This model, shown in Appendix Fig. 1 consists of a Maxwell model (a spring of stiffness  $k_1$  in series with a dashpot of relaxation time  $\tau_m$ ), in parallel with a spring of stiffness  $k_2$ , with  $k_1 = k_m^2 / (k_m + k_i)$ ,  $k_2 = k_m k_i / (k_m + k_i)$ , and  $\tau_m = \eta_i / (k_m + k_i)$ .



**Appendix Fig.1** Constitutive viscoelastic equation for the cell membrane. (a) Sketch of the cellular model: The membrane tension is related to the area difference between the plasma membrane and the cortex, area transfer with internal organelles. (b) Equivalent visco-elastic model for the total cell membrane area (spring and dashpot are linear elastic and viscous components) and variation of the cell area with time upon constant driving force ( $k_1 = 3 k_2$ ); dashed grey and black curves are purely elastic cells with very fast and very slow area transfer ( $\tau_m \rightarrow 0$  and  $\tau_m \rightarrow \infty$ , respectively). Solid grey and black curves are with membrane area transfer  $\tau_m = 5\tau_c$  and  $\tau_m = \tau_c$ , with  $\tau_c = k_2 / \eta_c$  the characteristic spreading time. (c) Stress-stain relationship for blebs in series with a spring: Dashed grey and black curves are for spring only and spring plus blebs, respectively. The latter shows that blebs maintain the membrane tension to a characteristic value  $\gamma_b$ , between the no-bleb and bleb-saturation regimes.

### ***Bleb statistics***

Blebs occur because of a localized detachment of the PM from the cytoskeleton (CSK). This process is helped by the internal cell pressure, partly built by acto-myosin contraction, and is prevented by membrane-cortex adhesion and membrane tension. This can be formalized in a bleb energy (142):  $E_b = -PV_b + \gamma_m \Delta S_b + \varepsilon_b S_b$ , where  $\varepsilon_b$  is the binding energy between the PM to the CSK,  $P$  is the pressure difference, and  $V_b$ ,  $S_b$  and  $\Delta S_b$  are the volume in the bleb, the area of membrane-free CSK, and the area increase due to the presence of the bleb. Although the following is qualitatively valid for blebs of any size, we concentrate for simplicity on low aspect ratio blebs  $S_b/R_b^2 \ll 1$  where  $R_b^2$  is the radius of curvature of the bleb, in which case this energy can be written

$$E_b = \varepsilon_b S_b + \frac{(\gamma_m - PR_b)S_b^2}{4\pi R_b^2} \quad [2]$$

Optimization with respect to the bleb curvature produces the Laplace law:

$R_b = 2\gamma_m / P$ ,  $E_b = \varepsilon_b S_b - P^2 S_b^2 / (16\pi\sigma)$ . This energy shows a maximum for a given bleb area  $S_b^*$ , corresponding to a nucleation energy barrier  $E_b^*$ :

$$E_b^* = 4\pi \frac{\gamma_m \varepsilon_b^2}{P^2} \quad S_b^* = 8\pi \frac{\gamma_m \varepsilon_b}{P^2} \quad [3]$$

The smaller the barrier, the higher the probability to observe blebs on a given cell. Note that the nucleation energy is expected to be quite large (of order  $1000k_B T$  for  $\varepsilon_b \sim 10^{-4} J/m^2$ ,  $\gamma_m \sim 10^{-4} J/m^2$ , and  $P \sim 300 Pa$ ), so spontaneous bleb nucleation is very unlikely to arise purely from thermal fluctuations. It has been suggested that a local increase of pressure near the cell PM due to acto-myosin contractility provides the driving force for bleb nucleation (143). Equation [3] shows that the nucleation energy barrier can also be decrease by a drop of membrane tension. Since blebs on detached cells

can persist for times consistent with the slow membrane recycling, we argue that they are a signature of a decrease of membrane tension.

The life cycle of a bleb involves nucleation and growth, followed by the polymerization of a new actin cortex underneath the bleb membrane and by bleb retraction. Following Kramer's nucleation theory (274), the rate of bleb nucleation can be expected to depend exponentially on the energy barrier  $k_n = k_n^0 e^{-E_b/E_t}$ , where  $k_n^0$  is the rate of bleb nucleation in the absence of energy barrier and  $E_t$  is the energy available from local fluctuations of the cell parameters (linkers concentration, local membrane tension, and local pressure). The rate of bleb retraction  $k_r$  on the other hand depends mostly on the time needed to polymerize a cortical layer thick enough to retract the bleb, and can be assumed constant for simplicity. The simplest form of a kinetic equation for the evolution of the average number of bleb  $N_b$  per cell, that includes nucleation and retraction, reads:

$$\frac{dn_b}{dt} = k_n (1 - n_b) - k_r n_b \quad [4]$$

Where  $n_b \equiv N_b S_b^* / A_{b0}$  is the fraction of cell area covered by blebs ( $A_{b0}$  is the maximum total area in blebs), and where the average bleb area is assumed to be of order  $S_b^*$ . A steady state is reached when bleb nucleation balances bleb retraction. From Eq.[3], one sees that the bleb nucleation energy increases linearly with membrane tension, so that the amount of cell blebbing is highly sensitive to membrane tension:

$$n_b = \frac{1}{1 + e^{\beta(\gamma_m - \gamma_b)}}, \text{ with } \beta \equiv \frac{4\pi\epsilon_b^2}{E_T}; \gamma_b = E_T \frac{P^2}{\epsilon_b^2} \log \frac{k_r}{k_n^0} \quad [5]$$

where  $\beta$  is the bleb sensitivity to membrane tension and  $\gamma_b$  a threshold tension below which cell blebbing can be observed. Equation [5] shows that blebs are absent under

high tension  $\gamma_m \gg \gamma_b$ , and entirely cover the cell surface under low tension  $\gamma_m \ll \gamma_b$

(Appendix Fig. 1).

### ***Final equations***

The effective cell stiffness at long time  $k_2$  controls the adhered area at saturation:  $A_{c, sat} = \varepsilon / k_2$  (Eq. [1]). To reduce the number of parameter, we express all tensions in unit  $\varepsilon$ , all areas in unit  $A_{c, sat}$ , and all times in unit of the characteristic spreading time  $\tau_c = \eta_c / k_2$ . The problem reduces to the set of normalized equations:

$$\begin{aligned} \dot{A}_c &= (1 - n_b) - \gamma_m \quad ; \quad \dot{\gamma}_m + \frac{\gamma_m}{\tau_m} = \left(1 + \frac{k_1}{k_2}\right)(\dot{A}_c + \dot{A}_b) + \frac{(A_c + A_b - A_b(\gamma_m = 0))}{\tau_m} \\ A_m &= A_c + A_b - A_b(\gamma_m = 0) - \frac{\gamma_m}{1 + k_1 / k_2} \quad ; \quad A_b = \frac{A_{b0}}{1 + e^{\beta(\gamma_m - \gamma_b)}} \end{aligned} \quad [6]$$

The predictions of these equations in various situations of interest for the experiments presented in the text are discussed below.

### ***Results:***

#### ***Area transfer and cell spreading***

In the absence of blebs ( $A_{b0} = 0$ ) the model is linear and can be solved analytically. Within our framework, the spreading of a purely elastic cell follows an exponential saturation of the form  $A_c(t) = \alpha A_\infty(1 - e^{-t/\tau})$  and reaches the saturation area  $A_\infty$  with a single timescale  $\tau$ . With our normalization Eq. [6],  $A_\infty = \tau = 1$  if membrane recycling is very fast ( $\tau_m \rightarrow 0$ ), and  $A_\infty = \tau = 1/(1 + k_1 / k_2)$  if recycling is absent ( $\tau_m \rightarrow \infty$ ). Tension-controlled membrane recycling allows the cell to spread more, as shown in Appendix Fig. 1(dashed curves). The viscoelastic model that takes into account the finite time of area transfer between the PM and inner organelles exhibits a second

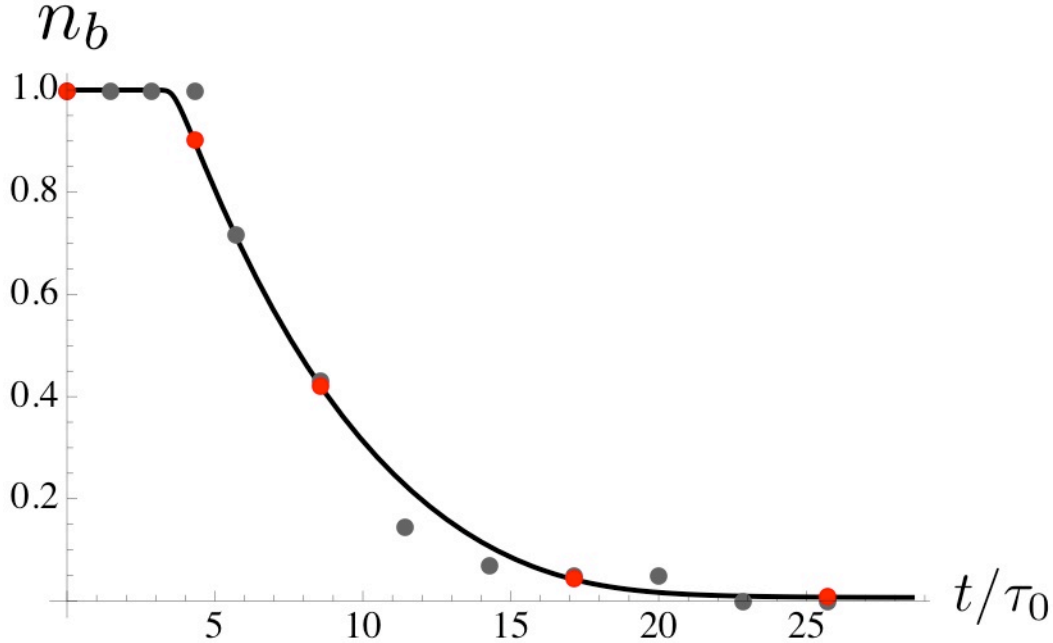
timescale  $\tau_m$  characteristic of this transfer (Appendix Fig. 1, solid curves). While the initial spreading kinetics is controlled by viscous dissipation in the cytosol (friction parameter  $\eta_c$ ), the later stage is slower, controlled by the kinetics of area transfer (parameter  $\eta_i$ ).

### ***Blebs and membrane tension***

Mechanically, blebs behave in a way reminiscent of smaller membrane outgrowth such as caveolae (155), which can regulate membrane tension by sequestering excess membrane area. This is illustrated during the rapid detachment of strongly adhered cells. As discussed above, the PM area  $A_m$  (that includes blebs) increases by membrane transfer during cell spreading to match the increase of the apparent cell area  $A_c$ . Upon cell detachment by trypsin, the cell quickly rounds up under the contractile cortical stress, without rapid change of the PM area. The subsequent increase of the PM excess area  $A_m - A_c$  decreases the membrane tension, which might drop below the threshold  $\gamma_b$ , allowing for the formation of membrane blebs. By incorporating some of the excess area, blebs keep the membrane tension to a value close to  $\gamma_b$ . The tension can however drop further if the excess membrane area becomes so large that the cell surface is saturated by blebs ( $n_b \cong 1$ ).

While the formation of blebs upon cell detachment is not easy to monitor, one may quantify the disappearance of membrane blebs after cell detachment (on non-adhered cells) as membrane area transferred away from the PM slowly reduces the area excess (Appendix Fig. 2). With our experimental conditions, the number of bleb remains initially constant, which we interpret as the signature that immediately after rounding up, the detached cell is saturated with blebs and its tension is lower than the blebbing

threshold. The subsequent decrease of the number of blebs follows the kinetics of membrane area transfer, until blebs completely disappear for the cell surface.

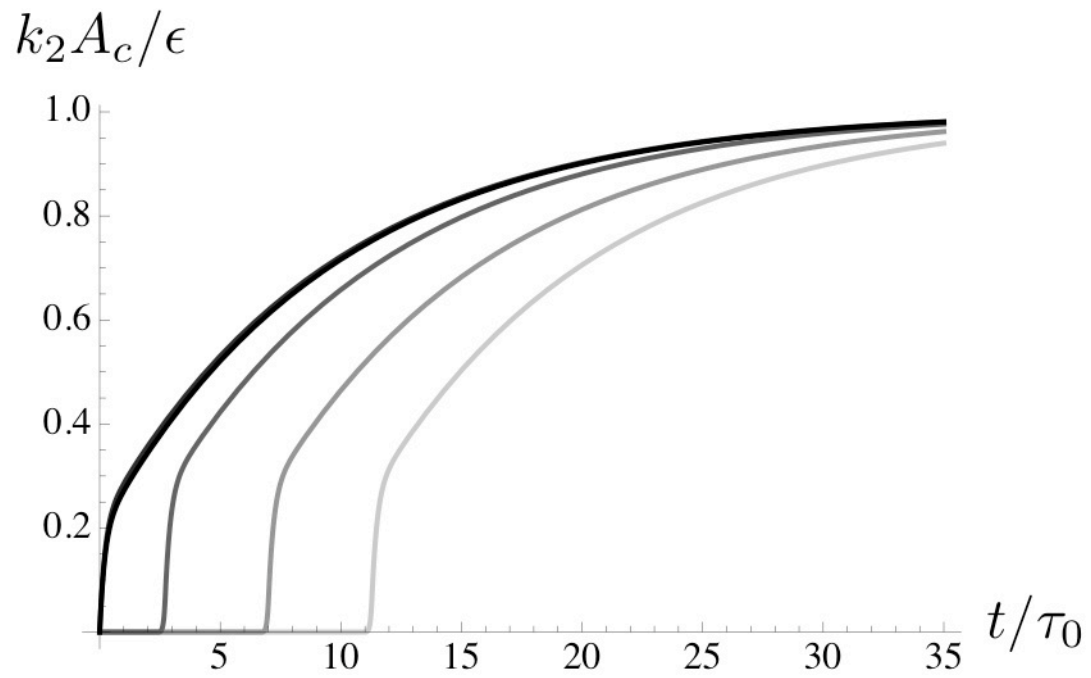


**Appendix Fig. 2** Evolution of the (normalized) average number of blebs cell  $n_b$  with time. In both the experimental observations (grey points) and the theoretical curve, cells were allowed to spread until complete saturation before being detached from the substrate, leading to pronounced cell blebbing. The decrease of the number of bleb per cell was then monitored on non-adhesive substrate by video microscopy (see text). Theoretically,  $n_b$  was calculated from Eq. [6] by fixing  $A_c = 0$  (no spreading) and setting the initial membrane area to its value for a fully adhered cell:  $A_m = k_1/(k_1 + k_2)$ . Parameters are  $\varepsilon / k_2 = 1500 \mu\text{m}^2 t$ ,  $k_1 = 3.4k_2$ ,  $\tau - m/2 = \tau_c = 3.5 \text{ min}$ ,  $\gamma_b = -0.1\varepsilon$ ,  $\beta\varepsilon = 50$  and  $A_{b0} = \varepsilon / 4k_2$ . The red dots show the different initial condition for the adhesion kinetics of blebbing cells in Fig. 3

### ***Spreading of a blebbing cell***

Our experimental setup allows us to quantify the effect of blebs on cell spreading, since the number of bleb per cell can be controlled by changing the incubation time, as show in Appendix Fig. 2. We observe that blebs have a strong effect on the initial stage of cell spreading. Blebbing cells near a substrate only start spreading after a lag time that increases with the initial number of blebs. We propose that blebs act as pressurized

cushions preventing strong cortex adhesion to the extracellular matrix. Part of this effect can be compared to the Helfrich repulsion of a thermally fluctuating membrane near a substrate (275), although the “fluctuations” of a blebbing cell are actively driven (by the acto-myosin cortex) and have a well-defined size  $S_b$  (Eq. [3]). It is in principle quite complicated to compute the effect of blebs on cell adhesion, since in addition to the “air bag” effect discussed above; some blebs near the substrate are seen to retract as they would in the absence of substrate, while others maintain a stable adhesion. Here, we use a very simple mean-field approach, and assume that the effective adhesion energy is reduced (linearly) when blebs are present:  $\varepsilon_{eff} = \varepsilon(1 - n_b / n_b^*)$ , where  $n_b^*$  is the bleb occupancy that prevents adhesion. This fairly crude approximation manages to qualitatively reproduce the experimental observations, as we show below. We numerically solve Eq. [6] for different initial conditions corresponding to different incubation times (the red dots shown in Appendix Fig. 2), and obtain the spreading kinetics shown in Appendix Fig. 3. The duration of the lag phase observed in the experiment are reproduced by choosing  $n_b^* = 1/4$ , meaning that the cell is prevented from adhering to the substrate when blebs covered about 25% of its surface.



**Appendix Fig. 3** Spreading kinetics for different incubation times, increasing from zero (lighter grey) to infinity (black). Incubation times are shown in Fig. 2. Parameters are the same as in Fig. 2, with  $\alpha_b = 4$ .

## 10 Bibliography

1. Cuvelier, D., Thery, M., Chu, Y.S., Dufour, S., Thiery, J.P., Bornens, M., Nassoy, P., and Mahadevan, L. The universal dynamics of cell spreading. *Curr Biol* 17, 694, 2007.
2. Sengupta, K., Aranda-Espinoza, H., Smith, L., Janmey, P., and Hammer, D. Spreading of neutrophils: from activation to migration. *Biophys J* 91, 4638, 2006.
3. Cuvelier, D., Rossier, O., Bassereau, P., and Nassoy, P. Micropatterned "adherent/repellent" glass surfaces for studying the spreading kinetics of individual red blood cells onto protein-decorated substrates. *Eur Biophys J* 32, 342, 2003.
4. Hategan, A., Sengupta, K., Kahn, S., Sackmann, E., and Discher, D.E. Topographical pattern dynamics in passive adhesion of cell membranes. *Biophys J* 87, 3547, 2004.
5. Dobereiner, H.G., Dubin-Thaler, B., Giannone, G., Xenias, H.S., and Sheetz, M.P. Dynamic phase transitions in cell spreading. *Phys Rev Lett* 93, 108105, 2004.
6. Sheetz, M., Dubin-Thaler, B., Giannone, G., Jiang, G., and Dobereiner, H.-G. Functional phases in cell attachment and spreading. In: Wedlich, D., ed. *Cell Migration*. Weinheim: Wiley-VCH Verlag GmbH & Co., 2005.
7. Weijer, C.J. Collective cell migration in development. *J Cell Sci* 122, 3215, 2009.
8. Bronner-Fraser, M. Neural crest cell formation and migration in the developing embryo. *Faseb J* 8, 699, 1994.
9. Tucker, R.P. Abnormal neural crest cell migration after the in vivo knockdown of tenascin-C expression with morpholino antisense oligonucleotides. *Dev Dyn* 222, 115, 2001.
10. Hathaway, H.J., and Shur, B.D. Cell surface beta 1,4-galactosyltransferase functions during neural crest cell migration and neurulation in vivo. *J Cell Biol* 117, 369, 1992.
11. Taneyhill, L.A., and Bronner-Fraser, M. Dynamic alterations in gene expression after Wnt-mediated induction of avian neural crest. *Mol Biol Cell* 16, 5283, 2005.
12. Coles, E.G., Taneyhill, L.A., and Bronner-Fraser, M. A critical role for Cadherin6B in regulating avian neural crest emigration. *Dev Biol* 312, 533, 2007.
13. Tucker, R.P. Antisense knockdown of the beta1 integrin subunit in the chicken embryo results in abnormal neural crest cell development. *Int J Biochem Cell Biol* 36, 1135, 2004.

14. Sasai, N., Mizuseki, K., and Sasai, Y. Requirement of FoxD3-class signaling for neural crest determination in *Xenopus*. *Development* 128, 2525, 2001.
15. Alberts, B. *Molecular biology of the cell*. New York: Garland Science, 2002.
16. Yoshida, B.A., Chekmareva, M.A., Wharam, J.F., Kadkhodaian, M., Stadler, W.M., Boyer, A., Watabe, K., Nelson, J.B., and Rinker-Schaeffer, C.W. Prostate cancer metastasis-suppressor genes: a current perspective. *In Vivo* 12, 49, 1998.
17. Yoshida, B.A., Sokoloff, M.M., Welch, D.R., and Rinker-Schaeffer, C.W. Metastasis-suppressor genes: a review and perspective on an emerging field. *J Natl Cancer Inst* 92, 1717, 2000.
18. Weigelt, B., Peterse, J.L., and van 't Veer, L.J. Breast cancer metastasis: markers and models. *Nat Rev Cancer* 5, 591, 2005.
19. Cancer Research Funding. National Cancer Institute, 2008, pp. [www.cancer.gov/cancertopics/factsheets/NCI/research-funding](http://www.cancer.gov/cancertopics/factsheets/NCI/research-funding).
20. Delves, P.J., and Roitt, I.M. The immune system. First of two parts. *N Engl J Med* 343, 37, 2000.
21. Luster, A.D., Alon, R., and von Andrian, U.H. Immune cell migration in inflammation: present and future therapeutic targets. *Nat Immunol* 6, 1182, 2005.
22. Kelly, M., Hwang, J.M., and Kubes, P. Modulating leukocyte recruitment in inflammation. *J Allergy Clin Immunol* 120, 3, 2007.
23. Majno, G., and Joris, I. *Cells, tissues, and disease: principles of general pathology*. Cambridge, Mass.: Blackwell Science, 1996.
24. Matsumoto, T., Abe, H., Ohashi, T., Kato, Y., and Sato, M. Local elastic modulus of atherosclerotic lesions of rabbit thoracic aortas measured by pipette aspiration method. *Physiol Meas* 23, 635, 2002.
25. Stroka, K.M., and Aranda-Espinoza, H. Neutrophils display biphasic relationship between migration and substrate stiffness. *Cell Motil Cytoskeleton* 66, 328, 2009.
26. Norman, L., Bragues, J., Sengupta, K., Sens, P., and Aranda-Espinoza, H. Cell blebbing and membrane area homeostasis in spreading and retracting cells. (Under Review).
27. Norman, L., Sengupta, K., and Aranda-Espinoza, H. Blebbing dynamics during endothelial cell spreading. (Under Review), 2010.

28. Dubin-Thaler, B.J., Giannone, G., Dobereiner, H.G., and Sheetz, M.P. Nanometer analysis of cell spreading on matrix-coated surfaces reveals two distinct cell states and STEPs. *Biophys J* 86, 1794, 2004.
29. Lammermann, T., Bader, B.L., Monkley, S.J., Worbs, T., Wedlich-Soldner, R., Hirsch, K., Keller, M., Forster, R., Critchley, D.R., Fassler, R., and Sixt, M. Rapid leukocyte migration by integrin-independent flowing and squeezing. *Nature* 453, 51, 2008.
30. Gupton, S.L., and Waterman-Storer, C.M. Spatiotemporal feedback between actomyosin and focal-adhesion systems optimizes rapid cell migration. *Cell* 125, 1361, 2006.
31. Pollard, T.D., and Borisy, G.G. Cellular motility driven by assembly and disassembly of actin filaments. *Cell* 112, 453, 2003.
32. Critchley, D.R., Holt, M.R., Barry, S.T., Priddle, H., Hemmings, L., and Norman, J. Integrin-mediated cell adhesion: the cytoskeletal connection. *Biochem Soc Symp* 65, 79, 1999.
33. Wozniak, M.A., Modzelewska, K., Kwong, L., and Keely, P.J. Focal adhesion regulation of cell behavior. *Biochim Biophys Acta* 1692, 103, 2004.
34. Kaverina, I., Krylyshkina, O., and Small, J.V. Regulation of substrate adhesion dynamics during cell motility. *Int J Biochem Cell Biol* 34, 746, 2002.
35. Lauffenburger, D.A., and Horwitz, A.F. Cell migration: a physically integrated molecular process. *Cell* 84, 359, 1996.
36. DiMilla, P.A., Stone, J.A., Quinn, J.A., Albelda, S.M., and Lauffenburger, D.A. Maximal migration of human smooth muscle cells on fibronectin and type IV collagen occurs at an intermediate attachment strength. *J Cell Biol* 122, 729, 1993.
37. Huttenlocher, A., Ginsberg, M.H., and Horwitz, A.F. Modulation of cell migration by integrin-mediated cytoskeletal linkages and ligand-binding affinity. *J Cell Biol* 134, 1551, 1996.
38. Palecek, S.P., Loftus, J.C., Ginsberg, M.H., Lauffenburger, D.A., and Horwitz, A.F. Integrin-ligand binding properties govern cell migration speed through cell-substratum adhesiveness. *Nature* 385, 537, 1997.
39. Pelham, R.J., Jr., and Wang, Y. Cell locomotion and focal adhesions are regulated by substrate flexibility. *Proc Natl Acad Sci U S A* 94, 13661, 1997.

40. Wang, H.B., Dembo, M., Hanks, S.K., and Wang, Y. Focal adhesion kinase is involved in mechanosensing during fibroblast migration. *Proc Natl Acad Sci U S A* 98, 11295, 2001.
41. Yeung, T., Georges, P.C., Flanagan, L.A., Marg, B., Ortiz, M., Funaki, M., Zahir, N., Ming, W., Weaver, V., and Janmey, P.A. Effects of substrate stiffness on cell morphology, cytoskeletal structure, and adhesion. *Cell Motil Cytoskeleton* 60, 24, 2005.
42. Doyle, A.D., Wang, F.W., Matsumoto, K., and Yamada, K.M. One-dimensional topography underlies three-dimensional fibrillar cell migration. *J Cell Biol* 184, 481, 2009.
43. DiMilla, P.A., Barbee, K., and Lauffenburger, D.A. Mathematical model for the effects of adhesion and mechanics on cell migration speed. *Biophys J* 60, 15, 1991.
44. Gardel, M.L., Sabass, B., Ji, L., Danuser, G., Schwarz, U.S., and Waterman, C.M. Traction stress in focal adhesions correlates biphasically with actin retrograde flow speed. *J Cell Biol* 183, 999, 2008.
45. Engler, A.J., Sen, S., Sweeney, H.L., and Discher, D.E. Matrix elasticity directs stem cell lineage specification. *Cell* 126, 677, 2006.
46. Janmey, P.A., Winer, J.P., Murray, M.E., and Wen, Q. The hard life of soft cells. *Cell Motil Cytoskeleton* 66, 597, 2009.
47. Norman, L.L., Stroka, K.M., and Aranda-Espinoza, H. Guiding Axons in the Central Nervous System: A Tissue-Engineering Approach. *Tissue Eng Part B Rev*, 2009.
48. Heath, J.P., and Peachey, L.D. Morphology of fibroblasts in collagen gels: a study using 400 keV electron microscopy and computer graphics. *Cell Motil Cytoskeleton* 14, 382, 1989.
49. Cukierman, E., Pankov, R., Stevens, D.R., and Yamada, K.M. Taking cell-matrix adhesions to the third dimension. *Science* 294, 1708, 2001.
50. Craig, A.M., and Banker, G. Neuronal polarity. *Annu Rev Neurosci* 17, 267, 1994.
51. de Lima, A.D., Merten, M.D., and Voigt, T. Neuritic differentiation and synaptogenesis in serum-free neuronal cultures of the rat cerebral cortex. *J Comp Neurol* 382, 230, 1997.
52. Dehmelt, L., Smart, F.M., Ozer, R.S., and Halpain, S. The role of microtubule-associated protein 2c in the reorganization of microtubules and lamellipodia during neurite initiation. *J Neurosci* 23, 9479, 2003.

53. Dotti, C.G., Sullivan, C.A., and Banker, G.A. The establishment of polarity by hippocampal neurons in culture. *J Neurosci* 8, 1454, 1988.
54. Dent, E.W., Kwiatkowski, A.V., Mebane, L.M., Philippar, U., Barzik, M., Rubinson, D.A., Gupton, S., Van Veen, J.E., Furman, C., Zhang, J., Alberts, A.S., Mori, S., and Gertler, F.B. Filopodia are required for cortical neurite initiation. *Nat Cell Biol* 9, 1347, 2007.
55. Donkelaar, H., Lammens, M., Hori, A., and Cremers, C. *Clinical neuroembryology: Development and developmental disorders of the human central nervous system*. New York: Springer, 2006.
56. Kriegstein, K. *Cell death in the nervous system*. New York: Springer Science and Business, 2006.
57. Bush, T.G., Puvanachandra, N., Horner, C.H., Polito, A., Ostenfeld, T., Svendsen, C.N., Mucke, L., Johnson, M.H., and Sofroniew, M.V. Leukocyte infiltration, neuronal degeneration, and neurite outgrowth after ablation of scar-forming, reactive astrocytes in adult transgenic mice. *Neuron* 23, 297, 1999.
58. Faulkner, J.R., Herrmann, J.E., Woo, M.J., Tansey, K.E., Doan, N.B., and Sofroniew, M.V. Reactive astrocytes protect tissue and preserve function after spinal cord injury. *J Neurosci* 24, 2143, 2004.
59. Myer, D.J., Gurkoff, G.G., Lee, S.M., Hovda, D.A., and Sofroniew, M.V. Essential protective roles of reactive astrocytes in traumatic brain injury. *Brain* 129, 2761, 2006.
60. Silver, J., and Miller, J.H. Regeneration beyond the glial scar. *Nat Rev Neurosci* 5, 146, 2004.
61. Fawcett, J.W. In: Bahr, M., ed. *Brain Repair*. New York: Springer Science+Business, 2006.
62. Rhodes, K., Moon, L., and Fawcett, J. Inhibiting cell proliferation during formation of the glial scar: Effects on axon regeneration in the CNS. *Neuroscience* 120, 41, 2003.
63. Ridet, J., Malhotra, S., Privat, A., and Gage, F. Reactive astrocytes: cellular and molecular cues to biological function. *TRENDS IN NEUROSCIENCES* 20, 570, 1997.
64. Fitch, M.T., and Silver, J. In: Sanders, N.R., and Dziegielewska, K.M., eds. *Degeneration and Regeneration in the Nervous System*. Australia: Harwood Academic Publishers, 2000.

65. Saltzman, W.M. *Tissue Engineering: Principles for the design of replacement organs and tissues*. New York: Oxford University Press, 2004.
66. Saha, K., Keung, A.J., Irwin, E.F., Li, Y., Little, L., Schaffer, D.V., and Healy, K.E. Substrate modulus directs neural stem cell behavior. *Biophys J* 95, 4426, 2008.
67. Leach, J.B., Brown, X.Q., Jacot, J.G., Dimilla, P.A., and Wong, J.Y. Neurite outgrowth and branching of PC12 cells on very soft substrates sharply decreases below a threshold of substrate rigidity. *J Neural Eng* 4, 26, 2007.
68. Gunn, J.W., Turner, S.D., and Mann, B.K. Adhesive and mechanical properties of hydrogels influence neurite extension. *J Biomed Mater Res A* 72, 91, 2005.
69. Greene, L.A. Nerve growth factor prevents the death and stimulates the neuronal differentiation of clonal PC12 pheochromocytoma cells in serum-free medium. *J Cell Biol* 78, 747, 1978.
70. Greene, L.A., and Tischler, A.S. Establishment of a noradrenergic clonal line of rat adrenal pheochromocytoma cells which respond to nerve growth factor. *Proc Natl Acad Sci U S A* 73, 2424, 1976.
71. Georges, P.C., Miller, W.J., Meaney, D.F., Sawyer, E.S., and Janmey, P.A. Matrices with compliance comparable to that of brain tissue select neuronal over glial growth in mixed cortical cultures. *Biophys J* 90, 3012, 2006.
72. Willits, R.K., and Skornia, S.L. Effect of collagen gel stiffness on neurite extension. *J Biomater Sci Polym Ed* 15, 1521, 2004.
73. Balgude, A.P., Yu, X., Szymanski, A., and Bellamkonda, R.V. Agarose gel stiffness determines rate of DRG neurite extension in 3D cultures. *Biomaterials* 22, 1077, 2001.
74. Cullen, D.K., Lessing, M.C., and LaPlaca, M.C. Collagen-dependent neurite outgrowth and response to dynamic deformation in three-dimensional neuronal cultures. *Ann Biomed Eng* 35, 835, 2007.
75. Flanagan, L.A., Ju, Y.E., Marg, B., Osterfield, M., and Janmey, P.A. Neurite branching on deformable substrates. *Neuroreport* 13, 2411, 2002.
76. Goldner, J.S., Bruder, J.M., Li, G., Gazzola, D., and Hoffman-Kim, D. Neurite bridging across micropatterned grooves. *Biomaterials* 27, 460, 2006.
77. Gomez, N., Lu, Y., Chen, S., and Schmidt, C.E. Immobilized nerve growth factor and microtopography have distinct effects on polarization versus axon elongation in hippocampal cells in culture. *Biomaterials* 28, 271, 2007.

78. Haq, F., Keith, C., and Zhang, G. Neurite development in PC12 cells on flexible micro-textured substrates under cyclic stretch. *Biotechnol Prog* 22, 133, 2006.
79. Houchin-Ray, T., Swift, L.A., Jang, J.H., and Shea, L.D. Patterned PLG substrates for localized DNA delivery and directed neurite extension. *Biomaterials* 28, 2603, 2007.
80. Li, N., and Folch, A. Integration of topographical and biochemical cues by axons during growth on microfabricated 3-D substrates. *Exp Cell Res* 311, 307, 2005.
81. Song, M., and Uhrich, K.E. Optimal micropattern dimensions enhance neurite outgrowth rates, lengths, and orientations. *Ann Biomed Eng* 35, 1812, 2007.
82. Woerly, S. Restorative surgery of the central nervous system by means of tissue engineering using NeuroGel implants. *Neurosurg Rev* 23, 59, 2000.
83. Bhang, S.H., Lim, J.S., Choi, C.Y., Kwon, Y.K., and Kim, B.S. The behavior of neural stem cells on biodegradable synthetic polymers. *J Biomater Sci Polym Ed* 18, 223, 2007.
84. Han, D.W., Sub Lee, M., Park, B.J., Kim, J.K., and Park, J.C. Enhanced neurite outgrowth of rat neural cortical cells on surface-modified films of poly(lactic-co-glycolic acid). *Biotechnol Lett* 27, 53, 2005.
85. Lee, S.J., Khang, G., Lee, Y.M., and Lee, H.B. The effect of surface wettability on induction and growth of neurites from the PC-12 cell on a polymer surface. *Journal of Colloid and Interface Science* 259, 228, 2003.
86. Hayman, M.W., Smith, K.H., Cameron, N.R., and Przyborski, S.A. Enhanced neurite outgrowth by human neurons grown on solid three-dimensional scaffolds. *Biochem Biophys Res Commun* 314, 483, 2004.
87. Lin, P.W., Wu, C.C., Chen, C.H., Ho, H.O., Chen, Y.C., and Sheu, M.T. Characterization of cortical neuron outgrowth in two- and three-dimensional culture systems. *J Biomed Mater Res B Appl Biomater* 75, 146, 2005.
88. Kofron, C.M., Fong, V.J., and Hoffman-Kim, D. Neurite outgrowth at the interface of 2D and 3D growth environments. *J Neural Eng* 6, 16002, 2009.
89. Willerth, S.M., and Sakiyama-Elbert, S.E. Approaches to neural tissue engineering using scaffolds for drug delivery. *Adv Drug Deliv Rev* 59, 325, 2007.
90. Saffell, J., Williams, E., Mason, I., Walsh, F., and Doherty, P. Expression of a dominant negative FGF receptor inhibits axonal growth and FGF receptor phosphorylation stimulated by CAMs. *Neuron* 18, 231, 1997.

91. Willlms, E., Furness, J., Waslsh, F., and Doherty, P. Activation of the FGF receptro underlies neurite outgrowth stimulated by L1, N-CAM, and N-Cadherin. *Neuron* 13, 583, 1994.
92. Williams, E., Williams, G., Howell, F., Skaper, S., Walsh, F., and Doherty, P. Identification of an N-cadherin motif that can interact with the fibroblast growth factor receptor and is required for axonal growth. *J Bio Chem* 276, 43879, 2001.
93. Sanchez-Heras, E., Howell, F., Williams, G., and Doherty, P. The fibroblast growth factor receptor acid box is essential for interactions with N-cadherin and all of the major isoforms of neural cell adhesion molecule. *J Bio Chem* 281, 35208, 2006.
94. Guan, K.L., and Rao, Y. Signaling mechanisms mediating neuronal responses to guidance cues. *Nature Reviews Neuroscience* 4, 941, 2003.
95. Maskery, S., and Shinbrot, T. Deterministic and stochastic elements of axonal guidance. *Ann Rev Bio Eng* 7, 187, 2005.
96. Pasterkamp, R., and Kolodkin, A. Semaphorin junction: making tracks toward neural connectivity. *Curr Opinion Neurobiology* 13, 79, 2003.
97. Kapfhammer, J.P., and Raper, J.A. Collapse of growth cone structure on contact with specific neurites in culture. *J Neurosci* 7, 201, 1987.
98. Kidd, T., Bland, K.S., and Goodman, C.S. Slit is the midline repellent for the robo receptor in *Drosophila*. *Cell* 96, 785, 1999.
99. Kennedy, T.E. Cellular mechanisms of netrin function: long-range and short-range actions. *Biochem Cell Biol* 78, 569, 2000.
100. Merz, D., and Culotti, J. Genetic analysis of growth cone migrations in *Caenorhabditis elegans*. *J Neurobiology* 44, 281, 2000.
101. Knoll, B., and Drescher, U. Ephrin-As as receptors in topographic projections. *Trends Neurosci* 25, 145, 2002.
102. Wilkinson, D.G. Multiple roles of EPH receptors and ephrins in neural development. *Nat Rev Neurosci* 2, 155, 2001.
103. Geller, H.M., and Fawcett, J.W. Building a bridge: engineering spinal cord repair. *Exp Neurol* 174, 125, 2002.
104. Powell, E.M., Sobarzo, M.R., and Saltzman, W.M. Controlled release of nerve growth factor from a polymeric implant. *Brain Res* 515, 309, 1990.

105. Taylor, S.J., Rosenzweig, E.S., McDonald, J.W., 3rd, and Sakiyama-Elbert, S.E. Delivery of neurotrophin-3 from fibrin enhances neuronal fiber sprouting after spinal cord injury. *J Control Release* 113, 226, 2006.
106. Cajal, S.R. A quelle époque apparaissent les expansions des cellules nerveuses de la moelle epiniere du poulet? *Anatomomischer Anzeiger* 21-22, 609, 1890.
107. Dent, E., and Gertler, F. Cytoskeletal dynamics and transport in growth cone motility and axon guidance. *Neuron* 40, 209, 2003.
108. Charras, G., Hu, C., Coughlin, M., and Mitchison, T. Reassembly of contractile actin cortex in cell blebs. *J Cell Biology* 175, 477, 2006.
109. Wittmann, T., Bokoch, G., and Waterman-Storer, C. Regulation of leading edge microtubule and actin dynamics downstream of Rac1. *J Cell Biology* 161, 845, 2003.
110. Wiggin, G.R., Fawcett, J.P., and Pawson, T. Polarity proteins in axon specification and synaptogenesis. *Dev Cell* 8, 803, 2005.
111. Shi, S.H., Jan, L.Y., and Jan, Y.N. Hippocampal neuronal polarity specified by spatially localized mPar3/mPar6 and PI 3-kinase activity. *Cell* 112, 63, 2003.
112. Arimura, N., and Kaibuchi, K. Neuronal polarity: from extracellular signals to intracellular mechanisms. *Nat Rev Neurosci* 8, 194, 2007.
113. Houweling, D.A., Lankhorst, A.J., Gispen, W.H., Bar, P.R., and Joosten, E.A. Collagen containing neurotrophin-3 (NT-3) attracts regrowing injured corticospinal axons in the adult rat spinal cord and promotes partial functional recovery. *Exp Neurol* 153, 49, 1998.
114. Blesch, A., and Tuszynski, M.H. Transient growth factor delivery sustains regenerated axons after spinal cord injury. *J Neurosci* 27, 10535, 2007.
115. Offenhausser, A., Bocker-Meffert, S., Decker, T., Helpenstein, R., Gasteier, P., Groll, J., Moller, M., Reska, A., Schafer, S., Schulte, P., and Vogt-Eisele, A. Microcontact printing of proteins for neuronal cell guidance. *Soft Matter* 3, 290, 2007.
116. Vogt, A.K., Lauer, L., Knoll, W., and Offenhausser, A. Micropatterned substrates for the growth of functional neuronal networks of defined geometry. *Biotechnol Prog* 19, 1562, 2003.
117. Norman, L., Oetama, R., Dembo, M., Byfield, F., Hammer, D., Levitan, I., and H, a.A.-E. Modification of cellular cholesterol content affects traction force, adhesion and cell spreading. *Cellular and Molecular Bioengineering* (DOI # 10.1007/s12195-010-0119x), 2010.

118. Curtis, A.S. The Mechanism Of Adhesion Of Cells To Glass. A Study By Interference Reflection Microscopy. *J Cell Biol* 20, 199, 1964.
119. Gingell, D., and Todd, I. Interference reflection microscopy. A quantitative theory for image interpretation and its application to cell-substratum separation measurement. *Biophys J* 26, 507, 1979.
120. Axelrod, D. Total internal reflection fluorescence microscopy in cell biology. *Methods Enzymol* 361, 1, 2003.
121. Jacobson, C., Schnapp, B., and Banker, G.A. A change in the selective translocation of the Kinesin-1 motor domain marks the initial specification of the axon. *Neuron* 49, 797, 2006.
122. Radmacher, M., Fritz, M., Kacher, C.M., Cleveland, J.P., and Hansma, P.K. Measuring the viscoelastic properties of human platelets with the atomic force microscope. *Biophys J* 70, 556, 1996.
123. Binnig, G., Quate, C.F., and Gerber, C. Atomic force microscope. *Phys Rev Lett* 56, 930, 1986.
124. Norman, L., and H, a.A.-E. Cortical neuron outgrowth is insensitive to substrate stiffness. (Under Review), 2010.
125. Drake, B., Prater, C.B., Weisenhorn, A.L., Gould, S.A., Albrecht, T.R., Quate, C.F., Cannell, D.S., Hansma, H.G., and Hansma, P.K. Imaging crystals, polymers, and processes in water with the atomic force microscope. *Science* 243, 1586, 1989.
126. Franze, K., Gerdemann, J., Weick, M., Betz, T., Pawlizak, S., Lakadamyali, M., Bayer, J., Rillich, K., Gogler, M., Lu, Y.B., Reichenbach, A., Janmey, P., and Kas, J. Neurite branch retraction is caused by a threshold-dependent mechanical impact. *Biophys J* 97, 1883, 2009.
127. Lu, Y.B., Franze, K., Seifert, G., Steinhauser, C., Kirchhoff, F., Wolburg, H., Guck, J., Janmey, P., Wei, E.Q., Kas, J., and Reichenbach, A. Viscoelastic properties of individual glial cells and neurons in the CNS. *Proc Natl Acad Sci U S A* 103, 17759, 2006.
128. Elkin, B.S., Azeloglu, E.U., Costa, K.D., and Morrison, B., 3rd. Mechanical heterogeneity of the rat hippocampus measured by atomic force microscope indentation. *J Neurotrauma* 24, 812, 2007.
129. Viani, M.B., Pietrasanta, L.I., Thompson, J.B., Chand, A., Gebeshuber, I.C., Kindt, J.H., Richter, M., Hansma, H.G., and Hansma, P.K. Probing protein-protein interactions in real time. *Nat Struct Biol* 7, 644, 2000.

130. McAllister, C., Karymov, M.A., Kawano, Y., Lushnikov, A.Y., Mikheikin, A., Uversky, V.N., and Lyubchenko, Y.L. Protein interactions and misfolding analyzed by AFM force spectroscopy. *J Mol Biol* 354, 1028, 2005.
131. Florin, E.L., Moy, V.T., and Gaub, H.E. Adhesion forces between individual ligand-receptor pairs. *Science* 264, 415, 1994.
132. Charras, G., and Paluch, E. Blebs lead the way: how to migrate without lamellipodia. *Nat Rev Mol Cell Biol* 9, 730, 2008.
133. Hoglund, A.S. The arrangement of microfilaments and microtubules in the periphery of spreading fibroblasts and glial cells. *Tissue Cell* 17, 649, 1985.
134. Bereiter-Hahn, J., Luck, M., Miebach, T., Stelzer, H.K., and Voth, M. Spreading of trypsinized cells: cytoskeletal dynamics and energy requirements. *J Cell Sci* 96 (Pt 1), 171, 1990.
135. Cunningham, C.C. Actin polymerization and intracellular solvent flow in cell surface blebbing. *J Cell Biol* 129, 1589, 1995.
136. Erickson, C.A., and Trinkaus, J.P. Microvilli and blebs as sources of reserve surface membrane during cell spreading. *Exp Cell Res* 99, 375, 1976.
137. Laster, S.M., and Mackenzie, J.M., Jr. Bleb formation and F-actin distribution during mitosis and tumor necrosis factor-induced apoptosis. *Microsc Res Tech* 34, 272, 1996.
138. Boucrot, E., and Kirchhausen, T. Endosomal recycling controls plasma membrane area during mitosis. *Proc Natl Acad Sci U S A* 104, 7939, 2007.
139. Blaser, H., Reichman-Fried, M., Castanon, I., Dumstrei, K., Marlow, F.L., Kawakami, K., Solnica-Krezel, L., Heisenberg, C.P., and Raz, E. Migration of zebrafish primordial germ cells: a role for myosin contraction and cytoplasmic flow. *Dev Cell* 11, 613, 2006.
140. Langridge, P.D., and Kay, R.R. Blebbing of Dictyostelium cells in response to chemoattractant. *Exp Cell Res* 312, 2009, 2006.
141. Zhao, M., Song, B., Pu, J., Wada, T., Reid, B., Tai, G., Wang, F., Guo, A., Walczysko, P., Gu, Y., Sasaki, T., Suzuki, A., Forrester, J.V., Bourne, H.R., Devreotes, P.N., McCaig, C.D., and Penninger, J.M. Electrical signals control wound healing through phosphatidylinositol-3-OH kinase-gamma and PTEN. *Nature* 442, 457, 2006.
142. Charras, G.T., Coughlin, M., Mitchison, T.J., and Mahadevan, L. Life and times of a cellular bleb. *Biophys J* 94, 1836, 2008.

143. Charras, G.T., Yarrow, J.C., Horton, M.A., Mahadevan, L., and Mitchison, T.J. Non-equilibration of hydrostatic pressure in blebbing cells. *Nature* 435, 365, 2005.
144. Dai, J., and Sheetz, M.P. Membrane tether formation from blebbing cells. *Biophys J* 77, 3363, 1999.
145. Merkel, R., Simson, R., Simson, D.A., Hohenadl, M., Boulbitch, A., Wallraff, E., and Sackmann, E. A micromechanic study of cell polarity and plasma membrane cell body coupling in *Dictyostelium*. *Biophys J* 79, 707, 2000.
146. Dubin-Thaler, B.J., Hofman, J.M., Cai, Y., Xenias, H., Spielman, I., Shneidman, A.V., David, L.A., Dobereiner, H.G., Wiggins, C.H., and Sheetz, M.P. Quantification of cell edge velocities and traction forces reveals distinct motility modules during cell spreading. *PLoS One* 3, e3735, 2008.
147. Chamaraux, F., Fache, S., Bruckert, F., and Fourcade, B. Kinetics of cell spreading. *Phys Rev Lett* 94, 158102, 2005.
148. del Pozo, M.A., Alderson, N.B., Kiosses, W.B., Chiang, H.H., Anderson, R.G., and Schwartz, M.A. Integrins regulate Rac targeting by internalization of membrane domains. *Science* 303, 839, 2004.
149. del Pozo, M.A., Balasubramanian, N., Alderson, N.B., Kiosses, W.B., Grande-Garcia, A., Anderson, R.G., and Schwartz, M.A. Phospho-caveolin-1 mediates integrin-regulated membrane domain internalization. *Nat Cell Biol* 7, 901, 2005.
150. Gauthier, N.C., Rossier, O.M., Mathur, A., Hone, J.C., and Sheetz, M.P. Plasma membrane area increases with spread area by exocytosis of a GPI-anchored protein compartment. *Mol Biol Cell* 20, 3261, 2009.
151. Balasubramanian, N., Scott, D.W., Castle, J.D., Casanova, J.E., and Schwartz, M.A. Arf6 and microtubules in adhesion-dependent trafficking of lipid rafts. *Nat Cell Biol* 9, 1381, 2007.
152. Steinman, R.M., Mellman, I.S., Muller, W.A., and Cohn, Z.A. Endocytosis and the recycling of plasma membrane. *J Cell Biol* 96, 1, 1983.
153. Grant, B.D., and Donaldson, J.G. Pathways and mechanisms of endocytic recycling. *Nat Rev Mol Cell Biol* 10, 597, 2009.
154. Macia, E., Ehrlich, M., Massol, R., Boucrot, E., Brunner, C., and Kirchhausen, T. Dynasore, a cell-permeable inhibitor of dynamin. *Dev Cell* 10, 839, 2006.
155. Sens, P., and Turner, M.S. Budded membrane microdomains as tension regulators. *Phys Rev E Stat Nonlin Soft Matter Phys* 73, 031918, 2006.

156. Morris, C.E., and Homann, U. Cell surface area regulation and membrane tension. *J Membr Biol* 179, 79, 2001.
157. Schwartz, M.A. Integrins, oncogenes, and anchorage independence. *J Cell Biol* 139, 575, 1997.
158. Kolodny, G.M. Effect of various inhibitors of readhesion of trypsinized cells in culture. *Exp Cell Res* 70, 196, 1972.
159. Deman, J.J., and Bruyneel, E.A. Thermal transitions in the adhesiveness of HeLa cells: effects of cell growth, trypsin treatment and calcium. *J Cell Sci* 27, 167, 1977.
160. Charras, G.T., Hu, C.K., Coughlin, M., and Mitchison, T.J. Reassembly of contractile actin cortex in cell blebs. *J Cell Biol* 175, 477, 2006.
161. Charras, G.T. A short history of blebbing. *J Microsc* 231, 466, 2008.
162. Keller, H., and Eggli, P. Protrusive activity, cytoplasmic compartmentalization, and restriction rings in locomoting blebbing Walker carcinosarcoma cells are related to detachment of cortical actin from the plasma membrane. *Cell Motil Cytoskeleton* 41, 181, 1998.
163. Keller, H., Rentsch, P., and Hagmann, J. Differences in cortical actin structure and dynamics document that different types of blebs are formed by distinct mechanisms. *Exp Cell Res* 277, 161, 2002.
164. Keller, H.U., and Bebie, H. Protrusive activity quantitatively determines the rate and direction of cell locomotion. *Cell Motil Cytoskeleton* 33, 241, 1996.
165. Cheung, A., Dantzig, J.A., Hollingworth, S., Baylor, S.M., Goldman, Y.E., Mitchison, T.J., and Straight, A.F. A small-molecule inhibitor of skeletal muscle myosin II. *Nat Cell Biol* 4, 83, 2002.
166. Mills, J.C., Stone, N.L., Erhardt, J., and Pittman, R.N. Apoptotic membrane blebbing is regulated by myosin light chain phosphorylation. *J Cell Biol* 140, 627, 1998.
167. Fedier, A., and Keller, H.U. Suppression of bleb formation, locomotion, and polarity of Walker carcinosarcoma cells by hypertonic media correlates with cell volume reduction but not with changes in the F-actin content. *Cell Motil Cytoskeleton* 37, 326, 1997.
168. Yoshida, K., and Soldati, T. Dissection of amoeboid movement into two mechanically distinct modes. *J Cell Sci* 119, 3833, 2006.
169. Limouze, J., Straight, A.F., Mitchison, T., and Sellers, J.R. Specificity of blebbistatin, an inhibitor of myosin II. *J Muscle Res Cell Motil* 25, 337, 2004.

170. Cai, Y., Biais, N., Giannone, G., Tanase, M., Jiang, G., Hofman, J.M., Wiggins, C.H., Silberzan, P., Buguin, A., Ladoux, B., and Sheetz, M.P. Nonmuscle myosin IIA-dependent force inhibits cell spreading and drives F-actin flow. *Biophys J* 91, 3907, 2006.
171. Wakatsuki, T., Wysolmerski, R.B., and Elson, E.L. Mechanics of cell spreading: role of myosin II. *J Cell Sci* 116, 1617, 2003.
172. Kadi, A., Pichard, V., Lehmann, M., Briand, C., Braguer, D., Marvaldi, J., Rognoni, J.B., and Luis, J. Effect of microtubule disruption on cell adhesion and spreading. *Biochem Biophys Res Commun* 246, 690, 1998.
173. Kaverina, I., Krylyshkina, O., and Small, J.V. Microtubule targeting of substrate contacts promotes their relaxation and dissociation. *J Cell Biol* 146, 1033, 1999.
174. Rhee, S., Jiang, H., Ho, C.H., and Grinnell, F. Microtubule function in fibroblast spreading is modulated according to the tension state of cell-matrix interactions. *Proc Natl Acad Sci U S A* 104, 5425, 2007.
175. Mooney, D.J., Langer, R., and Ingber, D.E. Cytoskeletal filament assembly and the control of cell spreading and function by extracellular matrix. *J Cell Sci* 108 (Pt 6), 2311, 1995.
176. Ren, X.D., Kiosses, W.B., and Schwartz, M.A. Regulation of the small GTP-binding protein Rho by cell adhesion and the cytoskeleton. *Embo J* 18, 578, 1999.
177. Rodriguez, O.C., Schaefer, A.W., Mandato, C.A., Forscher, P., Bement, W.M., and Waterman-Storer, C.M. Conserved microtubule-actin interactions in cell movement and morphogenesis. *Nat Cell Biol* 5, 599, 2003.
178. Bershadsky, A., Chausovsky, A., Becker, E., Lyubimova, A., and Geiger, B. Involvement of microtubules in the control of adhesion-dependent signal transduction. *Curr Biol* 6, 1279, 1996.
179. Enomoto, T. Microtubule disruption induces the formation of actin stress fibers and focal adhesions in cultured cells: possible involvement of the rho signal cascade. *Cell Struct Funct* 21, 317, 1996.
180. Felder, S., and Elson, E.L. Mechanics of fibroblast locomotion: quantitative analysis of forces and motions at the leading lamellas of fibroblasts. *J Cell Biol* 111, 2513, 1990.
181. Raucher, D., and Sheetz, M.P. Cell spreading and lamellipodial extension rate is regulated by membrane tension. *J Cell Biol* 148, 127, 2000.

182. Maxfield, F.R., and Tabas, I. Role of cholesterol and lipid organization in disease. *Nature* 438, 612, 2005.
183. Klausen, T.K., Hougaard, C., Hoffmann, E.K., and Pedersen, S.F. Cholesterol modulates the volume-regulated anion current in Ehrlich-Lette ascites cells via effects on Rho and F-actin. *American Journal Of Physiology Cell Physiology* 291, C757, 2006.
184. Levitan, I., Christian, A.E., Tulenko, T.N., and Rothblat, G.H. Membrane cholesterol content modulates activation of volume-regulated anion current in bovine endothelial cells. *J. Gen. Physiol.* 115, 405, 2000.
185. Romanenko, V.G., Rothblat, G.H., and Levitan, I. Modulation of endothelial inward-rectifier K<sup>+</sup> current by optical isomers of cholesterol. *Biophysical Journal* 83, 3211, 2002.
186. Romanenko, V.G., Rothblat, G.H., and Levitan, I. Sensitivity of volume-regulated anion current to cholesterol structural analogues. *Journal of General Physiology* 123, 77, 2004.
187. Lundbaek, J.A., Birn, P., Girshman, J., Hansen, A.J., and Andersen, O.S. Membrane stiffness and channel function. *Biochemistry* 35, 3825, 1996.
188. Levitan, I., and Gooch, K.J. Lipid rafts in membrane-cytoskeleton interactions and control of cellular biomechanics: actions of oxLDL. *Antioxid Redox Signal* 9, 1519, 2007.
189. Byfield, F.J., Aranda-Espinoza, H., Romanenko, V.G., Rothblat, G.H., and Levitan, I. Cholesterol depletion increases membrane stiffness of aortic endothelial cells. *Biophysical Journal* 87, 3336, 2004.
190. Chen, M., Mason, R.P., and Tulenko, T.N. Atherosclerosis Alters The Composition, Structure And Function Of Arterial Smooth-Muscle Cell Plasma-Membranes. *Biochimica Et Biophysica Acta-Molecular Basis Of Disease* 1272, 101, 1995.
191. Needham, D., and Nunn, R.S. Elastic-deformation and failure of lipid bilayer-membranes containing cholesterol. *Biophysical Journal* 58, 997, 1990.
192. Byfield, F.J., Tikku, S., Rothblat, G.H., Gooch, K.J., and Levitan, I. OxLDL increases endothelial stiffness, force generation, and network formation. *Journal Of Lipid Research* 47, 715, 2006.
193. Sun, M., Northup, N., Marga, F., Huber, T., Byfield, F.J., Levitan, I., and Forgacs, G. The effect of cellular cholesterol on membrane-cytoskeleton adhesion. *Journal of Cell Science* 120, 2223, 2007.

194. Kowalsky, G.B., Byfield, F.J., and Levitan, I. oxLDL facilitates flow-induced realignment of aortic endothelial cells. *Am J Physiol Cell Physiol* 295, C332, 2008.
195. Kwik, J., Boyle, S., Fooksman, D., Margolis, L., Sheetz, M.P., and Edidin, M. Membrane cholesterol, lateral mobility, and the phosphatidylinositol 4,5-bisphosphate-dependent organization of cell actin. *Pro Nat Acad Sci U S A* 100, 13964, 2003.
196. Pourati, J., Maniotis, A., Spiegel, D., Schaffer, J.L., Butler, J.P., Fredberg, J.J., Ingber, D.E., Stamenovic, D., and Wang, N. Is cytoskeletal tension a major determinant of cell deformability in adherent endothelial cells? *American Journal of Physiology Cell Physiology* 43, C1283, 1998.
197. Sato, M., Theret, D.P., Wheeler, L.T., Ohshima, N., and Nerem, R.M. Application of the micropipette technique to the measurement of cultured porcine aortic endothelial-cell viscoelastic properties. *Journal of Biomechanical Engineering* 112, 263, 1990.
198. Galbraith, C.G., and Sheetz, M.P. A micromachined device provides a new bend on fibroblast traction forces. *Pro Nat Acad Sci U S A* 94, 9114, 1997.
199. Corvera, S., DiBonaventura, C., and Shpetner, H.S. Cell confluence-dependent remodeling of endothelial membranes mediated by cholesterol. *Journal Of Biological Chemistry* 275, 31414, 2000.
200. Shibamoto, S., Hayakawa, M., Takeuchi, K., Hori, T., Oku, N., Miyazawa, K., Kitamura, N., Takeichi, M., and Ito, F. Tyrosine Phosphorylation Of Beta-Catenin And Plakoglobin Enhanced By Hepatocyte Growth-Factor And Epidermal Growth-Factor In Human Carcinoma-Cells. *Cell Adhesion And Communication* 1, 295, 1994.
201. Ukropec, J.A., Hollinger, M.K., Salva, S.M., and Woolkalis, M.J. SHP2 association with VE-cadherin complexes in human endothelial cells is regulated by thrombin. *Journal Of Biological Chemistry* 275, 5983, 2000.
202. Ramprasad, O.G., Srinivas, G., Rao, K.S., Joshi, P., Thiery, J.P., Dufour, S., and Pande, G. Changes in cholesterol levels in the plasma membrane modulate cell signaling and regulate cell adhesion and migration on fibronectin. *Cell Motility And The Cytoskeleton* 64, 199, 2007.
203. Wang, Y.L., and Pelham, R.J. Preparation of a flexible, porous polyacrylamide substrate for mechanical studies of cultured cells. *Molecular Motors And The Cytoskeleton*, Pt B, 1998, pp. 489-496.
204. Reinhart-King, C.A., Dembo, M., and Hammer, D.A. Endothelial cell traction forces on RGD-derivatized polyacrylamide substrata. *Langmuir* 19, 1573, 2003.
205. Christian, A.E., Haynes, M.P., Phillips, M.C., and Rothblat, G.H. Use of cyclodextrins for manipulating cellular cholesterol content. *J. Lipid Res.* 38, 2264, 1997.

206. Balaban, N.Q., Schwarz, U.S., Riveline, D., Goichberg, P., Tzur, G., Sabanay, I., Mahalu, D., Safran, S., Bershadsky, A., Addadi, L., and Geiger, B. Force and focal adhesion assembly: a close relationship studied using elastic micropatterned substrates. *Nature Cell Biology* 3, 466, 2001.
207. Butler, J.P., Tolic-Norrelykke, I.M., Fabry, B., and Fredberg, J.J. Traction fields, moments, and strain energy that cells exert on their surroundings. *American Journal Of Physiology-Cell Physiology* 282, C595, 2002.
208. Dembo, M., and Wang, Y.L. Stresses at the cell-to-substrate interface during locomotion of fibroblasts. *Biophys. J.* 76, 2307, 1999.
209. Tan, J.L., Tien, J., Pirone, D.M., Gray, D.S., Bhadriraju, K., and Chen, C.S. Cells lying on a bed of microneedles: an approach to isolate mechanical force. *Proc Natl Acad Sci U S A* 100, 1484, 2003.
210. Smith, L.A., Aranda-Espinoza, H., Haun, J.B., Dembo, M., and Hammer, D.A. Neutrophil traction stresses are concentrated in the uropod during migration. *Biophys J* 92, L58, 2007.
211. Schwarz, U.S., Balaban, N.Q., Riveline, D., Bershadsky, A., Geiger, B., and Safran, S.A. Calculation of forces at focal adhesions from elastic substrate data: the effect of localized force and the need for regularization. *Biophys J* 83, 1380, 2002.
212. Bershadsky, A.D., Balaban, N.Q., and Geiger, B. Adhesion-dependent cell mechanosensitivity. *Annu Rev Cell Dev Biol* 19, 677, 2003.
213. Saez, A., Buguin, A., Silberzan, P., and Ladoux, B. Is the mechanical activity of epithelial cells controlled by deformations or forces? *Biophys J* 89, L52, 2005.
214. Riveline, D., Zamir, E., Balaban, N.Q., Schwarz, U.S., Ishizaki, T., Narumiya, S., Kam, Z., Geiger, B., and Bershadsky, A.D. Focal contacts as mechanosensors: Externally applied local mechanical force induces growth of focal contacts by an mDia1-dependent and ROCK-independent mechanism. *Journal Of Cell Biology* 153, 1175, 2001.
215. Solon, J., Levental, I., Sengupta, K., Georges, P.C., and Janmey, P.A. Fibroblast adaptation and stiffness matching to soft elastic substrates. *Biophys J* 93, 4453, 2007.
216. Kong, H.J., Polte, T.R., Alsberg, E., and Mooney, D.J. FRET measurements of cell-traction forces and nano-scale clustering of adhesion ligands varied by substrate stiffness. *Proc Natl Acad Sci U S A* 102, 4300, 2005.
217. Guo, W.H., Frey, M.T., Burnham, N.A., and Wang, Y.L. Substrate rigidity regulates the formation and maintenance of tissues. *Biophys J* 90, 2213, 2006.

218. Cavalli, V., Corti, M., and Gruenberg, J. Endocytosis and signaling cascades: a close encounter. *FEBS Lett* 498, 190, 2001.
219. Chintagari, N.R., Jin, N., Wang, P., Narasaraju, T.A., Chen, J., and Liu, L. Effect of cholesterol depletion on exocytosis of alveolar type II cells. *Am J Respir Cell Mol Biol* 34, 677, 2006.
220. Ilangumaran, S., and Hoessli, D.C. Effects of cholesterol depletion by cyclodextrin on the sphingolipid microdomains of the plasma membrane. *Biochemical Journal* 335, 433, 1998.
221. Engler, A., Bacakova, L., Newman, C., Hategan, A., Griffin, M., and Discher, D. Substrate compliance versus ligand density in cell on gel responses. *Biophys J* 86, 617, 2004.
222. Michiels, C. Endothelial cell functions. *J Cell Physiol* 196, 430, 2003.
223. Sheetz, M.P., Sable, J.E., and Dobereiner, H.G. Continuous membrane-cytoskeleton adhesion requires continuous accommodation to lipid and cytoskeleton dynamics. *Annu. Rev. Biophys. Biomol. Struct.* 35, 417, 2006.
224. Paszek, M.J., Zahir, N., Johnson, K.R., Lakins, J.N., Rozenberg, G.I., Gefen, A., Reinhart-King, C.A., Margulies, S.S., Dembo, M., Boettiger, D., Hammer, D.A., and Weaver, V.M. Tensional homeostasis and the malignant phenotype. *Cancer Cell* 8, 241, 2005.
225. Georges, P.C., Hui, J.J., Gombos, Z., McCormick, M.E., Wang, A.Y., Uemura, M., Mick, R., Janmey, P.A., Furth, E.E., and Wells, R.G. Increased stiffness of the rat liver precedes matrix deposition: implications for fibrosis. *Am J Physiol Gastrointest Liver Physiol* 293, G1147, 2007.
226. Majno, G., and Joris, I. *Cells, tissues, and disease: principles of general pathology*. Worcester, Massachusetts: Blackwell Science, 1996.
227. Brown, X.Q., Ookawa, K., and Wong, J.Y. Evaluation of polydimethylsiloxane scaffolds with physiologically-relevant elastic moduli: interplay of substrate mechanics and surface chemistry effects on vascular smooth muscle cell response. *Biomaterials* 26, 3123, 2005.
228. Wong, J.Y., Velasco, A., Rajagopalan, P., and Pham, Q. Directed movement of vascular smooth muscle cells on gradient-compliant hydrogels. *Langmuir* 19, 1908, 2003.
229. Shi, P., Shen, K., Ghassemi, S., Hone, J., and Kam, L.C. Dynamic force generation by neural stem cells. *Cellular and Molecular Bioengineering* 2, 464, 2009.

230. Levental, I., Georges, P.C., and Janmey, P.A. Soft biological materials and their impact on cell function. *Soft Matter* 3, 299, 2007.
231. Miller, K., Chinzei, K., Orsengo, G., and Bednarz, P. Mechanical properties of brain tissue in-vivo: experiment and computer simulation. *J Biomech* 33, 1369, 2000.
232. Mazuchowski, E., and Thibault, L. Biomechanical properties of the human spinal cord and pia matter. 2003 Summer Bioengineering Conference. Key Biscayne, Florida: American Society of Mechanical Engineers, 2003, pp. 1205-1206.
233. Cheng, S., Clarke, E.C., and Bilston, L.E. Rheological properties of the tissues of the central nervous system: a review. *Med Eng Phys* 30, 1318, 2008.
234. Clarke, E.C., Cheng, S., and Bilston, L.E. The mechanical properties of neonatal rat spinal cord in vitro, and comparisons with adult. *J Biomech* 42, 1397, 2009.
235. Prange, M.T., and Margulies, S.S. Regional, directional, and age-dependent properties of the brain undergoing large deformation. *J Biomech Eng* 124, 244, 2002.
236. Ichihara, K., Taguchi, T., Shimada, Y., Sakuramoto, I., Kawano, S., and Kawai, S. Gray matter of the bovine cervical spinal cord is mechanically more rigid and fragile than the white matter. *J Neurotrauma* 18, 361, 2001.
237. Wang, Y.L., and Pelham, R.J., Jr. Preparation of a flexible, porous polyacrylamide substrate for mechanical studies of cultured cells. *Methods Enzymol* 298, 489, 1998.
238. Weisenhorn, A.L., Khorsandi, M., Kasas, S., Gotzos, V., and Butt, H.J. Deformation and height anomaly of soft surfaces studied with an AFM. *Nanotechnology* 4, 106, 1993.
239. Lin, L., Liu, A., Yu, Y., Zhang, C., Lim, C., Ng, S., Yap, P., and Gao, H. Cell compressibility studies utilizing noncontact hydrostatic pressure measurements on single living cells in a microchamber. *Applied Physics Letters* 92, 233901, 2008.
240. Rico, F., Roca-Cusachs, P., Gavara, N., Farre, R., Rotger, M., and Navajas, D. Probing mechanical properties of living cells by atomic force microscopy with blunted pyramidal cantilever tips. *Phys Rev E Stat Nonlin Soft Matter Phys* 72, 021914, 2005.
241. Gonthier, B., Nasarre, C., Rudiger, T., and Bagnard, D. Protocol for the primary culture of cortical neurons. Basel: Karger, 2005.
242. Tessier-Lavigne, M., and Goodman, C.S. The molecular biology of axon guidance. *Science* 274, 1123, 1996.

243. Gallo, G., Yee, H.F., Jr., and Letourneau, P.C. Actin turnover is required to prevent axon retraction driven by endogenous actomyosin contractility. *J Cell Biol* 158, 1219, 2002.
244. Lo, C.-M., Wang, H.-B., Dembo, M., and Wang, Y.-L. Cell movement is guided by the rigidity of the substrate. *Biophys J* 79, 144, 2000.
245. Peyton, S.R., and Putnam, A.J. Extracellular matrix rigidity governs smooth muscle cell motility in a biphasic fashion. *J Cell Physiol* 204, 198, 2005.
246. Kostic, A., Sap, J., and Sheetz, M.P. RPTPalph $\alpha$  is required for rigidity-dependent inhibition of extension and differentiation of hippocampal neurons. *J Cell Sci* 120, 3895, 2007.
247. Bagnard, D., Chounlamountri, N., Puschel, A.W., and Bolz, J. Axonal surface molecules act in combination with semaphorin 3a during the establishment of corticothalamic projections. *Cereb Cortex* 11, 278, 2001.
248. Basarsky, T.A., Parpura, V., and Haydon, P.G. Hippocampal synaptogenesis in cell culture: developmental time course of synapse formation, calcium influx, and synaptic protein distribution. *J Neurosci* 14, 6402, 1994.
249. Tischler, A.S., Riseberg, J.C., Hardenbrook, M.A., and Cherington, V. Nerve growth factor is a potent inducer of proliferation and neuronal differentiation for adult rat chromaffin cells in vitro. *J Neurosci* 13, 1533, 1993.
250. Tucker, K.L., Meyer, M., and Barde, Y.A. Neurotrophins are required for nerve growth during development. *Nat Neurosci* 4, 29, 2001.
251. Odde, D.J., Tanaka, E.M., Hawkins, S.S., and Buettnner, H.M. Stochastic dynamics of the nerve growth cone and its microtubules during neurite outgrowth. *Biotechnol Bioeng* 50, 452, 1996.
252. Dennerll, T.J., Lamoureux, P., Buxbaum, R.E., and Heidemann, S.R. The cytomechanics of axonal elongation and retraction. *J Cell Biol* 109, 3073, 1989.
253. Lemmon, V., Burden, S.M., Payne, H.R., Elmslie, G.J., and Hlavin, M.L. Neurite growth on different substrates: permissive versus instructive influences and the role of adhesive strength. *J Neurosci* 12, 818, 1992.
254. Fiford, R.J., and Bilston, L.E. The mechanical properties of rat spinal cord in vitro. *J Biomech* 38, 1509, 2005.
255. Kawaguchi, Y., Karube, F., and Kubota, Y. Dendritic branch typing and spine expression patterns in cortical nonpyramidal cells. *Cereb Cortex* 16, 696, 2006.

256. Jay, P.Y., Pham, P.A., Wong, S.A., and Elson, E.L. A mechanical function of myosin II in cell motility. *J Cell Sci* 108 (Pt 1), 387, 1995.
257. Bridgman, P.C., Dave, S., Asnes, C.F., Tullio, A.N., and Adelstein, R.S. Myosin IIB is required for growth cone motility. *J Neurosci* 21, 6159, 2001.
258. Wylie, S.R., and Chantler, P.D. Separate but linked functions of conventional myosins modulate adhesion and neurite outgrowth. *Nat Cell Biol* 3, 88, 2001.
259. Bentley, D., and Toroian-Raymond, A. Disoriented pathfinding by pioneer neurone growth cones deprived of filopodia by cytochalasin treatment. *Nature* 323, 712, 1986.
260. Gallo, G. Myosin II activity is required for severing-induced axon retraction in vitro. *Exp Neurol* 189, 112, 2004.
261. Billuart, P., Winter, C.G., Maresh, A., Zhao, X., and Luo, L. Regulating axon branch stability: the role of p190 RhoGAP in repressing a retraction signaling pathway. *Cell* 107, 195, 2001.
262. Ketschek, A.R., Jones, S.L., and Gallo, G. Axon extension in the fast and slow lanes: substratum-dependent engagement of myosin II functions. *Dev Neurobiol* 67, 1305, 2007.
263. Jiang, G., Huang, A.H., Cai, Y., Tanase, M., and Sheetz, M.P. Rigidity sensing at the leading edge through  $\alpha$ 5 $\beta$ 3 integrins and RPTP $\alpha$ . *Biophys J* 90, 1804, 2006.
264. Boal, D. *Mechanics of the cell*. Cambridge, United Kingdom: Cambridge University Press, 2002.
265. Rakic, P. Specification of cerebral cortical areas. *Science* 241, 170, 1988.
266. Rice, D.S., and Curran, T. Role of the reelin signaling pathway in central nervous system development. *Annu Rev Neurosci* 24, 1005, 2001.
267. Lamoureux, P., Buxbaum, R.E., and Heidemann, S.R. Direct evidence that growth cones pull. *Nature* 340, 159, 1989.
268. Stokols, S., Sakamoto, J., Breckon, C., Holt, T., Weiss, J., and Tuszynski, M.H. Templated agarose scaffolds support linear axonal regeneration. *Tissue Eng* 12, 2777, 2006.
269. Limozin, L., and Sengupta, K. Quantitative reflection interference contrast microscopy (RICM) in soft matter and cell adhesion. *Chem Phys Chem* 10, 2752, 2009.

270. Sund, S.E., and Axelrod, D. Actin dynamics at the living cell submembrane imaged by total internal reflection fluorescence photobleaching. *Biophys J* 79, 1655, 2000.
271. Evans, E., and Rawicz, W. Entropy-driven tension and bending elasticity in condensed-fluid membranes. *Phys Rev Lett* 64, 2094, 1990.
272. Raucher, D., and Sheetz, M.P. Membrane expansion increases endocytosis rate during mitosis. *J Cell Biol* 144, 497, 1999.
273. Upadhyaya, A., and Sheetz, M.P. Tension in tubulovesicular networks of Golgi and endoplasmic reticulum membranes. *Biophys J* 86, 2923, 2004.
274. Kramers, H. Brownian motion in a field of force and the diffusion model of chemical reactions. *Physica* Jan., 1940.
275. Helfrich, W., and Servuss, R.M. Undulations, steric interaction and cohesion of fluid membranes. *Nuovo Cimento D.* 3, 137, 1984.